



저작자표시-비영리-변경금지 2.0 대한민국

이용자는 아래의 조건을 따르는 경우에 한하여 자유롭게

- 이 저작물을 복제, 배포, 전송, 전시, 공연 및 방송할 수 있습니다.

다음과 같은 조건을 따라야 합니다:



저작자표시. 귀하는 원저작자를 표시하여야 합니다.



비영리. 귀하는 이 저작물을 영리 목적으로 이용할 수 없습니다.



변경금지. 귀하는 이 저작물을 개작, 변형 또는 가공할 수 없습니다.

- 귀하는, 이 저작물의 재이용이나 배포의 경우, 이 저작물에 적용된 이용허락조건을 명확하게 나타내어야 합니다.
- 저작권자로부터 별도의 허가를 받으면 이러한 조건들은 적용되지 않습니다.

저작권법에 따른 이용자의 권리는 위의 내용에 의하여 영향을 받지 않습니다.

이것은 [이용허락규약\(Legal Code\)](#)을 이해하기 쉽게 요약한 것입니다.

[Disclaimer](#)

공학박사학위논문

**Nanostructure Engineering and
Mechanical/Electrochemical Performances
of Nanocarbon Based Composite Films**

나노탄소 기반 복합체 필름의 나노구조 공학과
역학적/전기화학적 성능에 관한 연구

2016년 2월

서울대학교 대학원

재료공학부

오 준 영

**Nanostructure Engineering and Mechanical/Electrochemical
Performances of Nanocarbon Based Composite Films**

지도교수 박종래

이 논문을 공학박사 학위논문으로 제출함

2015 년 10 월

서울대학교 대학원

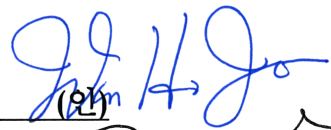
재료공학부

오준영

오준영의 박사학위논문을 인준함

2015 년 12 월

위원장 _____ 조원호


(인)

부위원장 _____ 박종래


(인)

위원 _____ 장지영


(인)

위원 _____ 박민


(인)

위원 _____ 양승재


(인)

Abstract

Nanostructure Engineering and Mechanical/Electrochemical Performances of Nanocarbon Based Composite Films

Jun Young Oh

Department of Materials Science and Engineering

The Graduate School

Seoul National University

This study describes the preparation and characterization of novel carbon nanotube (CNT) based composite films with various tailored nanostructures for use in structural and multifunctional materials. CNTs have attracted great interest due to their unique mechanical, electrical, and thermal properties. This has stimulated fundamental research on the physical/chemical nature and versatile route for their technological applications in recent decades. However, macroscopic materials such as buckypaper, fiber, and yarn consisting of randomly oriented CNTs lose the intrinsic properties of individual CNTs against all expectations. In addition, previously reported CNT films with low interaction forces can degrade easily and lose performance by an external force. Methods to control the nanostructure have so far been unable to simultaneously satisfy

performance, damage-tolerance, and high throughput. Therefore, a controlled assembly of CNTs in ordered nanostructures with strong interaction forces can lead to high strength CNT films.

Chapter 1 provides a general introduction of the relevant physical/chemical parameters that contribute to strength and multifunctional capabilities of CNT based composite films. Additionally, the state-of-the art materials and unsolved issues are discussed. The aims of the present work are introduced considering the fundamental and theoretical issues.

Chapter 2 presents a theoretical study for the strength of CNT film in comparison with the performance between previously reported experimental results. The correlation between the mechanical properties and the structural parameters is investigated to provide insight into the influencing factors. Theoretical modeling for the CNT film is conducted to indicate the performance of CNT films with the specified structure and interactions. Conclusively, the ideal structure and properties of CNT film based on the theoretical prediction are proposed.

Chapters 3 and 4 discuss the preparation and properties of self-assembled, well-aligned CNTs and graphene oxide (GO)@CNT with a densely packed nanostructure as a strategy to develop unique load-bearing architecture for high strength film. Highly aligned CNTs with high packing density are prepared in the form of buckypaper via a simple filtration method. The CNT suspension concentration is strongly reflected in the alignment and assembly behavior of CNT buckypaper. We further demonstrated that the horizontally aligned CNT domain gradually increases in size when increasing the deposited CNT quantity.

The resultant aligned buckypaper exhibited enhanced packing density, strength, modulus, and hardness compared to previously reported buckypapers. Furthermore, a novel approach in mimicking the natural bone structure is fabricating a hybrid composite paper based on GO and CNT. The size-tuning strategy enables smaller GO sheets to have more cross-linking reactions with CNTs and be homogeneously incorporated into CNT-assembled paper, which is advantageous for effective stress transfer. The resultant hybrid composite film has enhanced mechanical strength, modulus, toughness, and even electrical conductivity compared to previously reported CNT-GO based composites. We further demonstrate the usefulness of the size-tuned GOs as the “stress transfer medium” by performing in-situ Raman spectroscopy during the tensile test.

Chapter 5 focuses on a design and characterization of tannic acid (TA)@CNT composite film that relies on bio-metal coordination bonds to strengthen the interaction forces between CNTs. The TA@CNT film exhibits very high strength and flexibility. The materials sustain their high energy storage performance upon extremely bended conditions and demonstrate their utilization for flexible energy storage systems.

Keywords: carbon nanotubes, alignment, self-assembly, mechanical properties, graphene oxide, bone tissue, structural material, flexible energy storage system, supercapacitor

Student Number: 2011-30190

Contents

Abstract	i
Chapter 1 Introduction	1
1.1 General introduction to CNT based composite films.....	1
1.1.1 Overview of CNTs	1
1.1.2 Nanostructure engineering of CNT films.....	4
1.2 CNT based high strength films	8
1.2.1 Fundamentals and theoretical considerations of tensile properties of CNT based films	8
1.2.2 State-of-the-art works on assembly methods for high strength CNT films 	12
1.2.2.1 Aligned, high-density CNTs	12
1.2.2.2 Engineered interaction forces between CNTs	16
1.2.3 Issues associated with nanostructure engineering for high strength CNT films.....	18
1.3 CNT based composite films for flexible energy storage applications	19
1.3.1 Fundamentals and theory of a flexible supercapacitor	19
1.3.1.1 Supercapacitor electrode	19
1.3.1.2 State-of-the-art works on CNT based flexible supercapacitor electrode	22
1.3.2 Issues associated with flexible supercapacitors	24

1.4 Aim and scope of this research	25
1.4.1 Theoretical study of the strength of CNT films	25
1.4.2 Preparation and characterization of highly aligned, high-density CNT films	25
1.4.3 Preparation and characterization of bone-mimicking GO@CNT hybrid films	26
1.4.4 Preparation and characterization of flexible, high strength freestanding, pseudocapacitive CNT film by metal-bio coordination method	26
1.5 References	27
Chapter 2 Theoretical Approach and Prediction of the High Strength CNT Film.....	36
2.0 Major symbols	36
2.1 Theoretical consideration relevant to CNT based high strength films.....	37
2.2 Comparison of theoretical prediction and experimental results	42
2.3 Effect of structural parameters on the strength of CNT films.....	46
2.4 Conclusion	49
2.5 References	50
Chapter 3 Preparation and Mechanical Performance of Self- Assembled, Aligned CNT Film with High Packing Density	52
3.1 Introduction.....	52

3.2 Results and discussion	54
3.3 Experimental	87
3.4 Conclusion	90
3.5 References	91
Chapter 4 Preparation and Mechanical Performance of Bone-mimicking Size-Tuned GO@CNT Hybrid Film.....	100
4.1 Introduction	100
4.2 Results and discussion	103
4.3 Experimental	130
4.4 Conclusions	132
4.5 References	133
Chapter 5 Preparation and Mechanical/ Electrochemical Performance of TA@CNT Hybrid Film for Flexible Energy Storage System	140
5.1 Introduction	140
5.2 Results and discussion	142
5.3 Experimental	171
5.4 Conclusion	173
5.5 References	174
Abstract in Korean	176
List of Publications	179

List of Tables

Table 2.1. Comparison of the interaction energy levels

Table 2.2. Previously reported CNT buckypapers

Table 3.1. Comparison of mechanical properties of SWNT buckypapers prepared under various suspension concentrations

Table 4.1. Size of fragmented GO sheets characterized by DLS measurement

Table 4.2. Summary of SWNT-GO film mechanical and electrical performance

Table 5.1. Tensile strength of pristine SWNT, TA@SWNT prepared without Fe ions, TA@SWNT_Fe_pH1, and TA@SWNT_Fe_pH7 films

List of Figures

- Fig. 1.1.** Nanocarbon families.
- Fig. 1.2.** Nanostructure engineering of CNT to be used as a multifunctional material for future applications.
- Fig. 1.3.** The relationships between fiber, yarn and rope.
- Fig. 1.4.** CVD-grown aligned CNTs on a template substrate.
- Fig. 1.5.** MWNTs dispersed in nematic-liquid-crystal solvents (E7) with an external field.
- Fig. 1.6.** Alignment method of CNTs dispersed in a solvent with the application of shear force; optical images of glass with (a) and without (b) a polarizer.
- Fig. 1.7.** Schematic of the formation mechanism of aligned CNT fiber.
- Fig. 1.8.** Scheme of the layer-by-layer (LBL) method.
- Fig. 1.9.** Comparison of energy storage systems.
- Fig. 2.1.** The packing density of CNT film.
- Fig. 2.2.** The degree of alignment of CNT along the tensile load axis.
- Fig. 2.3.** Comparison of theoretically calculated values with previously reported experimental results.
- Fig. 2.4.** Effect of the CNT alignment on the strength of CNT films [Conditions: $\sigma_{CNT} = 30$ GPa, $D = 1$, $d_{CL} = 1$, $a = 0.5$, $I_{CNT} = 309$ kJ/mol, and $\phi = 1$]
- Fig. 2.5.** Effect of the CNT packing density on the strength of CNT films [Conditions: $\sigma_{CNT} = 30$ GPa, $D = 1$, $d_{CL} = 1$, $a = 0.5$, $I_{CNT} = 309$ kJ/mol, and $\phi_i = 0^\circ$]
- Fig. 2.6.** Effect of the type of interaction between CNTs on the strength of CNT films [Conditions: $\sigma_{CNT} = 30$ GPa, $D = 1$, $d_{CL} = 1$, $a = 0.5$, $\phi = 1$, and $\phi_i = 0^\circ$]
- Fig. 2.7.** Effect of the crosslinking density on the strength of CNT films [Conditions: $\sigma_{CNT} = 30$ GPa, $D = 1$, $a = 0.5$, $I_{CNT} = 309$ kJ/mol, $\phi = 1$, and $\phi_i = 0^\circ$]

Fig. 3.1. Mechanism for self-alignment behavior of CNTs with subsequent filtration process.

Fig. 3.2. (a) Photograph of residue ring stain after drying SWNT suspension droplet on a glass substrate, (b) POM image of perimeter, (c) aligned SWNTs in the edge regime, (d) non-aligned SWNTs in the center regime.

Fig. 3.3. POM image sequence of SWNT buckypaper prepared from (a) high concentration suspension and (b) low concentration suspension.

Fig. 3.4. SEM images of the surface of SWNT buckypapers prepared on the PTFE membrane with pore size of 200 nm (filtration velocity: 3.8 mL/h). The deposited SWNT quantities on the membrane: (a-b) 10.0 mg/cm², (c-d) 7.5 mg/cm², (e-f) 5.0 mg/cm², (g-h) 2.5 mg/cm².

Fig. 3.5. Phase diagram of CNTs (D=1, L=1000) in N-methyl-2-pyrrolidone (NMP). The Flory-Huggins interaction parameter, χ , is plotted against CNT volume fraction. I and N indicate isotropic and nematic phase of CNTs, respectively. The two lines denote the boundary of the dispersion state transition. The region between the lines corresponds to the biphasic region (I+N).

Fig. 3.6. The birefringence intensity of POM images of SWNT buckypapers prepared under various suspension concentrations.

Fig. 3.7. Comparison of size distributions of aligned SWNT domains showing birefringence texture, including representative POM images of buckypapers prepared on the PTFE membrane with pore size of 200 nm (a, c, e, g: slow filtration, 3.8 mL/h), and 500 nm (b, d, f, h: fast filtration, 6.3 mL/h).

Fig. 3.8. SEM images of the surface of SWNT buckypapers prepared on the PTFE membrane with pore size of 500 nm (filtration velocity: 6.3 mL/h). The deposited SWNT

quantities on the membrane: (a-b) 10.0 mg/cm², (c-d) 7.5 mg/cm², (e-f) 5.0 mg/cm², (g-h) 2.5 mg/cm².

Fig. 3.9. XPS C1s spectra of (a) pristine SWNTs and (b) acid oxidized SWNTs. (c) Quantitative analysis of various forms of C in the SWNTs, determined by integrating the C1s spectra peak area corresponding to the C-C & C=C, C-O & C=O, O-C=O bonded carbon. (d) Raman Spectra of SWNTs.

Fig. 3.10. Photograph of SWNT suspensions in NMP (suspension concentration: 1 mg/mL).

Fig. 3.11. Tapping-mode AFM image of acid oxidized SWNTs on a mica surface.

Fig. 3.12. UV-vis spectra of acid treated SWNT suspensions in various solvents.

Fig. 3.13. SEM image of the surface of buckypaper prepared by pristine SWNT suspension.

Fig. 3.14. SEM images: (a) pristine SWNTs, (b) acid oxidized SWNTs just after acid oxidation, deionized water purification, and drying process, (c) aligned, acid oxidized SWNTs on PTFE, (d) aligned, acid oxidized SWNTs on AAO, (e) aligned, surfactant wrapped SWNTs and (f) aligned, acid oxidized MWNTs. The total deposited CNT quantity and suspension concentration to prepare the aligned buckypapers (c, d, e, and f) were 10.0 mg/cm², and 1.0 mg/mL, respectively.

Fig. 3.15. N₂ adsorption isotherms (at 77K): (a) pristine SWNTs, (b) acid oxidized SWNTs and (c) aligned SWNTs.

Fig. 3.16. Pore size distribution of the pristine SWNTs powder, aligned and non-aligned SWNT buckypaper.

Fig. 3.17. (a) Representative tensile stress-strain curves of SWNT buckypapers prepared under various suspension concentrations (mg/mL). (b) Comparison of tensile strength and modulus for CNT buckypapers. (c) Representative nanoindentation load-

displacement curves of SWNT buckypapers prepared under various suspension concentrations (mg/mL). Inset AFM images show the surface of aligned (left, 1.0 mg/mL) and non-aligned (right, 0.01 mg/mL) SWNT papers after nanoindentation measurement applying 1 mN. (d) Comparison of compressive elastic modulus and hardness for a set of CNTs.

Fig. 3.18. Photographs of (a) freestanding aligned SWNT buckypapers, (b) papers which are cut into rectangular shape for tensile test, and (c) a bent piece of flexible paper.

Fig. 3.19. Tensile stress-strain curves of two samples shown in inset (Photograph showing that SWNT buckypaper was split into two directions).

Fig. 4.1. a) Preparation process of SWNT-GO hybrid film. b) The size distribution of GO sheets depending on the tip sonication time (0 ~ 30 min). The insets are the polarized 1.0 mg/mL GO suspension optical micrographs.

Fig. 4.2. a) SEM image of individualized SWNTs on a Si wafer and b) their length distribution.

Fig. 4.3. TEM image of GO30 sheets and SWNTs after sonication.

Fig. 4.4. a) SWNT-GO suspension precipitation depending on the cross-linking reaction between SWNTs and GO sheets by PPD molecules b) Absorbance at 550 nm of SWNT-GO suspensions acquired by UV-vis spectroscopy to quantitatively monitor the cross-linking reaction. c) XPS wide spectra of SWNT-GO films. XRD patterns of d) only GO sheets and e) SWNT-GO hybrid films.

Fig. 4.5. XPS wide spectrum of SWNT-GO30 film without cross-linking agent.

Fig. 4.6. a) TEM image of the SWNT-GO30 sample after cross-linking and elemental maps of b) carbon, c) oxygen, and d) nitrogen.

Fig. 4.7. a) Stress-strain curves of SWNT-GO0 (gray), -GO10 (pink), -GO20 (blue), and T-GO30 (green) films. b) Tensile strength (black squares) and elastic modulus (blue squares). c) Toughness values of SWNT-GO films

Fig. 4.8. Representative stress-strain curves of SWNT, SWNT with PPD, and SWNT-GO film without PPD.

Fig. 4.9. a) Electrical conductivities of SWNT-GO films. b) Comparison of tensile strength and toughness values of prior-art materials. Fully-filled square, half-filled square, and non-filled square indicate the order of electrical conductivity.

Fig. 4.10. SEM micrographs and large area AFM images with line scan results showing the surface morphologies and fractured ends after tensile testing of a, e, i) SWNT-GO0; b, f, j) SWNT-GO10; c, g, k) SWNT-GO20; and d, h, i) SWNT-GO30 films.

Fig. 4.11. a) Schematic illustration of *in-situ* Raman spectroscopy at tensile stage. b) G' band Raman spectra of SWNT-GO30 film under tensile strain. c) G' peak shift in the Raman spectra of the SWNT-GO films during tensile loading. d) TEM image showing the inter-connection between SWNTs and GO sheets. e) Polarized Raman spectra along the tensile axis showing relative orientation change of SWNT-GO30 after failure. f) Relative G peak intensity ratio in polarized Raman spectra of SWNT-GO films after failure. g) Fractured surface of SWNT-GO30 film between two crossed linear polarizer with an inset of normal OM image.

Fig. 4.12. G' band Raman spectra of a) SWNT-GO0, b) SWNT-GO10, and c) SWNT-GO20 films under tensile strain.

Fig. 4.13. Polarized Raman spectra along the tensile and perpendicular axis showing the relative orientation change of a) SWNT-GO0, b) SWNT-GO10, and c) SWNT-GO20 films after failure.

Fig. 4.14. Fractured surface of a) SWNT-GO0, b) SWNT-GO10, and c) SWNT-GO20 film after failure and their POM images under two crossed linear polarizer.

Fig. 4.15. Schematic diagram showing different architecture and fracture behavior of cross-linked a) SWNT-large GO and b) SWNT-small GO films.

Fig. 5.1. Scheme of the TA@SWNT film preparation by Fe-catechol coordination.

Fig. 5.2. Photograph of TA@SWNT suspensions before and after Fe ion addition.

Fig. 5.3. TEM images of (a) pristine and (b) TA functionalized SWNT.

Fig. 5.4. TEM image and EDX line mapping analysis results of the TA functionalized, individual SWNT for carbon, oxygen, and iron elements with an inset table indicating content quantity.

Fig. 5.5. SEM images of (a) pristine SWNT film and (b) TA@SWNT_10:1 film. EDX mapping analysis results of the TA@SWNT film for the carbon (red), oxygen (green), and iron (aquamarine) elements.

Fig. 5.6. C1s XPS spectra of (a) pristine SWNT film, (b) TA@SWNT_5:1 film, and (c) TA@SWNT_10:1 film. The quantitative analysis of various forms of carbon in the films calculated from C1s peak deconvolution.

Fig. 5.7. TGA curves of pristine SWNT, TA@SWNT_5:1, and TA@SWNT_10:1 films.

Fig. 5.8. The electrical conductivities of pristine SWNT, TA@SWNT_5:1, and TA@SWNT_10:1 films.

Fig. 5.9. Stress-strain curves of pristine SWNT (black), TA@SWNT prepared without Fe ions (red), TA@SWNT_Fe_pH1 (incarnadine), and TA@SWNT_Fe_pH7 (blue) films.

Fig. 5.10. Raman spectra of TA@SWNT prepared with varying pH.

Fig. 5.11. Photograph bended TA@SWNT film showing flexibility.

Fig. 5.12. Cyclic voltammetry curves of pristine SWNT, TA@SWNT_5:1, and TA@SWNT_10:1 films at a sweep rate of 10 mV/s in 1M H₂SO₄ solution.

Fig. 5.13. Galvanostatic charge-discharge plot for (a) pristine SWNT, TA@SWNT_5:1, and TA@SWNT_10:1 films with a current of 1A/g (b) TA@SWNT_10:1 films with various currents in 1M H₂SO₄ solution.

Fig. 5.14. Overall capacitance of the films as a function of discharge current density.

Fig. 5.15. The electrical conductivities of the heated TA@SWNT_10:1 films.

Fig. 5.16. C1s XPS spectra of TA@SWNT_10:1 film after carbonization (a) at 200 and (b) 400°C. The quantitative analysis of various carbon forms in the films are calculated from the C1s peak deconvolution.

Fig. 5.17. (a) Galvanostatic charge-discharge plot for TA@SWNT_10:1 films with varied carbonization temperatures. (b) Overall film capacitance as a function of discharge current density with 1M H₂SO₄ solution.

Fig. 5.18. Nyquist impedance spectra of the TA@SWNT films.

Fig. 5.19. Ragone plot for the TA@SWNT film at various charge-discharge rates in the working potential range of -0.2-1V. The data were calculated based on the total mass of the active electrode materials.

Fig. 5.20. Cycling stability of TA@SWNT film upon bending. The inset image shows the bent, flexible, and freestanding film.

Chapter 1 Introduction

1.1 General introduction to CNT based composite films

1.1.1 Overview of CNTs

Carbon (C) is a remarkable element, forming a myriad of structures with unique properties. The carbon atom is in column IV of the periodic table and has an electronic ground state configuration of $1s^2 2s^2 2p^2$. Such a configuration can be changed by hybridization of the orbitals in atomic carbon to sp , sp^2 , and sp^3 . The recent discoveries of carbon nanomaterial families such as fullerenes (0D buckyballs), carbon nanotubes (1D nanotubes) and graphene (2D nanosheets) have stimulated intense interest in the nanotechnology community (Figure 1.1).^{1,2}

Single-walled CNTs (SWNTs) and multi-walled CNTs (MWNTs) are cylinder-shaped carbon allotropes of one or more layers of rolled graphene.² CNTs with sp^2 -bonded carbons and a hexagonal type of network architecture provide a number of unique properties. Their strengths have been found to have an extremely high modulus of ~ 1 TPa and tensile strength of 30 GPa for SWNTs and 100 GPa for MWNTs, meaning that CNTs are the strongest and most flexible materials able to sustain a large amount of strain.³⁻⁵ Because their density is as low as ~ 1.3 g/cm³, CNTs are attracting great interest for high strength, lightweight material applications.^{6,7} Furthermore, CNT bundles have both high electrical (10^{6-7} S/cm, resistivity $\sim 10^{-3}$ Ω /cm) and thermal conductivity (200 W/mK). Recently, CNTs were grown with diameters of 1~2 nm (SWNTs) and 5~20 nm (MWNTs), with lengths between 20 ~ 100 μ m, exhibiting a high aspect ratio (greater

than 10^3) along the tube axis.⁸ These small dimensions give CNTs a tremendously high surface area ($\sim 1000 \text{ m}^2/\text{g}$). Their outstanding properties extend their potential to a wide range of applications, including fiber-reinforced composites, films, microelectronics, nanoelectromechanical systems, and energy storage systems.⁸

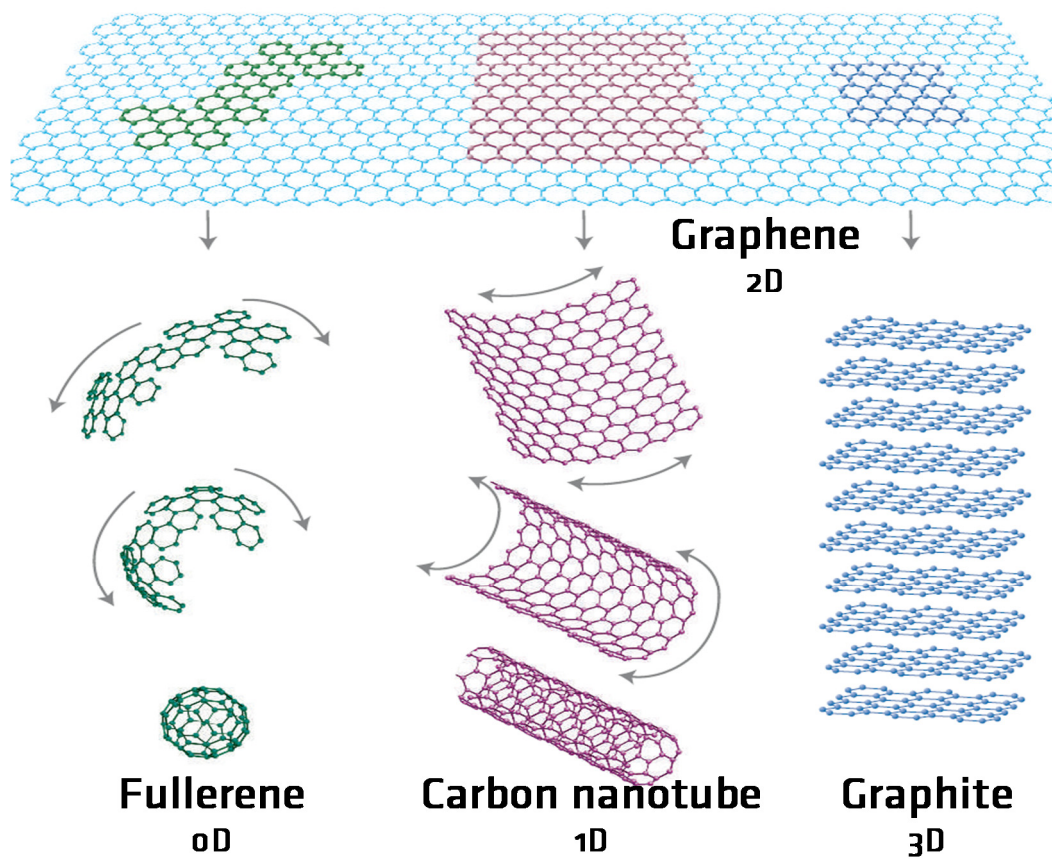


Fig. 1.1. Nanocarbon families.¹

1.1.2 Nanostructure engineering of CNT films

No materials have shown a combination of exceptional mechanical, electronic, thermal properties to match those of CNTs. Therefore, CNTs are strongly expected to be used as a multifunctional material when applied. Recently, most synthesis methods for CNTs which are close to commercialization have produced unorganized, CNT architectures. To utilize their unique properties in many bulk applications, devising custom nanostructure engineering techniques for each application is quite important. The macroscopic forms of CNTs include buckypaper, fibers, and yarn (Figure 1.2).^{9, 10} Different types of nanostructural engineering of the orientations, interactions, and functionalities of CNTs in the bulk form are most challenging issues.

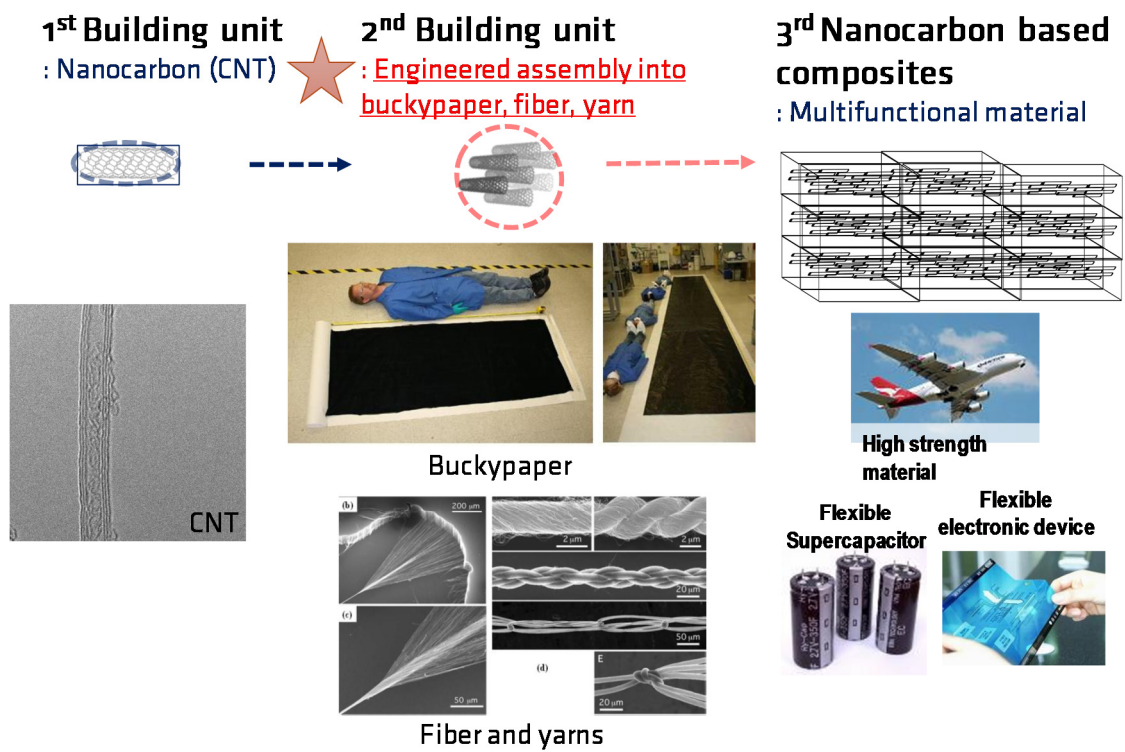


Fig. 1.2. Nanostructure engineering of CNT to be used as a multifunctional material for future applications.^{9, 10}

The practical use of CNTs is limited due to difficulties related to the assembly of CNTs into desired structures arising from the dispersion of CNTs in an aqueous solvent. The high cohesive energy between the tubes (0.5~2.0 eV per nanometer) allow CNTs to form bundled structures easily.¹¹ Raw CNTs are desired because they can spontaneously dissolve and debundle in a solvent. However, the solubility of raw CNTs is very low in organic solvents such as dimethylformamide, chloroform and ethanol. To facilitate dispersion, the surface functionalization of CNTs has been extensively explored to improve the miscibility of CNTs in various solvents.¹¹

Modification methods are based on the covalent bonding of functional groups and on the non-covalent wrapping or adsorption of molecules onto the CNT surfaces. Covalent bonding, represented by acid oxidation of the surfaces of the CNTs, leads to the formation of oxygen functional groups such as carboxylic and hydroxyl groups. Many oxidants, including sulfuric, nitric, and formic acids and mixtures containing these acids have been used in an effort to functionalize CNTs and disperse them into aqueous solutions.¹²⁻¹⁵ Furthermore, other surface modifications such as fluorination,^{16, 17} thiolation¹⁸ and amidation¹⁹⁻²² have been also assessed for practical use.

While covalent surface modification methods disrupt sp^2 hybridization and deteriorate the intrinsic properties of CNTs, non-covalent surface modification methods are advantageous for preserving the sp^2 -conjugated structure and the electronic performance of CNTs. The adsorption of both ionic and nonionic surfactants (amphiphilic molecules) onto CNT surfaces is the most widely used method because it offers effective dispersion and a non-destructive process.¹¹ A suggested mechanism for the adsorption and dispersion involves the hydrophobic part of the surfactants, which adsorbs and encapsulates the surfaces of the CNTs, and the hydrophilic part, which interacts with

water, resulting in the formation of a stable suspension. In addition, other organic materials with aromatic compounds including pyrene,²³⁻²⁵ porphyrin,²⁶ and poly(acrylic acid),²⁷ as well as biological molecules such as DNA,^{28, 29} reportedly interact with the sidewalls of CNTs and enhance their solubility.

1.2 CNT based high strength films

1.2.1 Fundamentals and theoretical considerations of tensile properties of CNT based films

High-strength CNT films have attracted remarkable interest due to the outstanding performance capabilities of individual CNTs. The nanostructural engineering of CNTs would determine the properties of the film, forming an important stage for applications. Theoretical considerations and predictions of the tensile properties of CNT films are urgently required prior to the assembly of CNTs. However, few theoretical models are available regarding how the tensile properties of CNT films depend on their length, diameter, strength as well as orientation with regard to the interaction between CNTs.

Herein, we need to revisit the structural mechanics of yarn, well established in theory. Yarn is defined as long, fine fiber structures which can be assembled into textiles, ropes and cables. Yarn is composed of spun-short staple fibers. It is the simplest building unit of cables. As shown in Figure 1.3, there is a strong relationship between fiber (the first building unit) and yarn (the second building unit). The mechanical performance of rope is determined by the properties of the yarn constituting it, which depend on the fiber properties and the geometric structure of the yarn. The commonly used theoretical equation regarding the strength of yarn and its geometric structure can be expressed as

$$\frac{\sigma_{yarn}}{\sigma_{fiber}} \approx \cos^2 \alpha [1 - (k \operatorname{cosec} \alpha)] \quad (1.1)$$

where σ_{yarn} and σ_{fiber} are the tensile strength of the yarn, and the fiber,³⁰⁻³² and α is the twisting angle. Here, k is determined by

$$k = \frac{(DQ/\mu)^{1/2}}{3L} \quad (1.2)$$

where L , D , Q , and μ are the length and diameter of the fiber, the fiber migration length, and the friction coefficient between the fibers, respectively.³² From the above equations, we can surmise that the strength of yarn is determined by the twisting angle of the fibers and the complex parameter k . The strength increases with a longer fiber length, a smaller fiber diameter and with longer migration length. As the fibers are twisted, the contact and friction force between the fibers also increases.

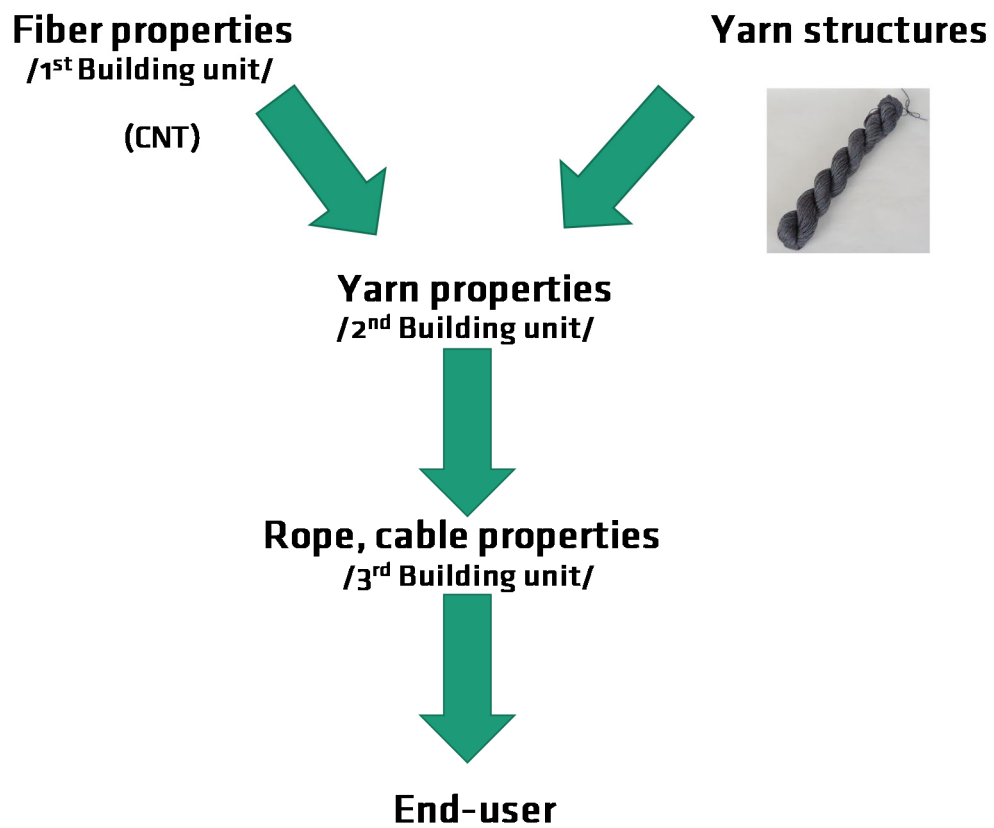


Fig. 1.3. The relationships between fiber, yarn and rope.

From equations (1.1) and (1.2), we found that the strength of yarn depends on its geometric structure. Although there are no theoretical equations regarding the tensile properties for films composed of CNTs, the strength of the film may be closely related to the properties of the CNTs and their nanostructures. Because an individual CNT is known to be 30 times stronger than Kevlar and 117 times stronger than steel, CNT film is expected to have very high strength.

However, previously reported CNT films have exhibited much lower mechanical performance capabilities compared to the expected levels. The most significant contributors to the low mechanical properties of CNT films were found to be randomly oriented CNTs with a low packing density and weak interactions. The nanostructural engineering of CNTs into aligned architectures is necessary before next-generation CNT films can be realized. Numerous studies have attempted to control the alignment of CNTs and their interactions. Here, we briefly assess the state-of-the-art works on assembly methods and related key issues. A new theoretical approach and predictions of the tensile strengths of CNT films are then discussed in **Chapter 2** in more detail.

1.2.2 State-of-the-art works on assembly methods for high strength CNT films

1.2.2.1 Aligned, high-density CNTs

Previous attempts to align CNTs can be classified into two categories according to the synthesis and alignment procedures. In-situ synthesis methods to align CNTs on a template substrate have been studied extensively in conjunction with the chemical vapor deposition (CVD) method (Figure 1.4).³³ Many researchers have attempted to control the length, diameter, purity and the number of walls of CNTs. The degree of alignment of grown CNTs has been found to depend on the synthesis conditions, such as the temperature, type of injected gases, and the patterning methods of the catalyst used.

In contrast, post-synthesis alignment methods of disordered CNTs are based on a solution process, which has an advantage in that it can be scaled up. Various studies have been reported, including external fields,³⁴⁻³⁹ liquid crystal,^{34, 40-42} mechanical shearing,⁴³⁻⁴⁵ patterned substrates,⁴⁶ and dip coating.⁴⁷ Through the use of an electric or magnetic field in a CNT-dispersed suspension, the alignment of CNTs was controlled (Figure 1.5). Another approach to align CNTs was to embed CNTs into nematic liquid crystals. Because these liquid crystals are aligned, the pi-pi interaction between the liquid crystals and the CNTs was suggested as an alignment mechanism. Furthermore, an alignment method assisted by mechanical shearing has been assessed. The CNT suspension was placed between two glass slides and rubbed along the opposite direction to apply shear force (Figure 1.6). Another approach involved the use of a simple dip-coating method without any equipment or and complex apparatuses (Figure 1.7). This method utilized microfluidics, including capillary condensation and surface tension, to obtain aligned CNTs.

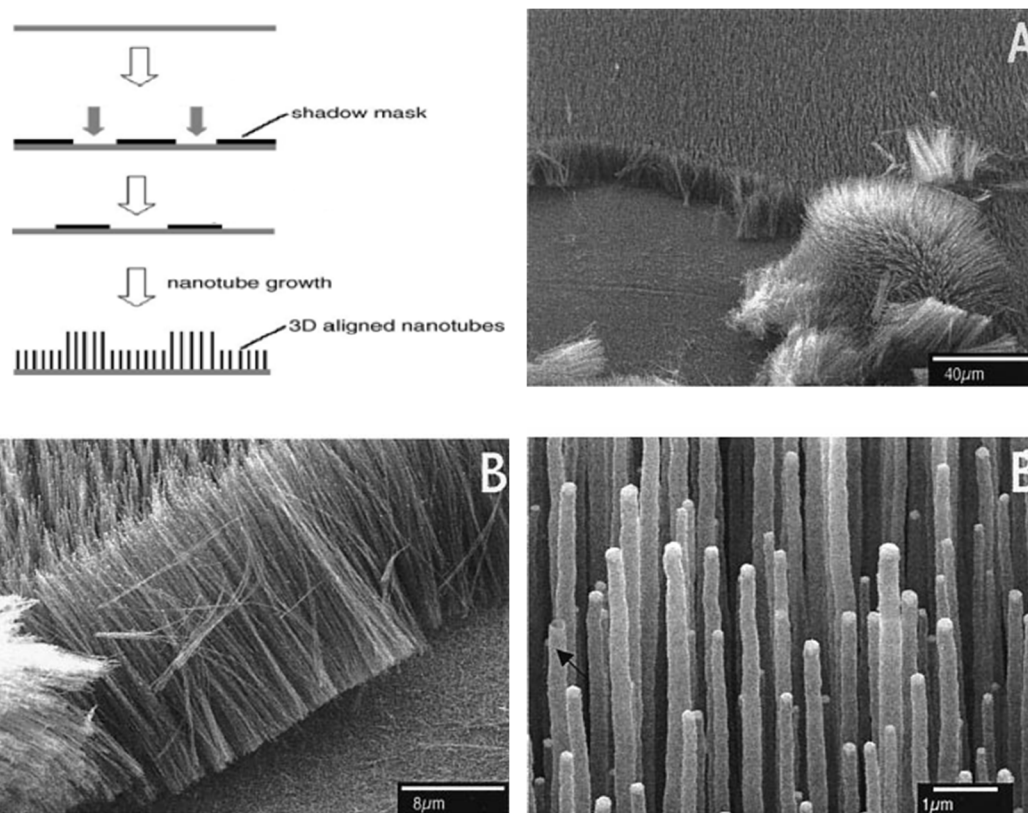


Fig. 1.4. CVD-grown aligned CNTs on a template substrate.³³

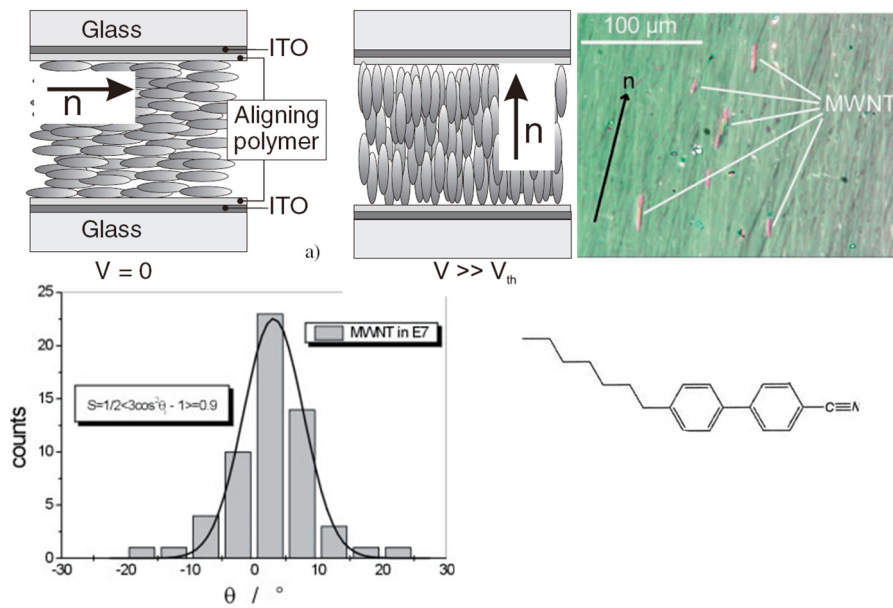


Fig. 1.5. MWNTs dispersed in nematic-liquid-crystal solvents (E7) with an external field.^{48,49}

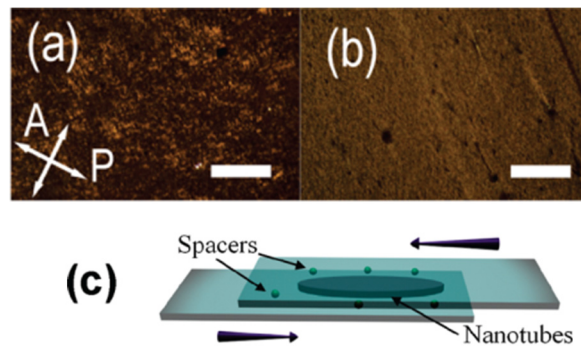


Fig. 1.6. Alignment method of CNTs dispersed in a solvent with the application of shear force; optical images of glass with (a) and without (b) polarizer.⁴⁴

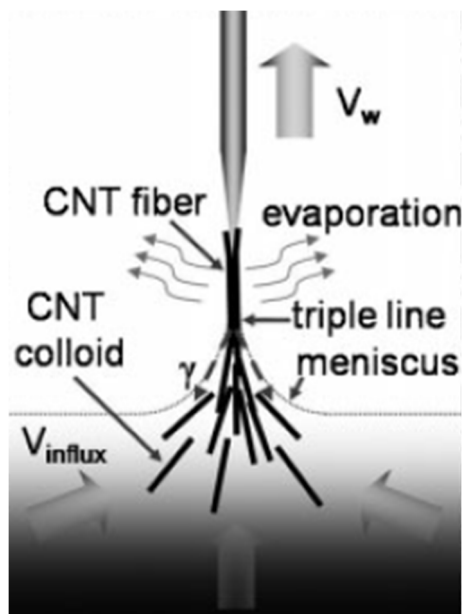


Fig. 1.7. Schematic of the formation mechanism of aligned CNT fiber.⁴⁷

1.2.2.2 Engineered interaction forces between CNTs

Previous approaches to add interaction forces to CNTs based on the van der Waals force are briefly categorized as those involving covalent and noncovalent interaction. The first method is represented by direct crosslinking between CNTs.⁵⁰ CVD-grown aligned CNTs can be drawn to make CNT fiber. CNT fibers are then inter-connected by crosslinking molecules to form covalent bonds. The second method involves the grafting of new functional groups onto the surfaces of CNTs. CNTs are chemically modified to have acid and base groups, after which the CNTs act as a weak polyelectrolyte.⁵¹ In this case, CNTs were also separately modified to have carboxylic acid groups and amine groups, resulting in a well-dispersed solution. Negatively and positively charged CNTs were used to create a 100% CNT thin film given their electrostatic force without additional organic molecules, as shown in Figure 1.8. The thickness and surface topology of the film were controlled by the pH.

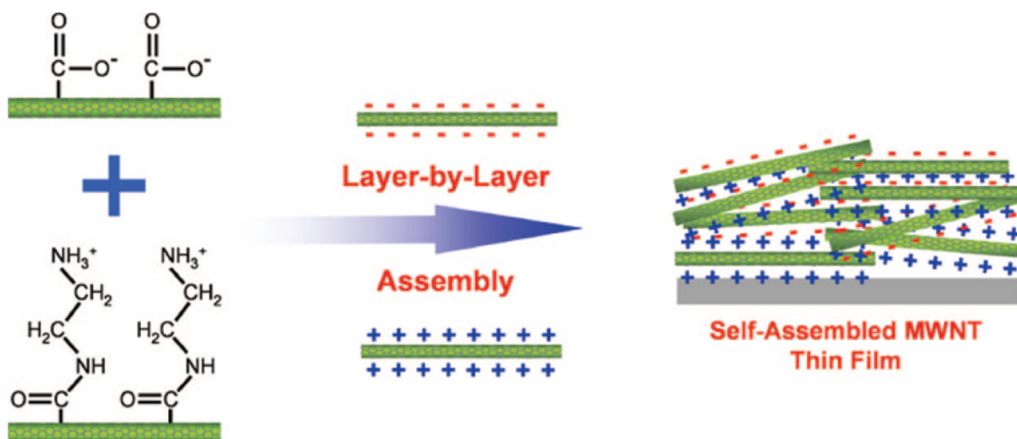


Fig. 1.8. Scheme of the layer-by-layer (LBL) method.

1.2.3 Issues associated with nanostructure engineering for high strength CNT films

The alignment, packing density, strong interaction force, and the crosslinking density are the key parameters for high-strength CNT film. However, despite numerous attempts to fabricate CNT films, several challenges remain to be overcome with regard to commercialization. Although an in-situ CVD method to obtain well-aligned CNT materials with high mechanical properties succeeded, scalability remains a challenge due to the high cost of the synthesis process and the complex apparatus required. Unfortunately, the resultant CNT products created by the alignment method based on a wet process have shown a low degree of alignment and a low packing density, making them unsuitable for application as a structural material. Furthermore, previously reported methods which attempted to add interaction forces have not led to significant enhancements, as CVD-grown CNTs generally lack functional groups on their surfaces, resulting in low-density crosslinking. The surface modifications for functionalization also destroyed the aligned nanostructure of the CNTs.

In an attempt to achieve long-range alignment and a high packing density, the spontaneous formation of an ordered phase of a CNT suspension was suggested and experimentally observed above the critical concentration, according to Onsager's theory for rigid rod-like particles.⁵² These findings regarding the liquid crystalline behavior have opened new paths for the alignment of disordered CNTs. However, a liquid crystalline solution of CNTs is difficult to obtain owing to the complicated process required, which hinders the realization of their full potential. Considering this situation, a facile processing method based on a wet process for self-aligned CNTs with a high packing density and strong interaction force is required.

1.3 CNT based composite films for flexible energy storage applications

1.3.1 Fundamentals and theory of a flexible supercapacitor

1.3.1.1 Supercapacitor electrode

With the increasing depletion of fossil fuels, climate change and severe environmental pollution, there is a need for environmentally friendly, sustainable, and renewable energy storage systems as new power sources. In many energy storage applications, supercapacitors (known as electrochemical capacitors)⁵³ have attracted much attention as energy sources for hybrid electric vehicles, uninterruptable power supplies, and portable electronics. The electrochemical performance capabilities of supercapacitors are such that they are ranked between those of batteries and conventional capacitors (Figure 1.9).⁵⁴ Supercapacitors possess higher power density levels and faster charge/discharge rates and long life cycles compared to batteries. However, as new technologies for various vehicle systems and electronic devices are developed, supercapacitors with high performance levels are urgently required.

Supercapacitors can be roughly classified into two types according to their energy storage mechanism. Electrical double-layer capacitors (EDLCs) store charges at the interface between the electrode surface and electrolyte. Because storage in this case depends on the electrostatic adsorption of ions, the key issue to increase the capacitance is to use an electrode with a high specific surface area, good electronic conductivity and a porous structure. Porous carbon scaffolds including activated carbon,⁵⁵ graphite⁵⁶ and CNTs⁵⁷ have been considered as promising electrode materials. However, their specific surface areas are limited, and their low energy density presents a challenge. Pseudocapacitors store charges by rapid and reversible faradaic (redox) reactions of

active electrode materials. Transition metal oxides such as RuO₂ and MnO₂ as well as conducting polymers have shown higher energy densities compared to those of carbon materials based on the electric double layer capacitance. However, their low conductivity, poor stability, and weightiness are known to be unsolved critical problems. For these reasons, current collectors such as metal foam have been studied for effective charge transfers.⁵⁸ In addition, while the deposition of metal oxides and conducting polymers on conductive, supporting carbon materials, including CNTs, reduced graphene oxide (GO), and carbon fiber (CF) have displayed enhanced capacitance,⁵⁹⁻⁶² the low cycle capability and high cost in these cases remain as barriers to commercialization.

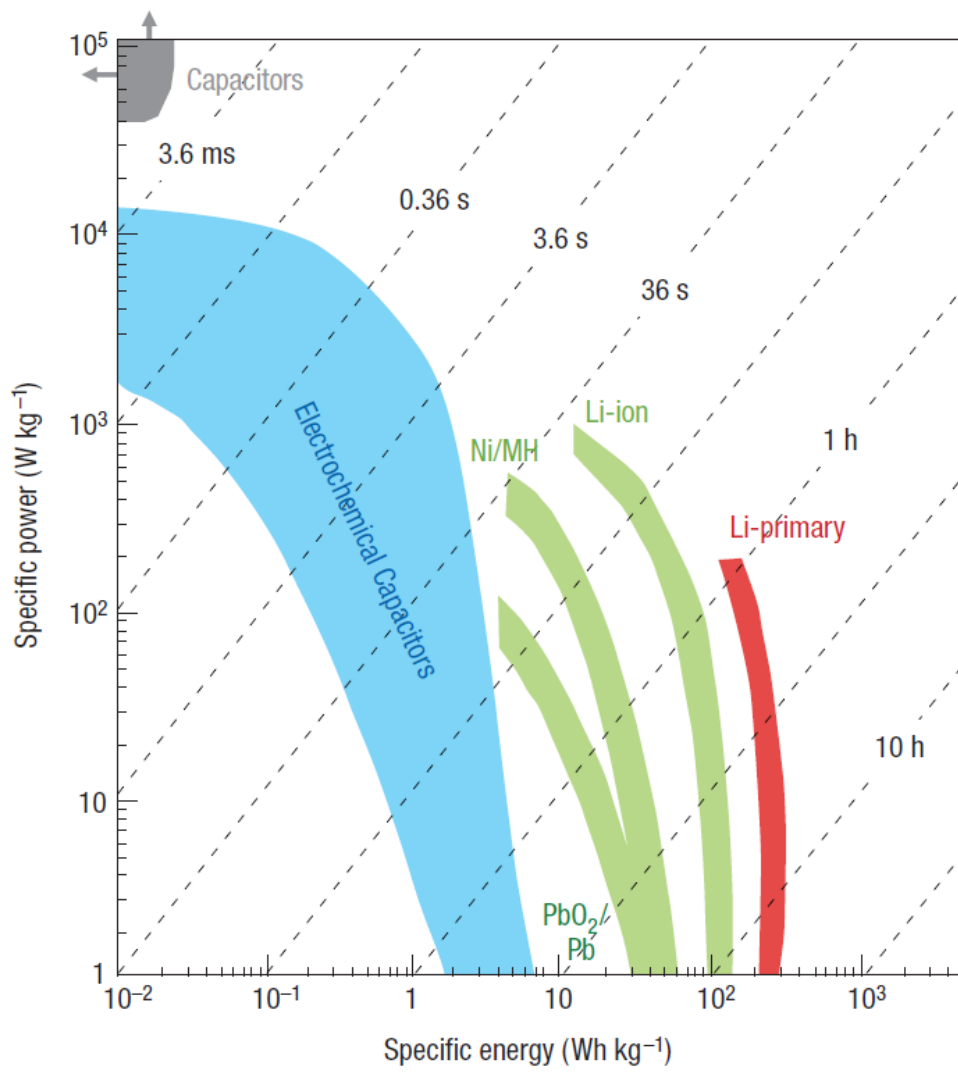


Fig. 1.9. Comparison of energy storage systems.

1.3.1.2 State-of-the-art works on CNT based flexible supercapacitor electrode

As various flexible electronic systems, including bendable displays and wearable e-textile/clothing applications are developed, energy devices require active electrodes which can be twisted, folded, rolled and stretched to fit into tight places without a loss of performance. Nickel and aluminum foam, which have been used as conventional supporting materials for metal oxides, cannot be applied to a flexible energy storage system. Hence, a supercapacitor electrode based on carbon nanomaterials is at present an emerging candidate supporting material for flexible energy storage and power supply systems.

With reference to many carbon nanomaterials, CNT-based flexible supercapacitors have been studied extensively due to their high electrical conductivity and their high mechanical strength. CNT-dispersed suspensions have been suggested as a functional ink to coat flexible and porous but nonconductive substrates (e.g., cotton, plastic film, and cellulose paper).⁵⁹⁻⁶² Cotton textiles are easily coated by dipping them into a CNT-dispersed suspension.⁶³ CNT-coated textiles show high flexibility and increased electrical conductivity with an increase in the dipping time. CNTs were also spray-coated onto polyethylene-terephthalate (PET) films and used as both electrodes and current collectors.⁶⁴

Randomly oriented buckypaper, which is composed of CNTs, has been studied as a freestanding electrode. However, its very low strength due to its porous structure and its high resistance from the relatively few contact points between the CNTs causes a slow charge transfer. Vertically aligned CNTs (VA-CNTs) synthesized on Si wafers have fulfilled the need for high strength and good rate capability.⁶⁵⁻⁶⁸ Furthermore, oxidized nickel nanoparticles were deposited on VA-CNTs to increase the energy density of the

electrode.⁶⁹ Agglomeration during the metal oxide deposition process was observed, and control of the metal-loading quantity was difficult due to the lack of functional groups on the VA-CNTs, which resulting in a low energy density level.

1.3.2 Issues associated with flexible supercapacitors

The energy density, power density, cycle stability as well as the mechanical strength, flexibility and integrity are the key parameters to consider when attempting to create flexible energy devices. However, conventional supercapacitor electrodes such as metal foam, activated carbons, graphite cannot be utilized in flexible supercapacitors due to their low strength and poor flexibility. They become degraded and lose their capacitance when they are bent, folded or stretched. Recent studies have introduced freestanding CNT-based electrodes which are promising for use as a flexible supercapacitor. CNT buckypaper has the advantages of a low-cost fabrication process and a porous structure. However, the introduction of a surfactant or a surface treatment to fabricate buckypaper decreases the intrinsic electrical conductivity, and the low strength and low energy density have hindered the practical application of this material. While VA-CNTs demonstrate high electrical conductivity, mechanical strength and flexibility, controlling the loading of pseudocapacitive materials onto VA-CNTs is very complicated. In this respect, a multifunctional material which combines high mechanical properties and electrochemical performances is needed for application to flexible energy storage systems.

1.4 Aim and scope of this research

This study focuses on designing and developing a means of preparing high-strength CNT films based on theoretical considerations. The preparation methodology provides a self-assembly approach to control the orientation, interaction force and surface chemistry of CNTs and a versatile route for future applications.

1.4.1 Theoretical study of the strength of CNT films

The theoretical approach regarding the strength of CNT films will be discussed in **Chapter 2**. First, a new equation to determine the strength of CNT films is introduced and theoretically assessed considering the important parameters and the relationship between the strength of the CNT films and the influencing factors, such as the orientation, packing density and interaction force. In addition, the reliability of the newly developed equation is verified by carrying out theoretical calculations of the strength of CNT films and by comparing these results with previous results. Through this theoretical study, an ideal structure and the properties of the high strength CNT films are proposed.

1.4.2 Preparation and characterization of highly aligned, high-density CNT films

Highly aligned CNTs with a densely packed nanostructure are assembled in the form of a sheet by a facile filtration process. The spontaneous self-alignment behavior of the CNTs based on an isotropic-nematic transition is controlled to align the CNTs in a suspension. The mechanism behind this will be discussed in **Chapter 3**. The proposed method leads to the self-alignment behavior of CNTs in an aqueous solution regardless of the surface modification methods or the types of CNTs used.

1.4.3 Preparation and characterization of bone-mimicking GO@CNT hybrid films

Nearly monolayered smaller GO-incorporated CNT films are developed to form an effective type of load-bearing hybrid architecture. The nanostructural design of the hybrid film focuses on the mimicking of collagen fibril in natural bone, which has unique load-bearing characteristics. The new approach for the homogeneous crosslinking reaction between CNT and GO is developed and discussed in **Chapter 4**.

1.4.4 Preparation and characterization of flexible, high strength freestanding, pseudocapacitive CNT film by metal-bio coordination method

The hybridization of natural polyphenol “tannic acid” (TA) and CNT is investigated to combine high strength and good energy storage ability in a hybrid film. TA is versatile for the wrapping and crosslinking of CNTs through the development of a metal-bio coordination complex and pseudocapacitance in the hybrid CNT film. The preparation method and mechanical/electrochemical performance of the TA@CNT film will be investigated in **Chapter 5**.

1.5 References

1. Geim, A. K.; Novoselov, K. S., The Rise of Graphene. *Nat. Mater.* **2007**, *6*, 183-191.
2. Bianco, A.; Cheng, H. M.; Enoki, T.; Gogotsi, Y.; Hurt, R. H.; Koratkar, N.; Kyotani, T.; Monthieux, M.; Park, C. R.; Tascon, J. M. D.; Zhang, J., All in the Graphene Family - A Recommended Nomenclature for Two-Dimensional Carbon Materials. *Carbon* **2013**, *65*, 1-6.
3. Peng, B.; Locascio, M.; Zapol, P.; Li, S. Y.; Mielke, S. L.; Schatz, G. C.; Espinosa, H. D., Measurements of Near-ultimate Strength for Multiwalled Carbon Nanotubes and Irradiation-induced Crosslinking Improvements. *Nat. Nanotechnol.* **2008**, *3*, 626-631.
4. Yu, M. F.; Files, B. S.; Arepalli, S.; Ruoff, R. S., Tensile Loading of Ropes of Single Wall Carbon Nanotubes and their Mechanical Properties. *Phys. Rev. Lett.* **2000**, *84*, 5552-5555.
5. Yu, M. F.; Lourie, O.; Dyer, M. J.; Moloni, K.; Kelly, T. F.; Ruoff, R. S., Strength and Breaking Mechanism of Multiwalled Carbon Nanotubes under Tensile Load. *Science* **2000**, *287*, 637-640.
6. Coleman, J. N.; Khan, U.; Blau, W. J.; Gun'ko, Y. K., Small but strong: A Review of the Mechanical Properties of Carbon Nanotube-Polymer Composites. *Carbon* **2006**, *44*, 1624-1652.
7. Oh, J. Y.; Choi, Y. S.; Yang, S. J.; Kim, J.; Choi, H. S.; Choi, G. D.; Yun, C. H.; Lee, B. K.; Park, C. R., Effect of Microstructure and Morphological Properties of Carbon Nanotubes on the Length Reduction during Melt Processing. *Compos. Sci. Technol.* **2015**, *112*, 42-49.
8. De Volder, M. F. L.; Tawfick, S. H.; Baughman, R. H.; Hart, A. J., Carbon

- Nanotubes: Present and Future Commercial Applications. *Science* **2013**, *339*, 535-539.
9. Jiang, K. L.; Li, Q. Q.; Fan, S. S., Nanotechnology: Spinning Continuous Carbon Nanotube Yarns - Carbon Nanotubes Weave Their Way into a Range of Imaginative Macroscopic Applications. *Nature* **2002**, *419*, 801-801.
 10. Zhang, M.; Atkinson, K. R.; Baughman, R. H., Multifunctional carbon nanotube yarns by downsizing an ancient technology. *Science* **2004**, *306*, 1358-1361.
 11. Kim, S. W.; Kim, T.; Kim, Y. S.; Choi, H. S.; Lim, H. J.; Yang, S. J.; Park, C. R., Surface modifications for the effective dispersion of carbon nanotubes in solvents and polymers. *Carbon* **2012**, *50*, 3-33.
 12. Dujardin, E.; Ebbesen, T. W.; Krishnan, A.; Treacy, M. M. J., Purification of single-shell nanotubes. *Adv. Mater.* **1998**, *10*, 611-+.
 13. Yang, S. J.; Choi, J. Y.; Chae, H. K.; Cho, J. H.; Nahm, K. S.; Park, C. R., Preparation and Enhanced Hydrostability and Hydrogen Storage Capacity of CNT@MOF-5 Hybrid Composite. *Chem. Mater.* **2009**, *21*, 1893-1897.
 14. Yang, S. J.; Park, C. R., Facile preparation of monodisperse ZnO quantum dots with high quality photoluminescence characteristics. *Nanotechnology* **2008**, *19*, 035609.
 15. Oh, J. Y.; Jee, S. H.; Kakati, N.; Kim, S. H.; Song, M. J.; Yoon, Y. S., Hydrothermal Synthesis of Pt-Ru-W Anode Catalyst Supported on Multi-Walled Carbon Nanotubes for Methanol Oxidation Fuel Cell (vol 49, 115101, 2010). *Jpn. J. Appl. Phys.* **2012**, *51*, 115101.
 16. Khabashesku, V. N.; Billups, W. E.; Margrave, J. L., Fluorination of single-wall carbon nanotubes and subsequent derivatization reactions. *Accounts Chem. Res.* **2002**, *35*, 1087-1095.
 17. Marcoux, P. R.; Schreiber, J.; Batail, P.; Lefrant, S.; Renouard, J.; Jacob, G.; Albertini, D.; Mevellec, J. Y., A spectroscopic study of the fluorination and

- defluorination reactions on single-walled carbon nanotubes. *Phys. Chem. Chem. Phys.* **2002**, *4*, 2278-2285.
18. Lim, J. K.; Yun, W. S.; Yoon, M. H.; Lee, S. K.; Kim, C. H.; Kim, K.; Kim, S. K., Selective thiolation of single-walled carbon nanotubes. *Synthetic Met.* **2003**, *139*, 521-527.
19. Hamon, M. A.; Hui, H.; Bhowmik, P.; Itkis, H. M. E.; Haddon, R. C., Ester-functionalized soluble single-walled carbon nanotubes. *Appl. Phys. a-Mater* **2002**, *74*, 333-338.
20. Hennrich, F.; Lebedkin, S.; Malik, S.; Tracy, J.; Barczewski, M.; Rosner, H.; Kappes, M., Preparation, characterization and applications of free-standing single walled carbon nanotube thin films. *Phys. Chem. Chem. Phys.* **2002**, *4*, 2273-2277.
21. Riggs, J. E.; Guo, Z. X.; Carroll, D. L.; Sun, Y. P., Strong luminescence of solubilized carbon nanotubes. *J. Am. Chem. Soc.* **2000**, *122*, 5879-5880.
22. Sun, Y. P.; Huang, W. J.; Lin, Y.; Fu, K. F.; Kitaygorodskiy, A.; Riddle, L. A.; Yu, Y. J.; Carroll, D. L., Soluble dendron-functionalized carbon nanotubes: Preparation, characterization, and properties. *Chem. Mater.* **2001**, *13*, 2864-2869.
23. Etika, K. C.; Jochum, F. D.; Theato, P.; Grunlan, J. C., Temperature Controlled Dispersion of Carbon Nanotubes in Water with Pyrene-Functionalized Poly(N-cyclopropylacrylamide). *J. Am. Chem. Soc.* **2009**, *131*, 13598.
24. Giulianini, M.; Waclawik, E. R.; Bell, J. M.; De Crescenzi, M.; Castrucci, P.; Scarselli, M.; Motta, N., Regioregular poly(3-hexyl-thiophene) helical self-organization on carbon nanotubes. *Appl. Phys. Lett.* **2009**, *95*, 013304.
25. Yan, Y. H.; Cui, J. A.; Potschke, P.; Voit, B., Dispersion of pristine single-walled carbon nanotubes using pyrene-capped polystyrene and its application for preparation of polystyrene matrix composites. *Carbon* **2010**, *48*, 2603-2612.

26. Guo, Z.; Mao, J.; Ouyang, Q.; Zhu, Y. Z.; He, L.; Lv, X.; Liang, L.; Ren, D. M.; Chen, Y. S.; Zheng, J. Y., Noncovalent Functionalization of Single-Walled Carbon Nanotube by Porphyrin: Dispersion of Carbon Nanotubes in Water and Formation of Self-Assembly Donor-Acceptor Nanoensemble. *J. Disper. Sci. Technol.* **2010**, *31*, 57-61.
27. Oh, J. Y.; Choi, H. S.; Kim, M. S.; Kim, Y. S.; Park, C. R., Effects of morphological characteristics of Pt nanoparticles supported on poly(acrylic acid)-wrapped multiwalled carbon nanotubes on electrochemical performance of direct methanol fuel cells. *J. Mater. Res.* **2012**, *27*, 2035-2045.
28. Wang, R. R.; Sun, J.; Gao, L. A.; Zhang, J., Dispersion of single-walled carbon nanotubes by DNA for preparing transparent conductive films. *J. Mater. Chem.* **2010**, *20*, 6903-6909.
29. Zheng, M.; Jagota, A.; Semke, E. D.; Diner, B. A.; Mclean, R. S.; Lustig, S. R.; Richardson, R. E.; Tassi, N. G., DNA-assisted dispersion and separation of carbon nanotubes. *Nat. Mater.* **2003**, *2*, 338-342.
30. Hearle, J. W. S., Structural Mechanics of Fibers. *J. Polym. Sci. Pol. Sym.* **1967**, *215*.
31. Hearle, J. W. S., A critical review of the structural mechanics of wool and hair fibres. *Int. J. Biol. Macromol.* **2000**, *27*, 123-138.
32. Hearle, J. W. S.; Grosberg, P.; Backer, S., *Structural mechanics of fibers, yarns, and fabrics*. Wiley-Interscience: New York,, 1969; p v.
33. Ren, Z. F.; Huang, Z. P.; Xu, J. W.; Wang, J. H.; Bush, P.; Siegal, M. P.; Provencio, P. N., Synthesis of large arrays of well-aligned carbon nanotubes on glass. *Science* **1998**, *282*, 1105-1107.
34. Kaida, S.; Matsui, J.; Sagae, T.; Hoshikawa, Y.; Kyotani, T.; Miyashita, T., The

production of large scale ultrathin aligned CNT films by combining AC electric field with liquid flow. *Carbon* **2013**, *59*, 503-511.

35. Kordas, K.; Mustonen, T.; Toth, G.; Vahakangas, J.; Uusimaki, A.; Jantunen, H.; Gupta, A.; Rao, K. V.; Vajtai, R.; Ajayan, P. M., Magnetic-field induced efficient alignment of carbon nanotubes in aqueous solutions. *Chem. Mater.* **2007**, *19*, 787-791.

36. Park, J. U.; Meitl, M. A.; Hur, S. H.; Usrey, M. L.; Strano, M. S.; Kenis, P. J. A.; Rogers, J. A., In situ deposition and patterning of single-walled carbon nanotubes by Laminar flow and controlled flocculation in microfluidic channels. *Angew. Chem. Int. Edit.* **2006**, *45*, 581-585.

37. Smith, B. W.; Benes, Z.; Luzzi, D. E.; Fischer, J. E.; Walters, D. A.; Casavant, M. J.; Schmidt, J.; Smalley, R. E., Structural anisotropy of magnetically aligned single wall carbon nanotube films. *Appl. Phys. Lett.* **2000**, *77*, 663-665.

38. Wang, B.; Ma, Y. F.; Li, N.; Wu, Y. P.; Li, F. F.; Chen, Y. S., Facile and Scalable Fabrication of Well-Aligned and Closely Packed Single-Walled Carbon Nanotube Films on Various Substrates. *Adv. Mater.* **2010**, *22*, 3067-3070.

39. Yu, G. H.; Cao, A. Y.; Lieber, C. M., Large-area blown bubble films of aligned nanowires and carbon nanotubes. *Nat. Nanotechnol.* **2007**, *2*, 372-377.

40. Fu, W. Q.; Liu, L.; Jiang, K. L.; Li, Q. Q.; Fan, S. S., Super-aligned carbon nanotube films as aligning layers and transparent electrodes for liquid crystal displays. *Carbon* **2010**, *48*, 1876-1879.

41. Mrozek, R. A.; Kim, B. S.; Holmberg, V. C.; Taton, T. A., Homogeneous, coaxial liquid crystal domain growth from carbon nanotube seeds. *Nano Lett.* **2003**, *3*, 1665-1669.

42. Russell, J. M.; Oh, S. J.; LaRue, I.; Zhou, O.; Samulski, E. T., Alignment of nematic liquid crystals using carbon nanotube films. *Thin Solid Films* **2006**, *509*, 53-57.

43. Allen, R.; Fuller, G. G.; Bao, Z. N., Aligned SWNT Films from Low-Yield Stress Gels and Their Transparent Electrode Performance. *ACS Appl. Mater. Inter.* **2013**, *5*, 7244-7252.
44. Zamora-Ledezma, C.; Blanc, C.; Maugey, M.; Zakri, C.; Poulin, P.; Anglaret, E., Anisotropic Thin Films of Single-Wall Carbon Nanotubes from Aligned Lyotropic Nematic Suspensions. *Nano Lett.* **2008**, *8*, 4103-4107.
45. Vigolo, B.; Penicaud, A.; Coulon, C.; Sauder, C.; Pailler, R.; Journet, C.; Bernier, P.; Poulin, P., Macroscopic fibers and ribbons of oriented carbon nanotubes. *Science* **2000**, *290*, 1331-1334.
46. Ko, H.; Tsukruk, V. V., Liquid-crystalline processing of highly oriented carbon nanotube arrays for thin-film transistors. *Nano Lett.* **2006**, *6*, 1443-1448.
47. Jang, E. Y.; Kang, T. J.; Im, H.; Baek, S. J.; Kim, S.; Jeong, D. H.; Park, Y. W.; Kim, Y. H., Macroscopic Single-Walled-Carbon-Nanotube Fiber Self-Assembled by Dip-Coating Method *Adv. Mater.* **2010**, *22*, 1552-1552.
48. Dierking, I.; Scalia, G.; Morales, P.; LeClere, D., Aligning and reorienting carbon nanotubes with nematic liquid crystals. *Adv. Mater.* **2004**, *16*, 865-869.
49. Lagerwall, J.; Scalia, G.; Haluska, M.; U.; Roth, S.; Giesselmann, F., Nanotube alignment using lyotropic liquid crystals. *Adv. Mater.* **2007**, *19*, 359-364.
50. Jiang, K. L.; Wang, J. P.; Li, Q. Q.; Liu, L. A.; Liu, C. H.; Fan, S. S., Superaligned Carbon Nanotube Arrays, Films, and Yarns: A Road to Applications. *Adv Mater* **2011**, *23*, 1154-1161.
51. Lee, S. W.; Kim, B. S.; Chen, S.; Shao-Horn, Y.; Hammond, P. T., Layer-by-Layer Assembly of All Carbon Nanotube Ultrathin Films for Electrochemical Applications. *J. Am. Chem. Soc.* **2009**, *131*, 671-679.
52. Onsager, L., The Effects of Shape on the Interaction of Colloidal Particles. *Ann.*

Ny. Acad. Sci. **1949**, *51*, 627-659.

53. Wang, G. P.; Zhang, L.; Zhang, J. J., A review of electrode materials for electrochemical supercapacitors. *Chem. Soc. Rev.* **2012**, *41*, 797-828.

54. Simon, P.; Gogotsi, Y., Materials for electrochemical capacitors. *Nat Mater* **2008**, *7*, 845-854.

55. Huang, X. W.; Xie, Z. W.; He, X. Q.; Sun, H. Z.; Tong, C. Y.; Xie, D. M., Electric double layer capacitors using activated carbon prepared from pyrolytic treatment of sugar as their electrodes. *Synthetic Met.* **2003**, *135*, 235-236.

56. Gomibuchi, E.; Ichikawa, T.; Kimura, K.; Isobe, S.; Nabeta, K.; Fujii, H., Electrode properties of a double layer capacitor of nano-structured graphite produced by ball milling under a hydrogen atmosphere. *Carbon* **2006**, *44*, 983-988.

57. Katakabe, T.; Kaneko, T.; Watanabe, W.; Fukushima, T.; Aida, T., Electric double-layer capacitors using "bucky gels" consisting of an ionic liquid and carbon nanotubes. *J. Electrochem. Soc.* **2005**, *152*, A1913-A1916.

58. Yu, L.; Zhang, G. Q.; Yuan, C. Z.; Lou, X. W., Hierarchical NiCo₂O₄@MnO₂ core-shell heterostructured nanowire arrays on Ni foam as high-performance supercapacitor electrodes. *Chem. Commun.* **2013**, *49*, 137-139.

59. Bi, R. R.; Wu, X. L.; Cao, F. F.; Jiang, L. Y.; Guo, Y. G.; Wan, L. J., Highly Dispersed RuO₂ Nanoparticles on Carbon Nanotubes: Facile Synthesis and Enhanced Supercapacitance Performance. *J. Phys. Chem. C* **2010**, *114*, 2448-2451.

60. Wang, H. L.; Casalongue, H. S.; Liang, Y. Y.; Dai, H. J., Ni(OH)₂ Nanoplates Grown on Graphene as Advanced Electrochemical Pseudocapacitor Materials. *J. Am. Chem. Soc.* **2010**, *132*, 7472-7477.

61. Yang, L.; Cheng, S.; Ding, Y.; Zhu, X. B.; Wang, Z. L.; Liu, M. L., Hierarchical Network Architectures of Carbon Fiber Paper Supported Cobalt Oxide Nanonet for

- High-Capacity Pseudocapacitors. *Nano Lett.* **2012**, *12*, 321-325.
62. Zhang, X. J.; Shi, W. H.; Zhu, J. X.; Kharistal, D. J.; Zhao, W. Y.; Lalia, B. S.; Hng, H. H.; Yan, Q. Y., High-Power and High-Energy-Density Flexible Pseudocapacitor Electrodes Made from Porous CuO Nanobelts and Single-Walled Carbon Nanotubes *ACS Nano* **2011**, *5*, 5280-5280.
63. Hu, L. B.; Pasta, M.; La Mantia, F.; Cui, L. F.; Jeong, S.; Deshazer, H. D.; Choi, J. W.; Han, S. M.; Cui, Y., Stretchable, Porous, and Conductive Energy Textiles. *Nano Lett.* **2010**, *10*, 708-714.
64. Kaempgen, M.; Chan, C. K.; Ma, J.; Cui, Y.; Gruner, G., Printable Thin Film Supercapacitors Using Single-Walled Carbon Nanotubes. *Nano Lett.* **2009**, *9*, 1872-1876.
65. Dai, L. M.; Patil, A.; Gong, X. Y.; Guo, Z. X.; Liu, L. Q.; Liu, Y.; Zhu, D. B., Aligned nanotubes. *Chemphyschem* **2003**, *4*, 1150-1169.
66. Ghosh, A.; Le, V. T.; Bae, J. J.; Lee, Y. H., TLM-PSD model for optimization of energy and power density of vertically aligned carbon nanotube supercapacitor. *Sci. Rep-Uk* **2013**, *3*.
67. Lin, H. J.; Li, L.; Ren, J.; Cai, Z. B.; Qiu, L. B.; Yang, Z. B.; Peng, H. S., Conducting polymer composite film incorporated with aligned carbon nanotubes for transparent, flexible and efficient supercapacitor. *Sci. Rep-Uk* **2013**, *3*.
68. Ye, J. S.; Cui, H. F.; Liu, X.; Lim, T. M.; Zhang, W. D.; Sheu, F. S., Preparation and characterization of aligned carbon nanotube-ruthenium oxide nanocomposites for supercapacitors. *Small* **2005**, *1*, 560-565.
69. Jiang, Y. Q.; Wang, P. B.; Zang, X. N.; Yang, Y.; Kozinda, A.; Lin, L. W., Uniformly Embedded Metal Oxide Nanoparticles in Vertically Aligned Carbon Nanotube Forests as Pseudocapacitor Electrodes for Enhanced Energy Storage. *Nano Lett.* **2014**, *14*, 2230-2230.

Chapter 2 Theoretical Approach and Prediction of the High Strength CNT Film

2.0 Major symbols

σ_{film} : Film tensile strength

σ_{CNT} : CNT tensile strength

D : Diameter of CNT

F_{CNT} : Force applied to all CNTs in the film

f_{CNT} : Force applied to an individual CNT

ϕ : Packing density of the CNT film

A_{film} : Cross-sectional area of the film

A_{CNT} : cross-sectional area of the CNTs which constitute the film

α : Empirical correction coefficient

I_{CNT} : Interaction force factor

I_{vdW} : van der Waals force per unit length

d_{CL} : Density of cross-links per unit length

I_E : Engineered attraction force per unit length

2.1 Theoretical consideration relevant to CNT based high strength films

In spite of the tremendous effort expended, earlier work continues to face the challenge of enhancing the mechanical performance of CNT-based films. Therefore, theoretical considerations are among the most important issues in the design and preparation of high-performance CNT films. Unfortunately, few theoretical models which account for nanomechanics are available, as previously reported theories cannot be applied to films composed of nanomaterials, as the models do not take into account the high surface-to-the volume ratio of the nanomaterials or the interaction forces. A new equation regarding certain fiber properties, including the surface-to-volume ratio, the length and the diameter as well as structural parameters such as the alignment, packing density, and interaction force between the CNTs is needed for accurate predictions of the strength of CNT films.

Equations (1.1) and (1.2) inspire us to develop a new theoretical equation to predict the tensile strength of CNT films. When we consider that yarn strength equations derive from the force per unit cross-sectional area, the tensile strength of the film (σ_{film}) can be determined as follows:

$$\sigma_{film} = \frac{\Sigma F_{CNT}}{A_{film}} \quad (2.1)$$

Here, A_{film} is the cross-sectional area of the film and F_{CNT} is force on all CNTs. Then, A_{film} can be expressed with the packing density, as follows:

$$A_{film} = \frac{\Sigma A_{CNT}}{\phi} \quad (2.2)$$

In this equation, ϕ and A_{CNT} are the packing density (Figure 2.1) and the sum of the cross-sectional area of the CNTs composing the film, respectively. When it is assumed that the CNTs have identical lengths and diameters and an identical position distribution in the film, the sum of the force applied onto all CNTs in equation (2.1) is determined as follows,

$$\Sigma F_{CNT} = a \cdot I_{CNT} \sum_i f_i \cos \varphi_i \quad (2.3)$$

$$= a \cdot I_{CNT} \sum_i \sigma_{CNT} \pi \left(\frac{D}{2}\right)^2 \cos \varphi_i \quad (2.4)$$

where σ_{CNT} , f_{CNT} , a , and φ_i are respectively the CNT tensile strength, the force on an individual CNT, the correction constant (a is 1 when the thickness of the CNT film is less than 1 μm and 0.5 when the thickness of CNT film exceeds 1 μm) and the tube orientation angle along the tensile load axis (Figure 2.2). I_{CNT} is a parameter associated with the interaction between the CNTs; it is expressed as follows,

$$I_{CNT} = \frac{I_{real}}{I_{ideal}} = \frac{I_{vdW} + d_{CL} I_E}{I_{ideal}} \quad (2.5)$$

where I_{real} , I_{ideal} and I_{vdW} are the real, ideal and van der Waals interaction forces between the CNTs. Considering a situation in which the CNTs interact not by forming covalent

C-C bonds but by weak van der Waals force, I_{CNT} reflects the deviation of the interaction force between the real and ideal cases. Although the intrinsic interaction force of CNTs is the van der Waals force, additional engineered crosslinking including covalent bonds, hydrogen bonds and electrostatic interaction can be introduced between the CNTs, thus enhancing the interaction forces. Here, d_{CL} and I_E denote the density of the cross-link per unit length and the engineered attraction force, respectively. The strength of the engineered interaction force can be determined according to the type of interaction force, as shown in Table 2.1, and I_{CNT} can be increased according to the design and engineering of the density of the crosslinking and the type of interaction force.

The developed equations originate from a rough prediction of the tensile strength of CNT films. However, the proportional relationship regarding the tensile properties can provide a guideline for the design and preparation of high-strength CNT films via the engineering of the above parameters. As CNTs have a more aligned nanostructure, they form a close-packed nanostructure which facilitates maximum contact and van der Waals force between the tubes with a high packing density. In addition, when a certain number of crosslinks are formed between the tubes, efficient stress transfer will likely make the film stronger.

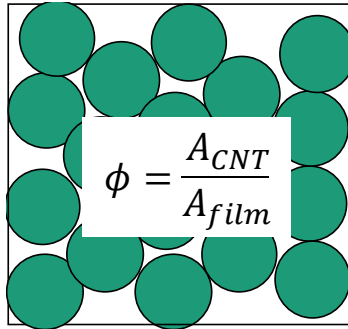


Fig. 2.1. The packing density of CNT film.

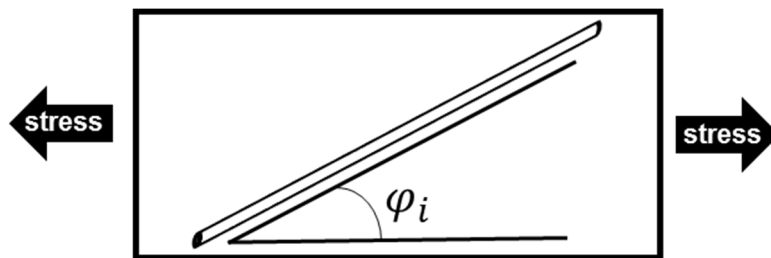


Fig. 2.2. The degree of CNT alignment along the tensile load axis.

Table 2.1. Comparison of the interaction energy levels

Interactions	kJ/mol
van der Waals	4
Covalent (C-C)	347
Covalent (amide)	305
Coordination	20
Hydrogen	12

2.2 Comparison of theoretical prediction and experimental results

From the developed equations, theoretical calculations can be carried out for various cases. In order to confirm the reliability of the equations, the previously reported experimental conditions are substituted into the equations and the results are compared with the calculated values, as shown in Figure 2.3. When the case of an individual CNT tube^{1,2} is applied to the equation, an identical strength level of 30 GPa results. Meanwhile, the theoretically predicted strength of a randomly oriented bulk CNT film³ sample is 10 MPa compared to the experimentally reported values, thus showing a dramatic decrease in the strength due to the random orientation and weak interactions.

Inoue et al.⁴ fabricated well-aligned CNT films through the stacking of aligned CNT webs. The resultant films displayed good anisotropic mechanical performance along the tensile axis. The strength of the aligned CNT film in the parallel direction along the tensile axis was higher than that of a randomly oriented CNT film. In contrast, the strength in the perpendicular direction was very low. It was demonstrated that this trend is also well reflected in the theoretical predictions.

Wang et al.⁵ reported enhanced mechanical properties in chemically cross-linked CNT films upon the exposure of electron-beam irradiation onto the film. Although the CNTs had a random orientation in the film, the cross-linked CNT film showed increased strength and a higher modulus with an increase in the irradiation dose. Theoretical calculations were also made with the parameters under the experimental conditions and compared with the results. When the crosslinking density was less than 3%, the prediction was in good agreement with the experimental value, whereas a gap appeared with an increase in the crosslinking density. This deviation may have originated from the

difficulty in quantifying the crosslinking density. As the irradiation beam method was only applied onto the exposed surface area of the CNT films, the internal chemical nature could not easily be analyzed.

The parameters used in this case, i.e., the type of CNTs, the alignment and other numerical values, are shown in Table 2.2. The comparison of the theoretically calculated values and the experimental results proved that the equations to determine the strength of the CNT film efficiently reflect the fiber properties and structural parameters.

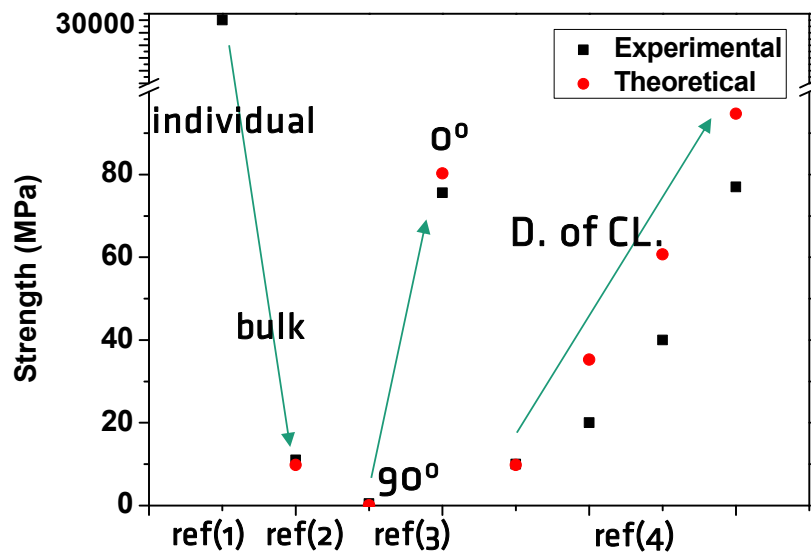


Fig. 2.3. Comparison of theoretically calculated values with previously reported experimental results.

Table 2.2. Previously reported CNT buckypapers

Ref	CNT (D, nm)	Alignment (φ_i)	Packing(ϕ)	Bonding (kJ/mol)	Density of CL.	$\sigma_{\text{experimental}}$ (MPa)
(1) <i>Phys. Rev. Lett.</i> 2000 , 84, 5552 / <i>Science</i> 2000 , 287, 637	SWNT MWNT					30000
(2) <i>J. Am. Chem. Soc.</i> 2005 , 127, 5125	SWNT (D=1)	randomly oriented	0.1	van der Waals	0	10
(3) <i>Carbon</i> 2011 , 49, 2437	MWNT (D=30)	Aligned	0.58	van der Waals	0	75.6 (0°) 0.5 (90°)
(4) <i>Adv. Mater.</i> 2007 , 19, 12	SWNT (D=1)	randomly oriented	0.1	C-C (sp ³)	3~10%	10(0%)~ 80(10%)

2.3 Effect of structural parameters on the strength of CNT films

From the developed equations, we can theoretically calculate and investigate the effects of structural parameters on the strength of CNT films. The introduced numerical values, with a number of assumptions, are indicated in the figure captions of Figs. 2.4-2.7. As the alignment of the CNTs along the tube axis changed from the parallel to the perpendicular direction, the strength of the CNT film was significantly decreased, as shown in Figure 2.4. When all of the CNTs were aligned along tube axis, the strength of the film was 15 GPa, whereas the strength in the $\pi/2$ case was less than 1 GPa. The strength of the CNT film was proportional to the packing density (Figure 2.5), showing a trend similar to that associated with the alignment. As the CNTs have loosely packed structure, the strength of the film was decreased. When the types of interaction forces between the CNTs were varied, the predicted strength rapidly changed, as shown in Figure 2.6. According to the interaction energies (C-C, C-N, coordination, hydrogen, and van der Waals), a considerable change was observed. Even when all of the CNTs has an aligned morphology with a high packing density, the CNT films depending only on the van der Waals interaction showed very low strength values. In this respect, the introduction of engineered crosslinking was one of the key issues in the preparation of high-strength CNT film. As shown in Figure 2.7, when amide bonding was formed between the CNTs, the strength was significantly increased with an increased density of the crosslinking as well.

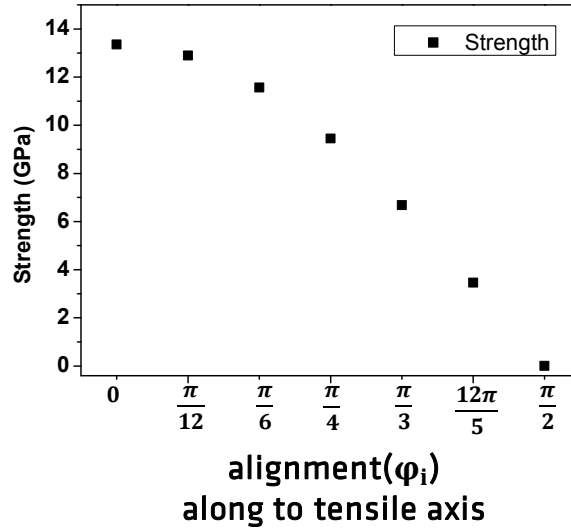


Fig. 2.4. Effect of CNT alignment on the strength of CNT films. [Conditions: $\sigma_{CNT} = 30$ GPa, $D = 1$, $d_{CL} = 1$, $a = 0.5$, $I_{CNT} = 309$ kJ/mol, and $\phi = 1$]

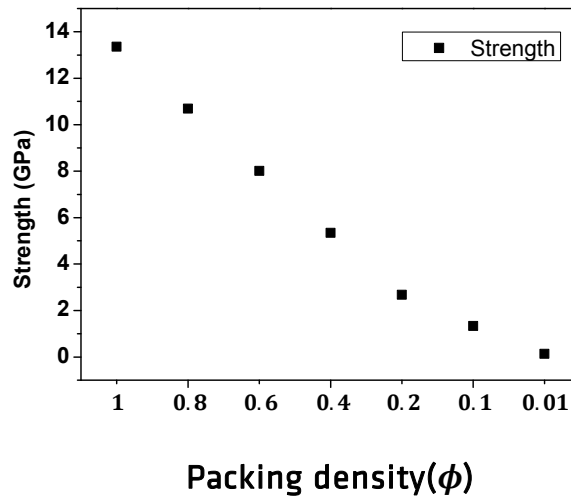


Fig. 2.5. Effect of CNT packing density on the strength of CNT films. [Conditions: $\sigma_{CNT} = 30$ GPa, $D = 1$, $d_{CL} = 1$, $a = 0.5$, $I_{CNT} = 309$ kJ/mol, and $\phi_i = 0^\circ$]

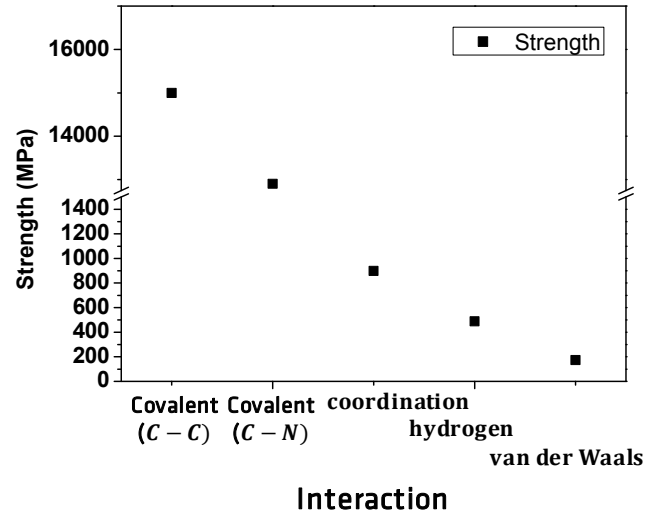


Fig. 2.6. Effect of the type of interaction between CNTs on the strength of CNT films.

[Conditions: $\sigma_{CNT} = 30$ GPa, $D = 1$, $d_{CL} = 1$, $a = 0.5$, $\phi = 1$, and $\varphi_i = 0^\circ$]

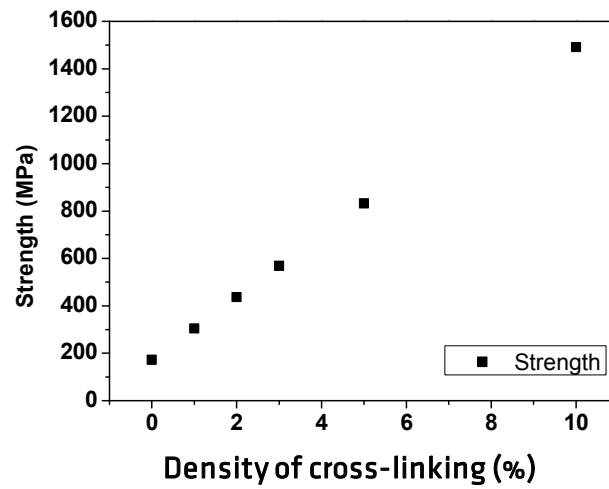


Fig. 2.7. Effect of the cross-linking density on the strength of CNT films. [Conditions:

$\sigma_{CNT} = 30$ GPa, $D = 1$, $a = 0.5$, $I_{CNT} = 309$ kJ/mol, $\phi = 1$, and $\varphi_i = 0^\circ$]

2.4 Conclusion

New equations regarding the strength and nanomechanics of CNT film were proposed in this study. The equations accounted for the parameters which influence the fiber properties and film structures. The reliability of the equations was confirmed by comparing the results from theoretical calculations with earlier experimental findings. From the theoretical considerations, we expect the newly developed equations to be applicable to the design and realization of high-strength CNT films with good control of various structural parameters.

2.5 References

1. Yu, M. F.; Files, B. S.; Arepalli, S.; Ruoff, R. S. Tensile Loading of Ropes of Single Wall Carbon Nanotubes and Their Mechanical Properties. *Phys. Rev. Lett.* **2000**, *84*, 5552-5555.
2. Yu, M. F.; Lourie, O.; Dyer, M. J.; Moloni, K.; Kelly, T. F.; Ruoff, R. S. Strength and Breaking Mechanism of Multiwalled Carbon Nanotubes under Tensile Load. *Science* **2000**, *287*, 637-640.
3. Dettlaff-Weglikowska, U.; Skakalova, V.; Graupner, R.; Jhang, S. H.; Kim, B. H.; Lee, H. J.; Ley, L.; Park, Y. W.; Berber, S.; Tomanek, D.; Roth, S. Effect of SOCl_2 Treatment on Electrical and Mechanical Properties of Single-Wall Carbon Nanotube Networks. *J. Am. Chem. Soc.* **2005**, *127*, 5125-5131.
4. Inoue, Y.; Suzuki, Y.; Minami, Y.; Muramatsu, J.; Shimamura, Y.; Suzuki, K.; Ghemes, A.; Okada, M.; Sakakibara, S.; Mimura, F.; Naito, K. Anisotropic Carbon Nanotube Papers Fabricated from Multiwalled Carbon Nanotube Webs. *Carbon* **2011**, *49*, 2437-2443.
5. Wang, S. R.; Liang, Z. Y.; Wang, B.; Zhang, C. High-Strength and Multifunctional Macroscopic Fabric of Single-Walled Carbon Nanotubes. *Adv. Mater.* **2007**, *19*, 1257-1261.

Chapter 3 Preparation and Mechanical Performance of Self-Assembled, Aligned CNT Film with High Packing Density

3.1 Introduction

CNTs have attracted remarkable attention due to their unique mechanical, electrical, and thermal properties.¹ The outstanding mechanical performance of individual CNTs suggests that they are promising for use as building blocks in novel structural materials.² However, research on preparing buckypaper, in which CNTs are assembled into a web or sheet, has not yet yielded the expected high-performance mechanical properties of the materials. The random orientations and low CNT density were considered the most significant contributors to the low mechanical performances of the buckypaper. Much effort has been taken to align CNTs so that the buckypaper has a well-ordered nanostructure with high packing density. For example, the in situ CNT alignment on a template during CVD processes has been extensively studied,³ although this approach has some issues like high implementation costs. A variety of scalable approaches have recently been reported to prepare aligned CNTs by applying external forces,⁴⁻⁹ mechanical shearing forces,¹⁰⁻¹² liquid crystals embedding,¹³⁻¹⁵ patterned substrates,¹⁶ and dip-coating methods.¹⁷

Even from those approaches, the mechanical performance of the obtained buckypaper was disappointing due to poor alignment and low packing density of CNTs. The CNT

self-assembly in a liquid crystalline phase has been suggested to achieve good alignment and high-density CNTs in a buckypaper.¹⁸⁻²⁵ This method exposed practical drawbacks since the fabrication process for a buckypaper from a highly concentrated CNT suspension is highly complicated. A facile, but effective, method for fabricating CNT buckypaper with a well-aligned state and a high packing density remains in high demand.

In this chapter, we discuss a facile filtration method to fabricate a buckypaper composed of densely packed and well-aligned CNTs. Early reports have described a filtration method that yielded a buckypaper with randomly oriented CNTs. By contrast, our suggested method relies on the entropy-driven alignment of CNTs to form an anisotropic phase triggered by a simple filtration process of a CNT suspension. The resulting aligned CNT layers self-assemble horizontally on the filtration membrane. The self-aligned densely packed CNT nanostructures apparently formed only from a CNT suspension concentration of 1 mg/mL. These results confirmed that the critical suspension concentration should be high, which can facilitate interaction among CNTs, thereby promoting self-assembled ordering. Furthermore, our systematic investigation found that dispersion status also played a crucial role in triggering the self-alignment behavior. The resultant aligned buckypaper displayed an enhanced packing density, strength, modulus, and hardness compared to previously reported buckypapers. This unprecedented study will provide a facile and scalable preparation method for aligned CNT papers with high packing density and new insight into CNT self-assembly behaviors.

3.2 Results and discussion

A schematic illustration about the formation of aligned CNT layers is proposed in Figure 3.1. The prepared suspension containing isotropic CNTs was filtered, and the CNTs were deposited on the filtration membrane. When the suspension passed through the filter paper, the CNTs immediately began to accumulate on the membrane surface under the hydrodynamic drag. As the solvent was removed by filtration, the local concentration of CNTs near the membrane increased rapidly, and the CNT–CNT interactions appeared dominant over the CNT–solvent interactions. The CNTs were most likely to behave like lyotropic rigid rod-like polymers in the concentrated regime as predicted by Onsager model²⁶ and undergo entropy-driven alignment above a critical concentration to form an ordered deposit with an aligned arrangement, leading to densely packed CNT domain formation. Onsager's theory has been widely used to describe the phase behavior of rigid rod-like entities, such as rod-like liquid crystalline polymers, biological rod particles, and inorganic nanorods. We presumed that CNTs can be classified as rigid rod-like linear polymers due to their unusual high aspect ratio and straightness, which is consistent with previous reports.^{19, 20, 27-29} From a thermodynamic point of view, at a fixed density, the isotropic to nematic transition arises from the competition between the orientational entropy and the packing entropy. Above a critical concentration, the packing entropy becomes dominant over the orientational entropy due to Onsager's excluded volume effect, which the nematic phase is favored. From an experimental point of view, the attractive forces (van der Waals) and short range repulsive forces (electrostatic) between CNTs are counterbalanced in the concentrated CNT suspension. When CNTs are dispersed in a good solvent, the repulsive forces surpass attraction forces between nanotubes, which enable them to form thermodynamically stable nematic phase in the concentrated regime as with Onsager's theory. As CNT filtration processes proceeded,

initial deposits act as pre-deposited aligned CNT layers. The subsequent CNTs in the suspension gradually became aligned along the pre-deposited horizontally aligned CNT layer. This process resulted in the aligned domain growth. A detailed experimental procedure can be found in the Experimental section



Fig. 3.1. Mechanism for self-alignment behavior of CNTs with subsequent filtration process.

To understand the self-alignment mechanism dependent on the variable CNT suspension concentrations, the natural drying system was also introduced. When a droplet of colloidal suspension is dried on a solid surface, the solvent evaporates and induces an outward capillary flow carrying the suspended particles. This well-known phenomenon, called the “coffee ring effect,” redistributes the particles into two different concentrations according to droplet location (edge: concentric regime, center: diluted regime).^{30, 31} To confirm the effect of CNT suspension concentration change on alignment phenomenon, a droplet was placed and dried on a glass substrate. The SWNT suspension utilized in this step was the same as the SWNT suspension for the aligned buckypaper via filtration. Figure 3.2 showed the birefringence texture along the perimeter attributed to the SWNT orientations after complete drying. Furthermore, well-aligned SWNTs were obtained from the concentric edge region while the non-aligned SWNTs were obtained from the relatively diluted center region. Based on “coffee ring effect” where the solute concentration gradient is created during evaporation, the self-alignment phenomenon is assumed to be triggered by the increase in local concentration.

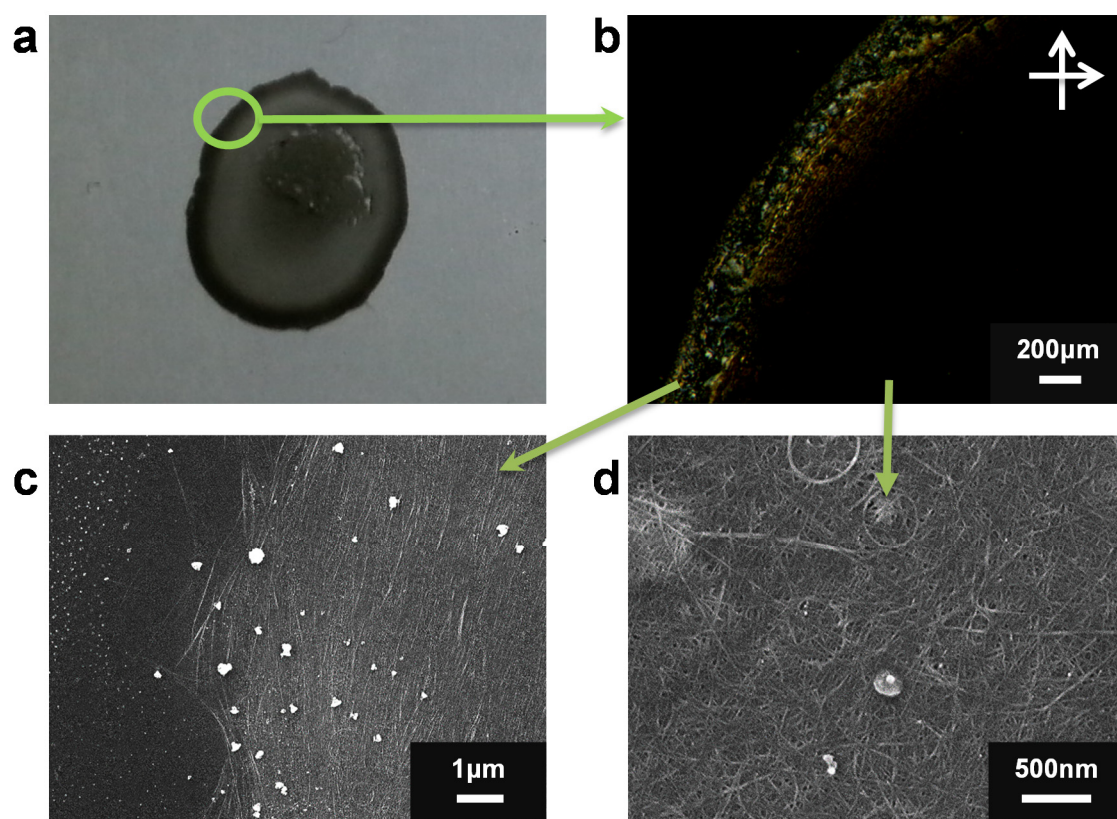


Fig. 3.2. (a) Photograph of residue ring stain after drying SWNT suspension droplet on a glass substrate, (b) POM image of perimeter, (c) aligned SWNTs in the edge regime, (d) non-aligned SWNTs in the center regime.

For the first time, we experimentally observed the pre-deposited, aligned CNT layer functions as an alignment template layer and play an important role in triggering subsequent self-alignment. CNTs have functioned as distinct nucleating agents for polymer crystallization and templates for liquid crystal molecule orientation due to the nanoscale diameter, high specific surface area and extremely high aspect ratio.^{9, 32-34} In our experiments, subsequent CNTs tended to align themselves on the pre-deposited aligned CNT layer; facilitating the formation of large-scale ordered domains. The sequence of polarized optical microscopy (POM) buckypaper images shown in Figure 3.3a indicates alignment behavior triggered by single-walled carbon nanotube (SWNT) suspension filtration over the course of filtering a 1 mg/mL suspension. As the quantity of SWNTs deposited on the membrane reached 2.5 mg/cm², very weak birefringence started to be observed and indicated that the isotropic SWNTs underwent alignment to eventually deposit themselves in an aligned arrangement. The number of small, dark, yellow spots in the 5.0 mg/cm² SWNT buckypaper that originated from the anisotropic properties of the aligned SWNT domains clearly increased. The 10 mg/cm² SWNT buckypaper provided POM image that exhibited strong birefringence of multifarious spots indicative of SWNT connected domains aligned over a large scale. Comparing POM images revealed remarkable changes in the birefringence properties as the filtration of the SWNT suspension proceeded. The differences were clearly attributable to the individual SWNT orientation, as shown in Figure 3.4. As the deposited SWNT quantities increased, the deposited SWNT buckypaper had better aligned orientation and more densely packed morphologies. The aligned domains became larger since the pre-deposited aligned CNT layers facilitated not only orientation, but also heterogeneous nucleation and the subsequent CNT growth during filtration due to decreased activation energy in the crystalline phase (ordered and aligned phase). This observation confirmed

that subsequent deposition of isotropic SWNTs on a pre-deposited aligned layer led to the formation of large aligned macroscale domains of SWNTs. The thicknesses of 2.5, 5, 7.5, 10.0 mg/cm² SWNT buckypaper were 6.0, 13.4, 19.6, 24.4 μm, respectively. In our system, the aligned buckypapers were obtained when the buckypaper thickness exceeds 19.6 μm.

The concentration of SWNT suspension was important for the self-assembled alignment process. At low concentrations, the particle–particle interactions were not sufficiently strong enough to induce the alignment behavior. POM buckypaper images prepared from a 0.01 mg/mL SWNT suspension displayed no birefringence properties, which indicate that the SWNTs deposited with an isotropic arrangement (Figure 3.3b). The filtration method applied to low concentration SWNT suspensions did not yield aligned films, even though the overall process used the same total quantity of SWNTs as the process applied to a high concentration SWNT suspension. These results can be explained by the phase behavior of CNTs, which is assumed to be analogous to that of lyotropic rigid rod-like polymers.

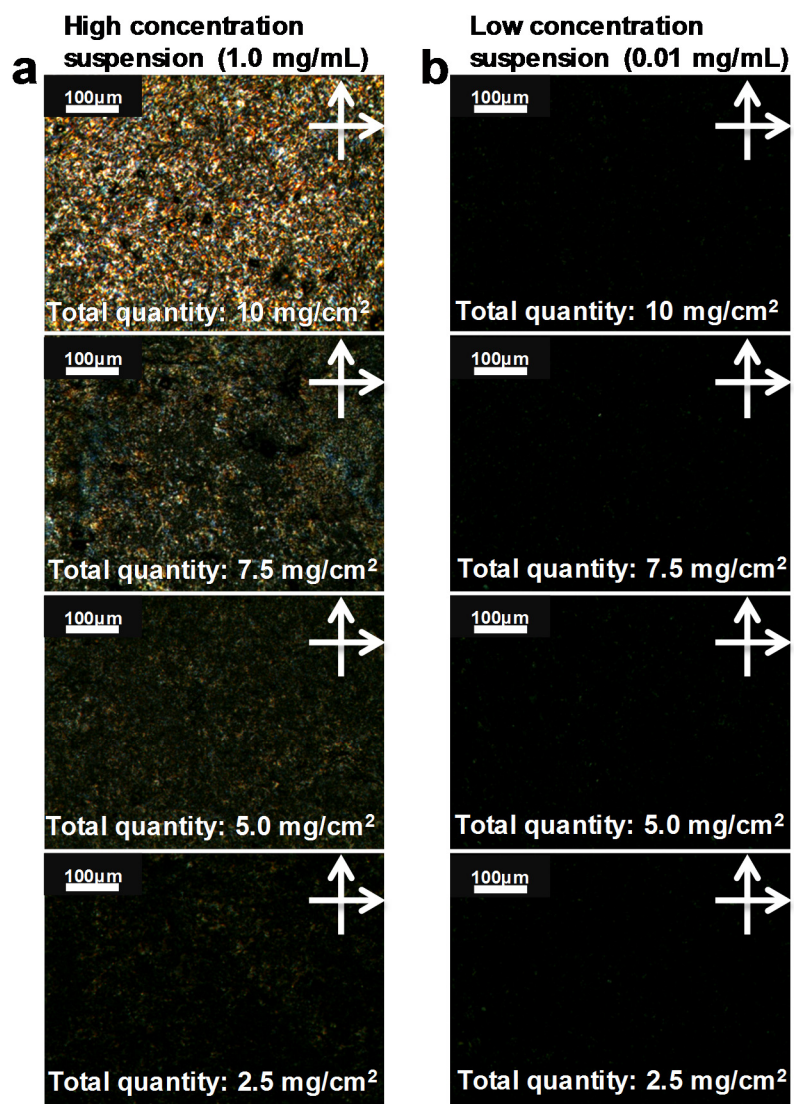


Fig. 3.3. POM image sequence of SWNT buckypaper prepared from (a) high concentration suspension and (b) low concentration suspension.

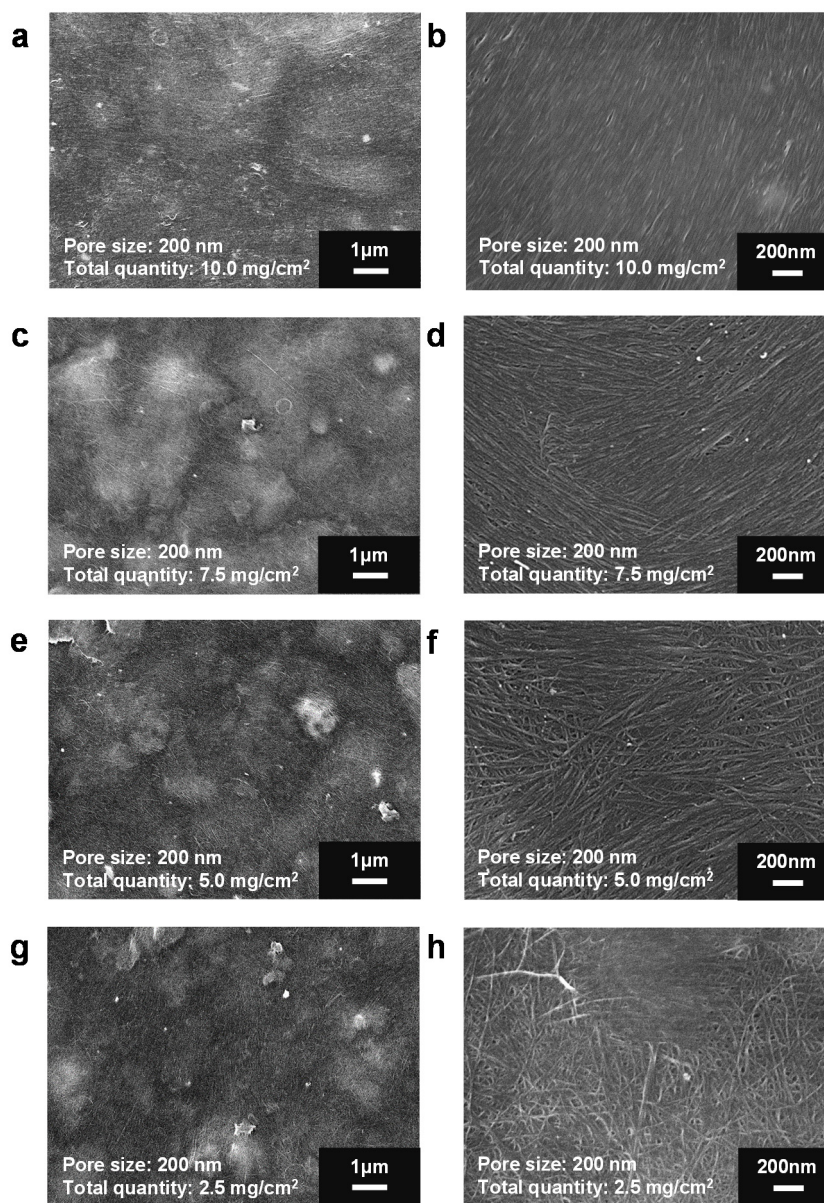


Fig. 3.4. SEM images of the surface of SWNT buckypapers prepared on the PTFE membrane with pore size of 200 nm (filtration velocity: 3.8 mL/h). The deposited SWNT quantities on the membrane: (a-b) 10.0 mg/cm², (c-d) 7.5 mg/cm², (e-f) 5.0 mg/cm², (g-h) 2.5 mg/cm².

Figure 3.5 shows the SWNT phase diagram with an aspect ratio of 1000 as predicted according to previous reports.^{35, 36} Increasing the suspension concentration of isotropic SWNTs results in a transition from an isotropic to a nematic phase at 0.1 vol% through a biphasic region. In our system, a solvent removal by filtration can concentrate SWNTs followed by crossing the phase line from left to right. However, not all initial suspensions can be concentrated to reach where the nematic phase is in equilibrium. We systematically explored the concentrations in an effort to identify the critical suspension concentration to achieve self-alignment. This concentration was found to fall in the ranges 0.5–1.0 mg/mL, determined by the quantized birefringence intensities of the SWNT buckypaper POM images (Figure 3.6).

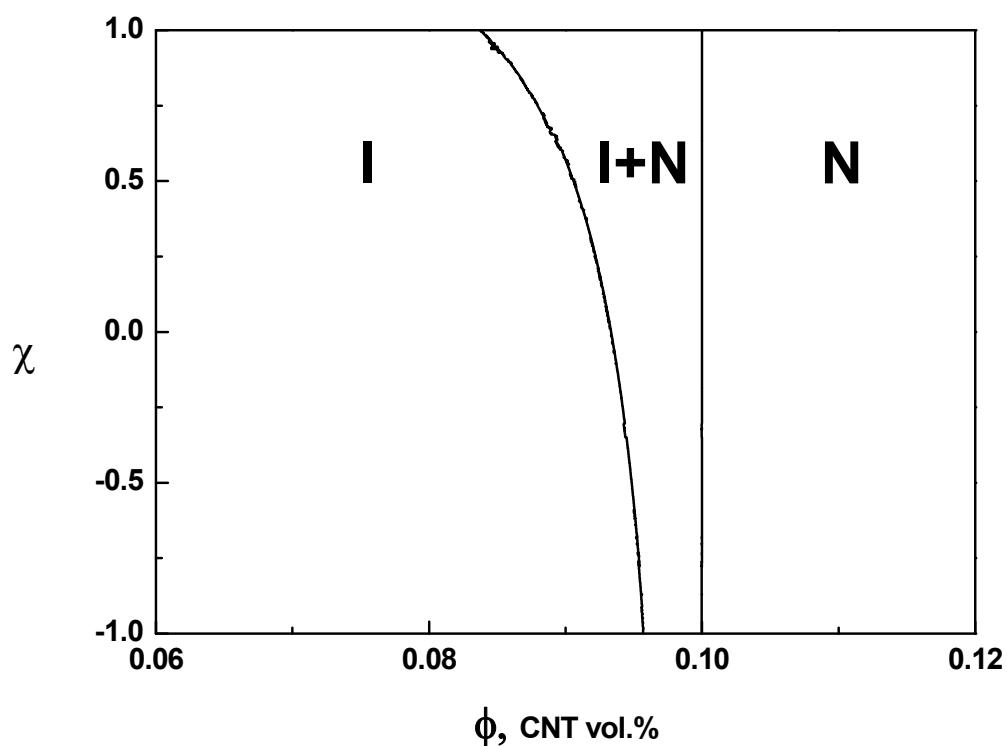


Fig. 3.5. Phase diagram of CNTs ($D=1$, $L=1000$) in N-methyl-2-pyrrolidone (NMP). The Flory-Huggins interaction parameter, χ , is plotted against CNT volume fraction. I and N indicate isotropic and nematic phase of CNTs, respectively. The two lines denote the boundary of the dispersion state transition. The region between the lines corresponds to the biphasic region (I+N).

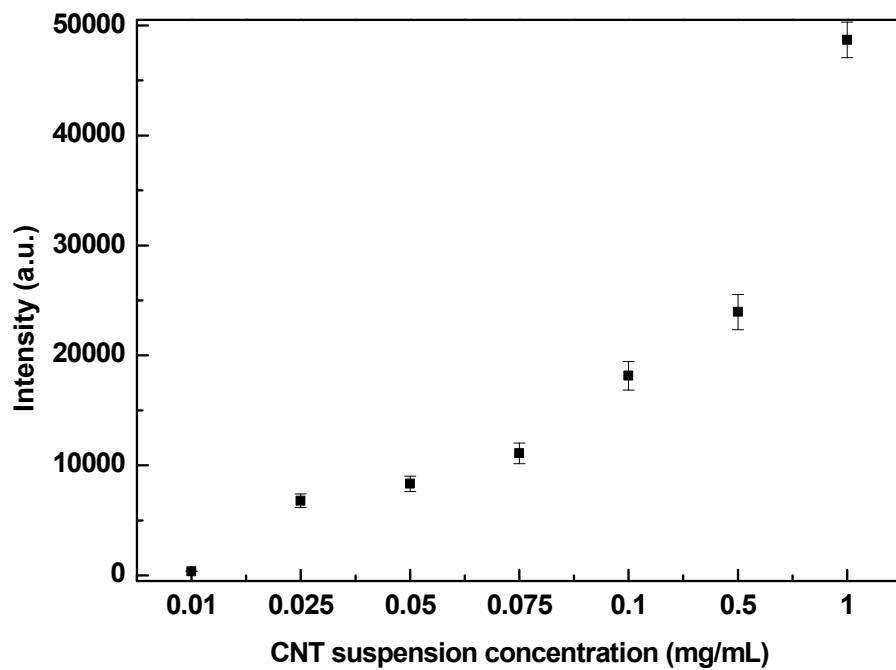


Fig. 3.6. The birefringence intensity of POM images of SWNT buckypapers prepared under various suspension concentrations.

It is worth noting that filtration velocity also influenced the SWNT alignment process. Figure 3.7 displays the size distributions of aligned SWNT domains in buckypapers prepared under two different filtration velocities. In the fast filtration condition, the subsequent CNTs did not have enough time for diffusion onto the pre-deposited aligned CNT layers and sufficient thermodynamic interaction, which resulted in limited growth and alignment behavior. Consequently, the resultant buckypapers (Figure 3.8) showed less aligned and loosely packed morphologies compared to the papers (Figure 3.4) from slow filtration. The average aligned domain size of SWNT buckypapers from fast filtration was relatively smaller than that of SWNT buckypapers from slow filtration. To make a highly aligned CNT paper via a filtration method, we should consider not only CNT suspension concentration and filtration velocity but also dispersion state in a suspension. This is because CNT agglomeration is undesirable for obtaining a high volume concentration of CNT in a specific mass concentration. CNTs can be dispersed in a specific solvent either covalently or noncovalently modifying the CNTs to overcome the inherent bundling or entangling CNT properties.³⁷⁻⁴¹

The CNTs used in this work were functionalized by acid oxidation (covalent) or surfactant wrapping (noncovalent). X-ray photoelectron spectroscopy (XPS), Raman spectroscopy, atomic force microscopy (AFM), and UV-vis spectroscopy were used to characterize the surfaces and physical properties of the SWNTs and evaluate the degree of dispersion of the suspensions (see Figures 3.9–3.12). The XPS C1s spectra of the pristine and acid-oxidized SWNTs are shown Figures 3.9a and b. After acid treatment, the quantity of oxygen-containing functional groups (hydroxyl, epoxy, carbonyl, and carboxyl) on the SWNTs surfaces increased. Raman spectra of the pristine and acid-oxidized SWNTs are shown in Figure 3.9d. The relative intensity ratio (I_D/I_G) of the pristine SWNTs was 0.04; however, after acid treatment, I_D/I_G increased to 0.17. This

increase indicated a change in the surfaces of the SWNTs, in accordance with the XPS results. Quantitative information about the distributions of the lengths of the acid-oxidized SWNTs was derived directly from the AFM images. The acid-oxidized SWNT suspension was spin-coated onto freshly cleaved mica. The average length of the SWNTs was measured to be $1.03 \pm 0.47 \mu\text{m}$. The degree of dispersion of the acid-oxidized SWNTs in various solvents was estimated based on the UV–Vis absorption spectra shown in Figure 3.12. The absorbance properties varied significantly according to the solvent type. The degree of dispersion improved significantly as the SWNTs were dispersed in amide solvents such as N-methyl-2-pyrrolidone or dimethylformamide. The influence of the dispersion status on the self-alignment behavior was investigated by preparing buckypaper using a poorly dispersed SWNT suspension in the filtration process. Figure 3.13 shows the randomly oriented SWNTs on the buckypaper prepared by a pristine (poorly dispersed) SWNT suspension. Unless the SWNTs were functionalized and effectively dispersed in the solvent, self-aligned CNTs buckypaper cannot be obtained using the filtration method.

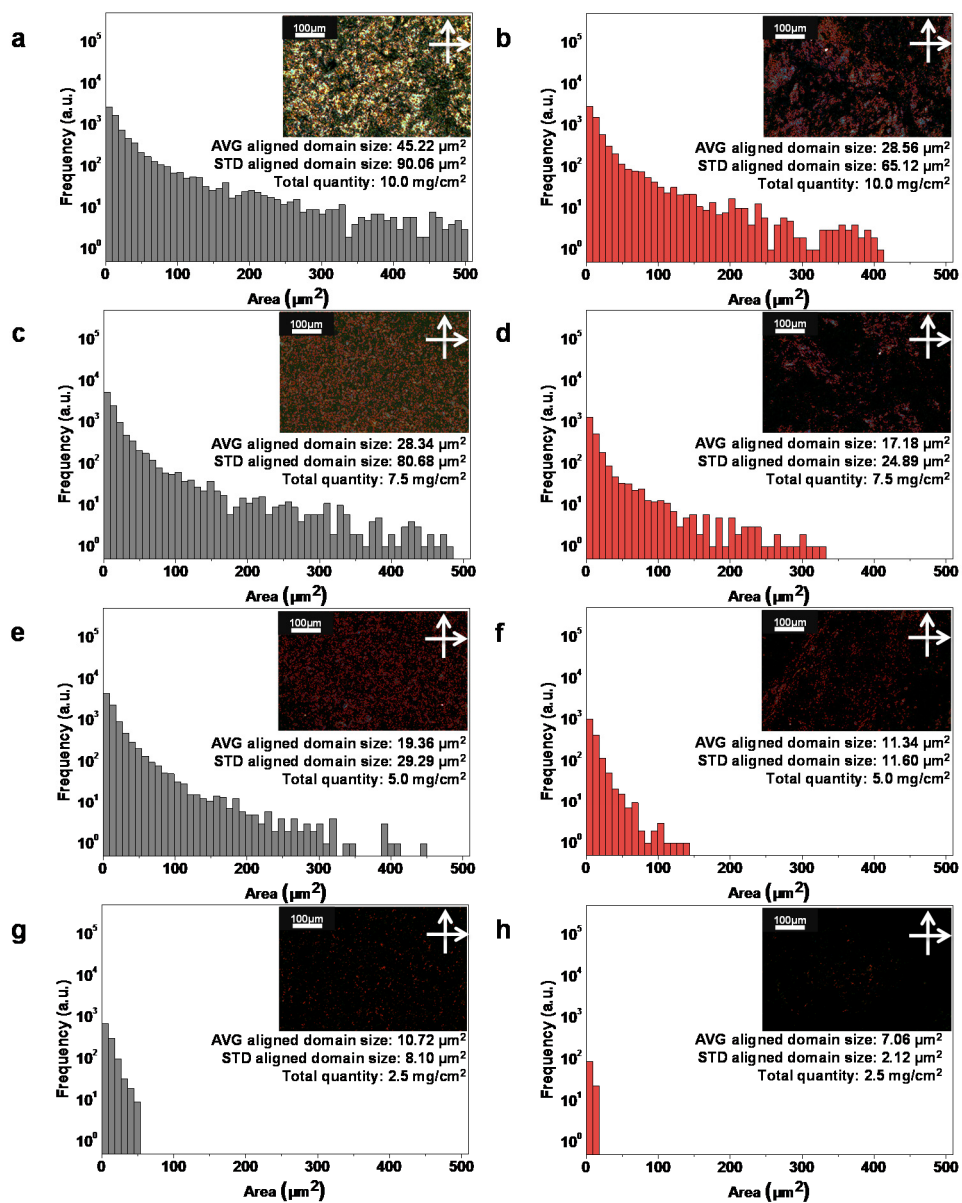


Fig. 3.7. Comparison of size distributions of aligned SWNT domains showing birefringence texture, including representative POM images of buckypapers prepared on the PTFE membrane with pore size of 200 nm (a, c, e, g: slow filtration, 3.8 mL/h), and 500 nm (b, d, f, h: fast filtration, 6.3 mL/h).

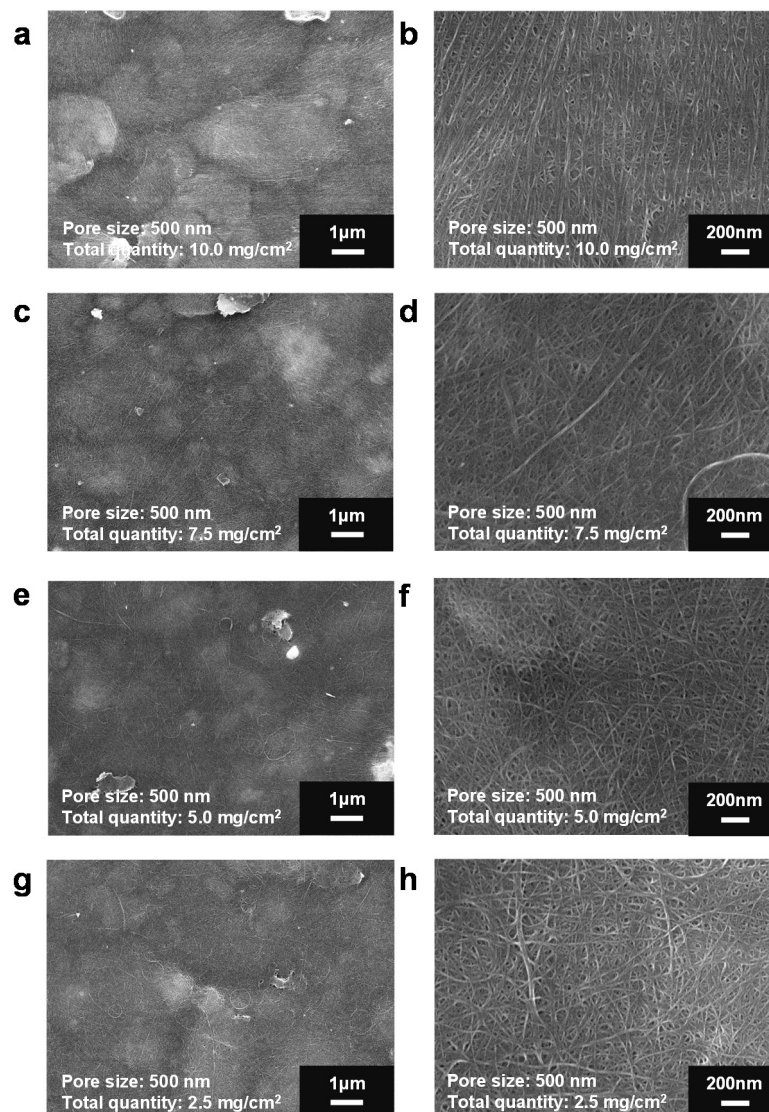


Fig. 3.8. SEM images of the surface of SWNT buckypapers prepared on the PTFE membrane with pore size of 500 nm (filtration velocity: 6.3 mL/h). The deposited SWNT quantities on the membrane: (a-b) 10.0 mg/cm², (c-d) 7.5 mg/cm², (e-f) 5.0 mg/cm², (g-h) 2.5 mg/cm².

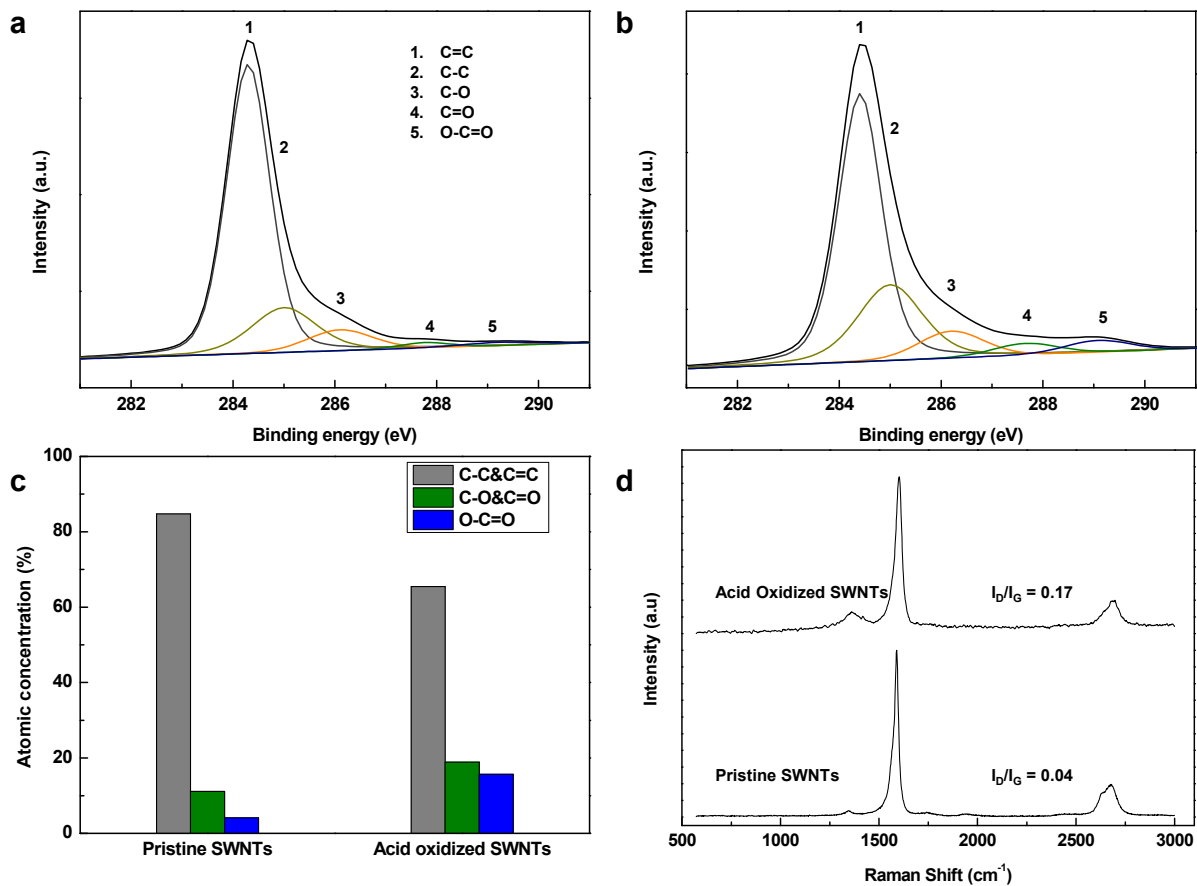


Fig. 3.9. XPS C1s spectra of (a) pristine SWNTs and (b) acid oxidized SWNTs. (c) Quantitative analysis of various forms of C in the SWNTs, determined by integrating the C1s spectra peak area corresponding to the C-C & C=C, C-O & C=O, O-C=O bonded carbon. (d) Raman Spectra of SWNTs.

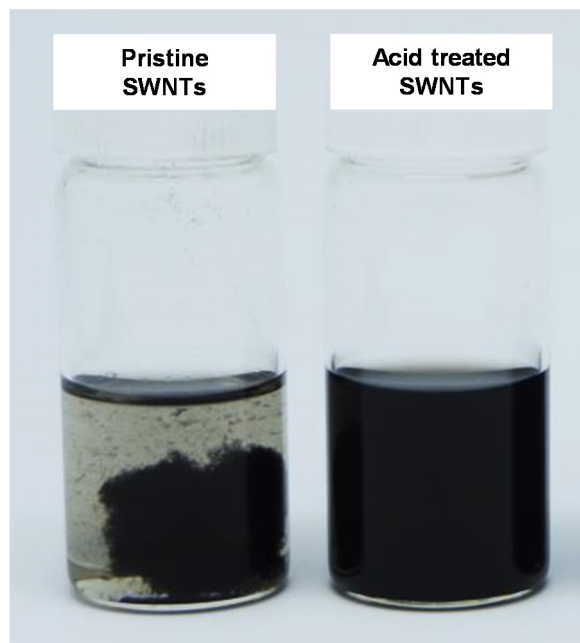


Fig. 3.10. Photograph of SWNT suspensions in NMP (suspension concentration: 1 mg/mL)

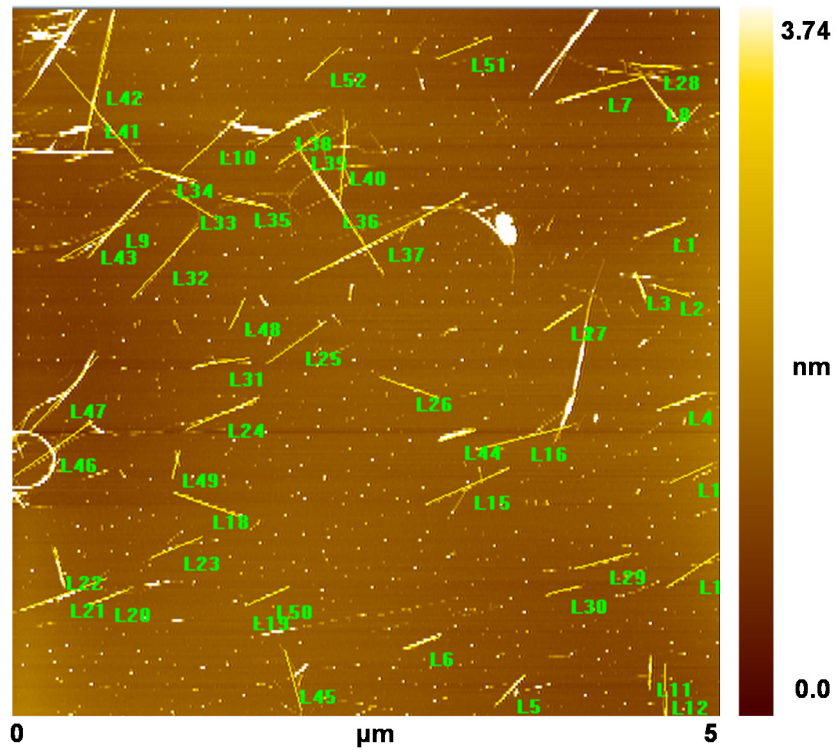


Fig. 3.11. Tapping-mode AFM image of acid oxidized SWNTs on a mica surface.

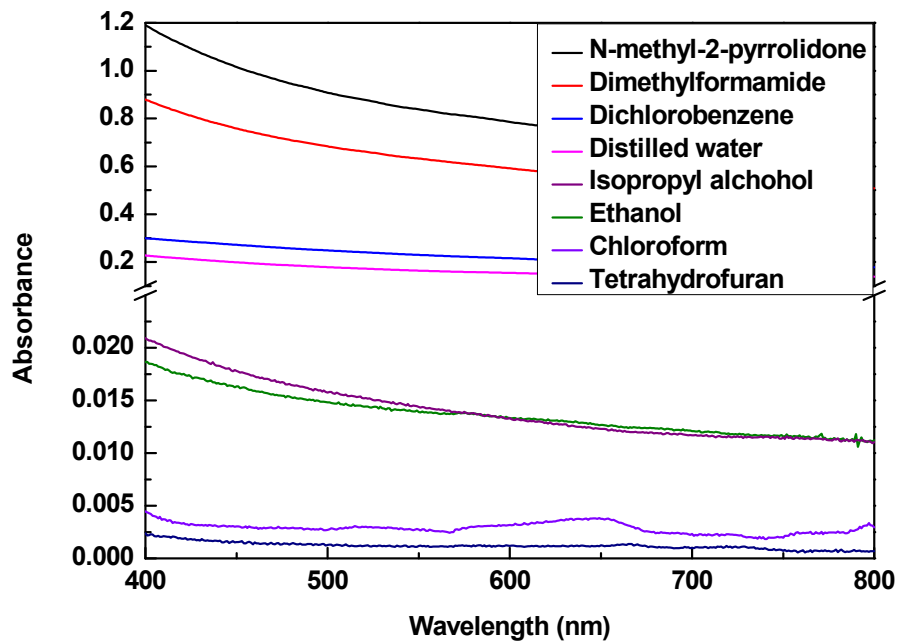


Fig. 3.12. UV-vis spectra of acid treated SWNT suspensions in various solvents.

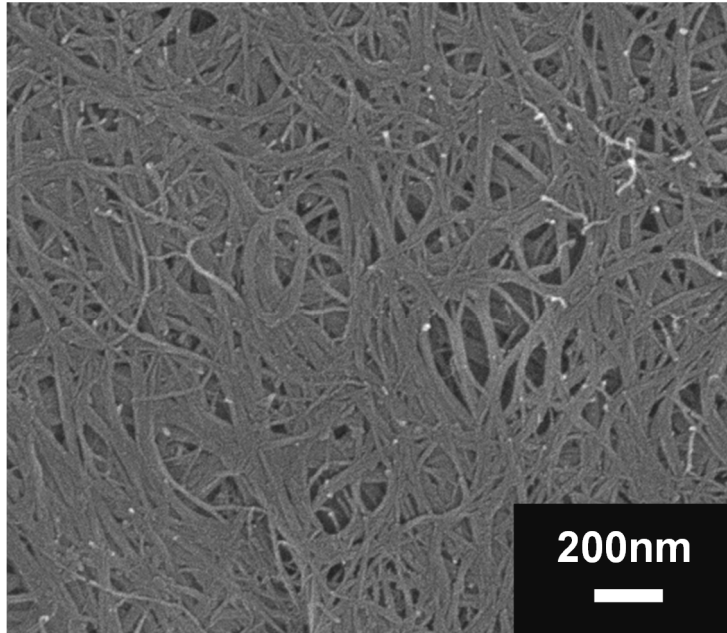


Fig. 3.13. SEM image of the surface of buckypaper prepared by pristine SWNT suspension.

Figure 3.14 displays scanning electron microscopy (SEM) images that show the CNTs arrangements. Figures 3.14a and 3.14b show the typical isotropic morphologies of the pristine and acid-oxidized SWNTs, respectively. Figure 3.14c shows an image of self-assembled aligned SWNT buckypaper prepared using simple filtration of the acid oxidized SWNT-NMP suspension. The well-aligned SWNTs assumed a closely packed nanostructure. To investigate if the alignment behavior is dependent on the surface properties of the filtration membrane, the filtration process was conducted using two different membranes and compared. The SWNT buckypapers prepared on an anodic aluminum oxide (AAO) membrane (Figure 3.14d) or a polytetrafluoroethylene (PTFE) membrane (Figure 3.14c) displayed similar aligned morphologies, indicating that the filtration membrane did not influence the alignment properties. The surfactant wrapped SWNT-water (Figure 3.14e) and the acid oxidized multi-walled carbon nanotubes (MWNTs)-NMP (Figure 3.14f) suspension also formed aligned morphologies. The proposed filtration method appears to readily extend to CNT alignment, irrespective of the CNT type and surface modification method.

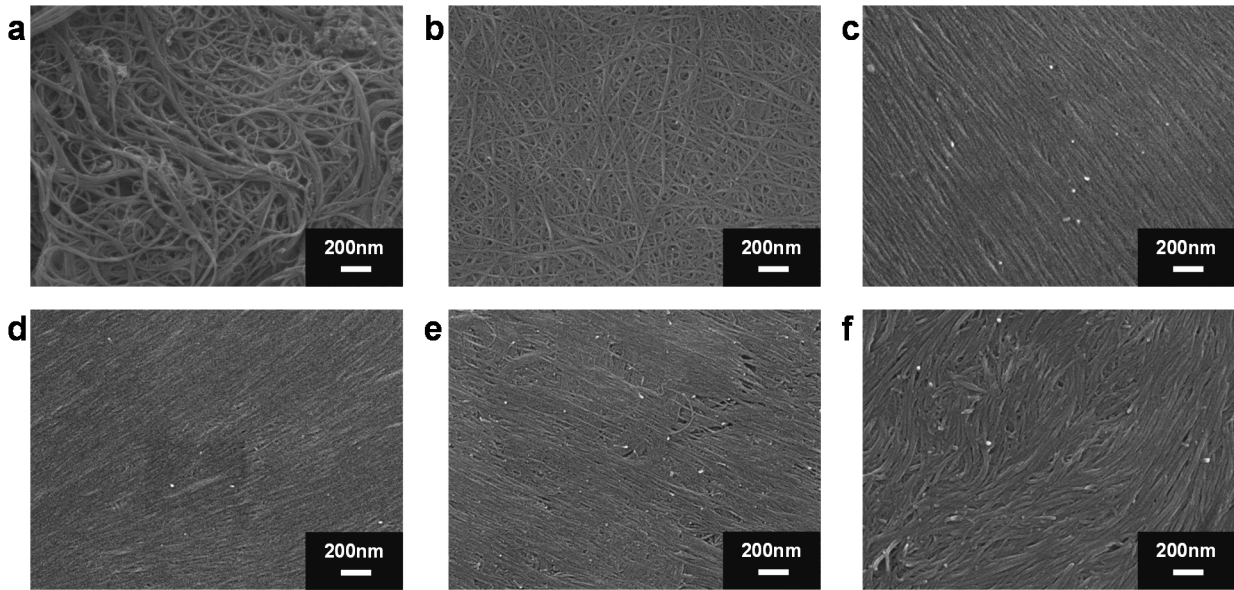


Fig. 3.14. SEM images: (a) pristine SWNTs, (b) acid oxidized SWNTs just after acid oxidation, deionized water purification, and drying process, (c) aligned, acid oxidized SWNTs on PTFE, (d) aligned, acid oxidized SWNTs on AAO, (e) aligned, surfactant wrapped SWNTs and (f) aligned, acid oxidized MWNTs. The total deposited CNT quantity and suspension concentration to prepare the aligned buckypapers (c, d, e, and f) were 10.0 mg/cm^2 , and 1.0 mg/mL , respectively.

The porosity of buckypaper based on CNTs can often provide unfavorable weak points with respect to the mechanical strength. The close-packed nanostructure formed by well-aligned SWNTs can mitigate pore evolution. The pore characteristics of the prepared SWNTs were quantitatively characterized by measuring the nitrogen sorption isotherms, as shown in Figure 3.15. The nitrogen isotherms of the products displayed feature characteristic of type IV isotherms, suggesting the presence of mesoporosity. The SEM results (see the Figure 3.15 insets) confirmed that the overall porosity decreased significantly as the density of the buckypaper increased. It is particularly noteworthy that the hysteresis pressure range varied according to the morphology, which indicates differences in the pore size distribution (Figure 3.16). As the density of the buckypaper increased, the large-sized mesopores were reorganized into small-sized mesopores concurrently with a significantly reduced pore volume. The mechanism underlying the porosity development in the CNT array suggested that a decrease in the pore size and volume signified a decrease in the distance between individual CNTs and a substantial enhancement in the packing density.

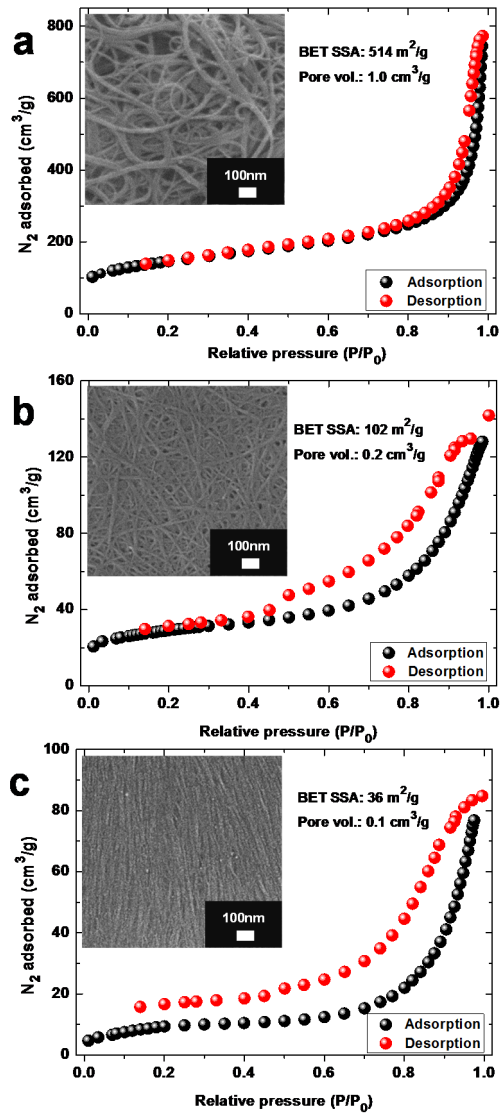


Fig. 3.15. N₂ adsorption isotherms (at 77K): (a) pristine SWNTs, (b) acid oxidized SWNTs and (c) aligned SWNTs.

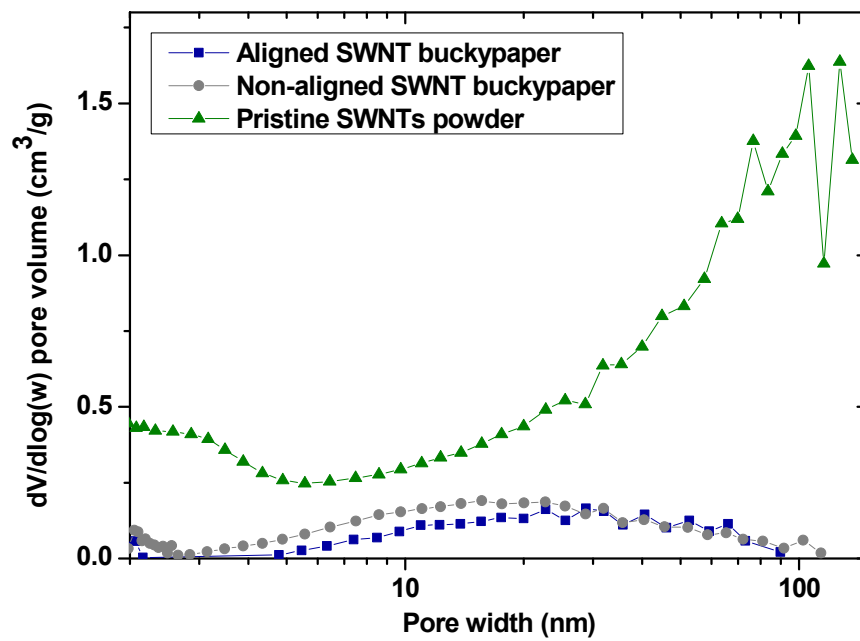


Fig. 3.16. Pore size distribution of the pristine SWNTs powder, aligned and non-aligned SWNT buckypaper.

The aligned morphology on the mechanical properties of the macroscopic materials was studied using a tensile test, as shown in Figures 3.17a and 3.17b. Before the tensile test, the papers were cut into the sizes (length: 32 mm, width: 6 mm) shown in Figure 3.18. Figure 3.17a shows representative stress–strain curves of SWNT buckypapers prepared under various suspension concentrations. The tensile strength and modulus were measured to be 12.38 ± 3.83 MPa and 3.11 ± 0.43 GPa, respectively, for the non-aligned SWNT buckypaper (0.01 mg/mL). On the other hand, the aligned SWNT buckypaper (1.0 mg/mL) exhibited a tensile strength of 94.62 ± 10.52 MPa and a modulus of 8.35 ± 2.75 GPa. This confirms the improved mechanical properties that resulted from the desired alignment. As the suspension concentration for preparing SWNT buckypaper increased, the resulting materials showed a steady increase in the mechanical properties due to the enhanced packing density. The numerical values for tensile strength, modulus and elongation of SWNT buckypapers prepared under various suspension concentrations are shown in Table 3.1. The strength and modulus of our buckypapers are comparable to the capillary aggregated CNT forests⁴² but relatively smaller than aligned CNT fibers due to the difference in the length of individual CNT and alignment along tensile axis.⁴³⁻⁴⁶ According to previous research on the tensile properties of aligned CNT materials, the materials are expected to show anisotropic properties. However, because the orientation of aligned SWNT domains in the buckypaper is multidirectional, the tensile properties of buckypapers appeared to be similar, irrespective of direction (Figure 3.19). In Figure 3.17b, the mechanical properties of the aligned SWNT buckypapers (1.0 mg/mL) prepared in this work were compared with those of other CNT-based buckypapers.⁴⁷⁻⁵⁶ Our aligned SWNT buckypapers showed superior strength and modulus values, which may have been attributed to the high degree of alignment. The thickness of our buckypaper for tensile

test was larger than one⁵⁶ (1.8 μm), similar with three^{48, 49, 53} (19.7~ 40 μm) and smaller than four^{50, 52, 54, 55} (80 ~ 270 μm). The aligned morphology of the SWNTs mainly enhanced the mechanical properties in two ways. As mentioned previously, the high degree of alignment and the consequent dense packing minimized the porosity or the formation of void defects in the macroscopic materials. The maximal contact area and attractive forces between adjacent SWNTs could be achieved by reducing the distance between SWNTs. The aligned morphology of SWNTs increased van der Waals forces between the nanotubes that are important in determining the nanostructure of bundles.^{57, 58} Thus, the close-packed nanostructure of the aligned SWNTs strengthened the resulting buckypapers due to effective load bearing between the SWNTs, facilitated by substantially increased van der Waals forces.

In addition to the tensile test, nanoindentation measurements were carried out using a Berkovich diamond nanoindenter tip to estimate the compressive elastic modulus and the hardness of the aligned SWNT buckypaper, as shown in Figures 3.17c and 3.17d. Materials with a large hardness value strongly resist plastic deformations and crack generation during compression tests. Under an applied force of 100 μN , the aligned SWNTs yielded a smaller penetration depth than was measured from the non-aligned SWNTs, indicating a greater hardness and stiffness in the aligned SWNTs (Figure 3.17c). Indeed, the elastic modulus and hardness values of the aligned SWNTs (1.0 mg/mL) were found to be 4.38 ± 0.36 GPa and 410.28 ± 40.85 MPa, respectively, as determined using the Oliver–Pharr method.⁵⁹ These values were much higher than those obtained from other SWNT buckypapers. While the tensile strength of SWNT buckypapers steadily increased with an increase in the suspension concentrations, the hardness values significantly increased in the range 0.1–1.0 mg/mL (see Table 3.1 for details). Since nanoindentation measured the top surface of buckypapers, the sudden increase might be

ascribed to the remarkable changes in degree of alignment of SWNTs in the upper portion of the buckypaper as the deposited SWNT quantity increased (Figure 3.3a and 3.6). The indent shape and crack generation were investigated by applying a stronger force of 1 mN. The changed sample surfaces using the same indenter tip were shown in the Figure 3.17 inset. Fracture and crack propagation occurred on the non-aligned SWNT surfaces (right, 0.01 mg/mL), whereas clear indent impressions without crack generation were observed on the aligned SWNT surfaces (left, 1.0 mg/mL). The differences in the two materials were mainly attributed to differences in the load transfer efficiency. The applied force was uniformly distributed into neighboring SWNTs on the aligned SWNT buckypapers due to the high degree of alignment and high packing density. Recent research on VACNTs synthesized using carbide-derived carbon (CDC) showed similar outcomes as our results.^{58, 60} The CDC-VACNTs exhibited a highly aligned structure with dense networking. The nanostructure enabled stronger interactions between adjacent CNTs in an array and effective energy dissipation. This consequently led to much higher compressive properties when compared to common VACNTs synthesized by CVD in the same manner as aforementioned. The compressive properties of the aligned SWNT buckypapers prepared with a closely packed nanostructure were superior to the corresponding properties of non-aligned SWNT buckypapers, CVD-VACNTs⁶¹, and cross-linked CNTs (CLCNTs)⁶² with low packing density (see Figure 3.17d).

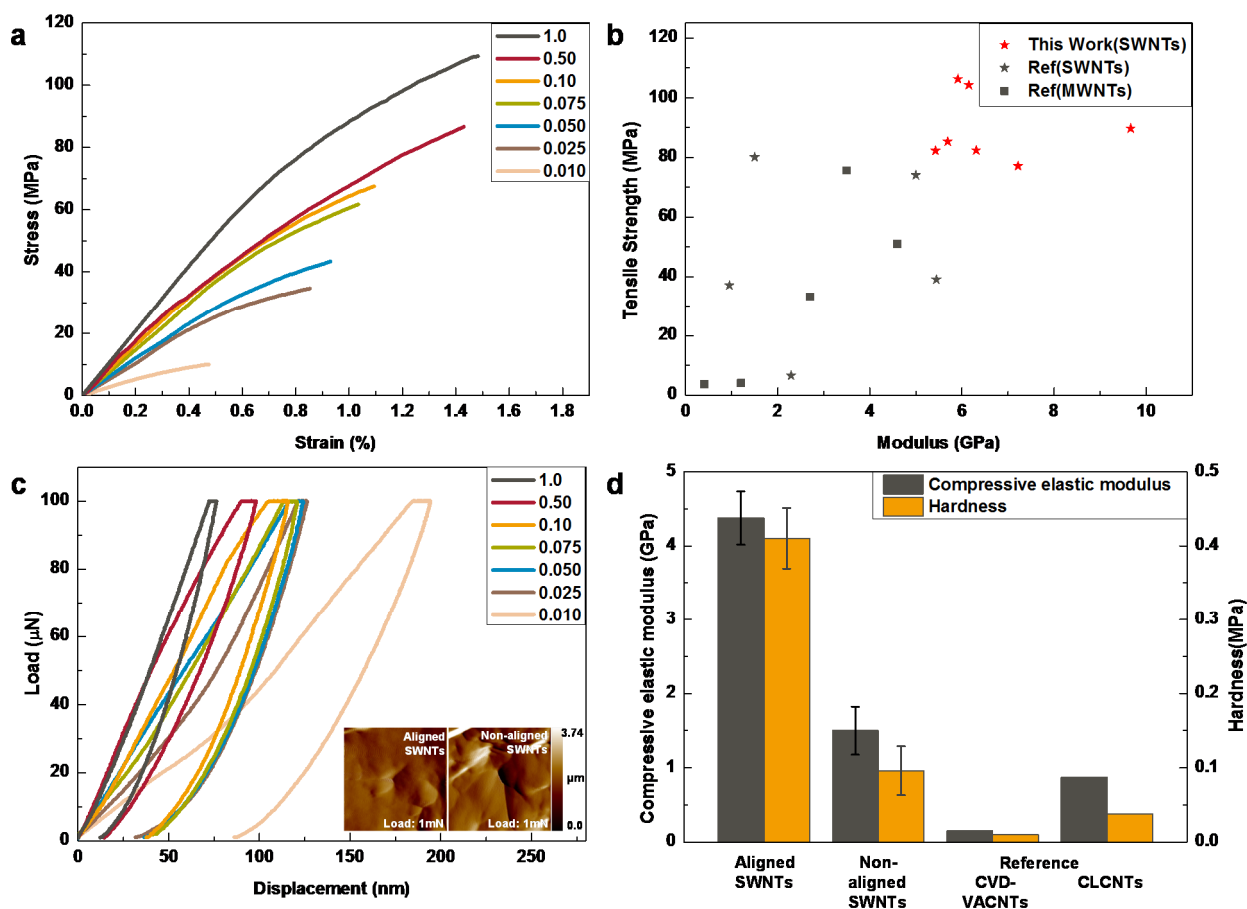


Fig. 3.17. (a) Representative tensile stress-strain curves of SWNT buckypapers prepared under various suspension concentrations (mg/mL). (b) Comparison of tensile strength and modulus for CNT buckypapers. (c) Representative nanoindentation load-displacement curves of SWNT buckypapers prepared under various suspension concentrations (mg/mL). Inset AFM images show the surface of aligned (left, 1.0 mg/mL) and non-aligned (right, 0.01 mg/mL) SWNT papers after nanoindentation measurement applying 1 mN. (d) Comparison of compressive elastic modulus and hardness for a set of CNTs.

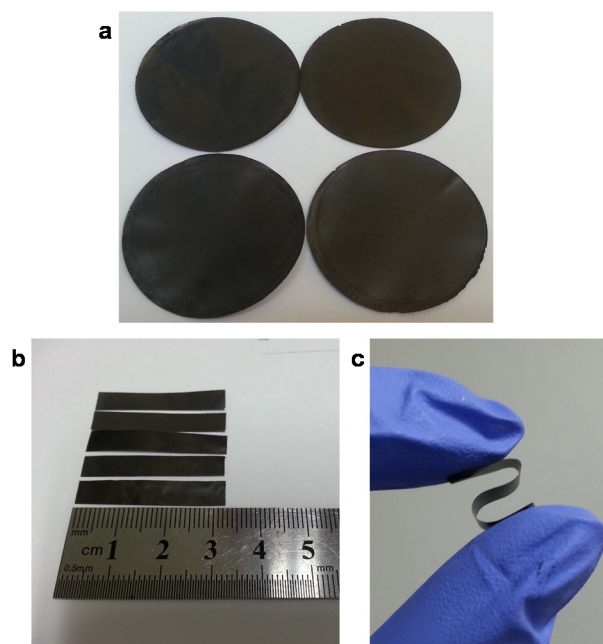


Fig. 3.18. Photographs of (a) freestanding aligned SWNT buckypapers, (b) papers which are cut into rectangular shape for tensile test, and (c) a bent piece of flexible paper.

Table 3.1. Comparison of mechanical properties of SWNT buckypapers prepared under various suspension concentrations

Sample		Tensile test			Nanoindentation test	
CNT suspension concentration (mg/mL) (vol%)	Modulus (GPa)	Tensile strength (MPa)	Elongation (%)	Modulus (GPa)	Hardness (MPa)	
1.0 0.0690	8.35 ± 2.75	94.62 ± 10.52	2.06 ± 1.08	4.38 ± 0.36	410.28 ± 40.85	
0.50 0.0340	6.40 ± 1.42	82.86 ± 17.39	1.52 ± 0.32	3.23 ± 0.35	337.13 ± 58.87	
0.10 0.00690	6.15 ± 0.56	67.43 ± 3.89	1.10 ± 0.04	3.26 ± 0.66	288.43 ± 95.44	
0.075 0.00520	5.17 ± 1.77	61.52 ± 10.45	1.27 ± 0.43	3.17 ± 0.25	256.48 ± 35.35	
0.050 0.00340	5.74 ± 0.43	53.02 ± 5.74	1.18 ± 0.23	2.99 ± 0.43	262.52 ± 56.87	
0.025 0.00170	5.78 ± 0.97	25.36 ± 9.21	0.59 ± 0.18	2.95 ± 0.56	268.67 ± 83.52	
0.010 0.00069	3.11 ± 0.43	12.38 ± 3.83	0.46 ± 0.12	1.50 ± 0.32	96.08 ± 32.79	

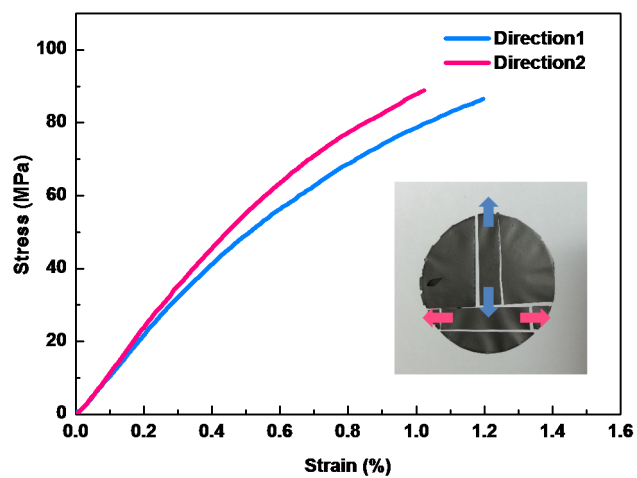


Fig. 3.19. Tensile stress-strain curves of two samples shown in inset (Photograph showing that SWNT buckypaper was split into two directions).

3.3 Experimental

Surface modification of the CNTs

The SWNTs (CVD, batch No. TNST, Purity > 95 wt.%, 1–2 nm in outer diameter, 10–15 μm in length) used in this work were purchased from Timesnano, Chengdu Organic Chemicals Co. Ltd., China. To effectively disperse the SWNTs, SWNTs (200 mg) were added to a mixture of concentrated H_2SO_4 (45 mL) and HNO_3 (15 mL). The suspension was stirred for 24 hours at 60°C , followed by washing with deionized (DI) water (1800 mL) and drying in a vacuum oven for 24 h.

To confirm the alignment of the CNTs of different type and surface modification, SWNTs (50 mg) and sodium dodecylbenzene sulfonate (SDBS) (500 mg) were soaked in DI water (500 mL) under tip sonication for 1 h. The sample was then filtered, washed with DI water several times, and dried. MWNTs (CVD, batch No. CM250, Purity > 95 wt.%, 15–20 nm in outer diameter, ~ 75 μm in length) were purchased from Hanhwa Chemical Co. Ltd. and oxidized for 3 hours at 60°C , as described above.

Preparation of the aligned CNT buckypaper

The surface-modified CNTs (100 mg, acid-treated SWNTs, MWNTs) were dispersed in N-methyl-2-pyrrolidone (NMP), and the SDBS-wrapped SWNTs were dispersed in DI water, respectively. All dispersions were subjected to tip sonication for 30 min. The first aligned CNT layer was prepared by filtering a tenth of the prepared suspension over a PTFE filtration membrane (pore size: 0.2 μm , Whatman). After all the solvent had been filtered, the same filtration process was applied to the separated suspension repeatedly

until the total quantity of CNTs on the membrane reached 10 mg/cm². The product was then dried in a vacuum oven for 24 h. To confirm the effect of filtration membrane and velocity on the alignment behavior, the AAO (pore size: 0.2 μm, Whatman) and PTFE (pore size: 0.5 μm, Whatman) was used, respectively.

Material characterization

SEM (JSM6700F Instrument, JEOL) was used to analyze the product morphology. The optical anisotropy of the product was imaged using an Olympus BX-51 microscope in the reflection mode between crossed polarizers. The birefringence strength was quantized based on the total intensity over a thousand pixels on the circular line indicated. All images were obtained under an exposure time of 0.25 sec. To analyze the size of aligned domains, we compiled statistics of the aligned domain size from five POM images per sample using Image-Pro Plus program (version 6.0.0.260.). Nitrogen adsorption isotherms (at 77 K) up to 1 bar were measured using a Micromeritics ASAP 2020 static volumetric gas adsorption instrument.

Tensile tests were performed using a universal testing machine (Instron-5543, Instron). For tensile tests, the papers were cut in a size (length: 32 mm, width: 6 mm) as shown in Figure S10. The gage length and loading rate were 16 mm and 1 mm/min. Nanoindentations were carried out using a nanoindentation system (Hysitron Tribolab 750, Hysitron Inc.) operated under load control at a constant loading rate of 20 μNs⁻¹ up to maximum load. To prevent the undesirable influence of the substrate, we limited the indentation depth to less than a tenth of the thickness of the sample. In addition, to avoid fracture while obtaining a clear unloading curve, the maximum stress was limited during

the test. The hardness and elastic modulus values were calculated according to the Oliver–Pharr method and were averaged over seventy measurements. After the nanoindentation measurements, the same indenter tip was used to image the surfaces of the samples. XPS (AXIS-His, KRATOS) was performed to analyze functional groups of CNTs.

Raman spectroscopy was performed using a RAMAN plus confocal laser Raman microscope (Nanophoton) at a laser wavelength of 532 nm, which permitted the study of structural changes. AFM images were collected using a SPA-400 (Seiko Instrument) operated in the tapping mode to analyze the physical characteristics of the acid-oxidized SWNTs. The UV-vis absorption spectra of the CNT suspensions were recorded using a Cary 5000 (Varian Inc.).

3.4 Conclusion

We developed a facile approach to self-assembled well-aligned CNTs with a high packing density using a filtration method. The self-alignment behavior of the CNTs could be facilitated using a suspension concentration that exceeds the critical concentration for achieving alignment. The well-aligned CNT arrangement formed a close-packed nanostructure that enhanced the strength, modulus, and hardness of the buckypapers. The proposed solution processing approach to align the CNTs opens up a scaling up opportunity for the manufacturing due to the flexible usage of CNT type and solvent recycling. We expect our findings to direct attention toward understanding and controlling the assembly behavior of desired CNTs in potential applications as high strength films, gas barrier films, sensors, and flexible electronic devices.

3.5 References

1. Baughman, R. H.; Zakhidov, A. A.; de Heer, W. A., Carbon nanotubes - the route toward applications. *Science* **2002**, *297*, 787-792.
2. Yu, M. F.; Lourie, O.; Dyer, M. J.; Moloni, K.; Kelly, T. F.; Ruoff, R. S., Strength and breaking mechanism of multiwalled carbon nanotubes under tensile load. *Science* **2000**, *287*, 637-640.
3. Ren, Z. F.; Huang, Z. P.; Xu, J. W.; Wang, J. H.; Bush, P.; Siegal, M. P.; Provencio, P. N., Synthesis of large arrays of well-aligned carbon nanotubes on glass. *Science* **1998**, *282*, 1105-1107.
4. Yu, G. H.; Cao, A. Y.; Lieber, C. M., Large-area blown bubble films of aligned nanowires and carbon nanotubes. *Nat Nanotechnol* **2007**, *2*, 372-377.
5. Kordas, K.; Mustonen, T.; Toth, G.; Vahakangas, J.; Uusimaki, A.; Jantunen, H.; Gupta, A.; Rao, K. V.; Vajtai, R.; Ajayan, P. M., Magnetic-field induced efficient alignment of carbon nanotubes in aqueous solutions. *Chem Mater* **2007**, *19*, 787-791.
6. Wang, B.; Ma, Y. F.; Li, N.; Wu, Y. P.; Li, F. F.; Chen, Y. S., Facile and Scalable Fabrication of Well-Aligned and Closely Packed Single-Walled Carbon Nanotube Films on Various Substrates. *Adv Mater* **2010**, *22*, 3067-3070.
7. Park, J. U.; Meitl, M. A.; Hur, S. H.; Usrey, M. L.; Strano, M. S.; Kenis, P. J. A.; Rogers, J. A., In situ deposition and patterning of single-walled carbon nanotubes by Laminar flow and controlled flocculation in microfluidic channels. *Angew Chem Int Edit* **2006**, *45*, 581-585.
8. Smith, B. W.; Benes, Z.; Luzzi, D. E.; Fischer, J. E.; Walters, D. A.; Casavant, M. J.; Schmidt, J.; Smalley, R. E., Structural anisotropy of magnetically aligned single wall carbon nanotube films. *Appl Phys Lett* **2000**, *77*, 663-665.

9. Kaida, S.; Matsui, J.; Sagae, T.; Hoshikawa, Y.; Kyotani, T.; Miyashita, T., The production of large scale ultrathin aligned CNT films by combining AC electric field with liquid flow. *Carbon* **2013**, *59*, 503-511.
10. Allen, R.; Fuller, G. G.; Bao, Z. N., Aligned SWNT Films from Low-Yield Stress Gels and Their Transparent Electrode Performance. *Acs Appl Mater Inter* **2013**, *5*, 7244-7252.
11. Zamora-Ledezma, C.; Blanc, C.; Maugey, M.; Zakri, C.; Poulin, P.; Anglaret, E., Anisotropic Thin Films of Single-Wall Carbon Nanotubes from Aligned Lyotropic Nematic Suspensions. *Nano Lett* **2008**, *8*, 4103-4107.
12. Vigolo, B.; Penicaud, A.; Coulon, C.; Sauder, C.; Pailier, R.; Journet, C.; Bernier, P.; Poulin, P., Macroscopic fibers and ribbons of oriented carbon nanotubes. *Science* **2000**, *290*, 1331-1334.
13. Dierking, I.; Scalia, G.; Morales, P.; LeClere, D., Aligning and reorienting carbon nanotubes with nematic liquid crystals. *Adv Mater* **2004**, *16*, 865-869.
14. Lagerwall, J.; Scalia, G.; Haluska, M.; Dettlaff-Weglikowska, U.; Roth, S.; Giesselmann, F., Nanotube alignment using lyotropic liquid crystals. *Adv Mater* **2007**, *19*, 359-364.
15. Lynch, M. D.; Patrick, D. L., Organizing carbon nanotubes with liquid crystals. *Nano Lett* **2002**, *2*, 1197-1201.
16. Ko, H.; Tsukruk, V. V., Liquid-crystalline processing of highly oriented carbon nanotube arrays for thin-film transistors. *Nano Lett* **2006**, *6*, 1443-1448.
17. Jang, E. Y.; Kang, T. J.; Im, H.; Baek, S. J.; Kim, S.; Jeong, D. H.; Park, Y. W.; Kim, Y. H., Macroscopic Single-Walled-Carbon-Nanotube Fiber Self-Assembled by Dip-Coating Method. *Adv Mater* **2009**, *21*, 4357-4361.

18. Badaire, S.; Zakri, C.; Maugey, M.; Derre, A.; Barisci, J. N.; Wallace, G.; Poulin, P., Liquid crystals of DNA-stabilized carbon nanotubes. *Adv Mater* **2005**, *17*, 1673-1676.
19. Davis, V. A.; Parra-Vasquez, A. N. G.; Green, M. J.; Rai, P. K.; Behabtu, N.; Prieto, V.; Booker, R. D.; Schmidt, J.; Kesselman, E.; Zhou, W.; Fan, H.; Adams, W. W.; Hauge, R. H.; Fischer, J. E.; Cohen, Y.; Talmon, Y.; Smalley, R. E.; Pasquali, M., True solutions of single-walled carbon nanotubes for assembly into macroscopic materials. *Nat Nanotechnol* **2009**, *4*, 830-834.
20. Rai, P. K.; Pinnick, R. A.; Parra-Vasquez, A. N. G.; Davis, V. A.; Schmidt, H. K.; Hauge, R. H.; Smalley, R. E.; Pasquali, M., Isotropic-nematic phase transition of single-walled carbon nanotubes in strong acids. *J Am Chem Soc* **2006**, *128*, 591-595.
21. Song, W. H.; Kinloch, I. A.; Windle, A. H., Nematic liquid crystallinity of multiwall carbon nanotubes. *Science* **2003**, *302*, 1363-1363.
22. Chan, C.; Crawford, G.; Gao, Y. M.; Hurt, R.; Jian, K. Q.; Li, H.; Sheldon, B.; Sousa, M.; Yang, N., Liquid crystal engineering of carbon nanofibers and nanotubes. *Carbon* **2005**, *43*, 2431-2440.
23. Lee, K. E.; Kim, J. E.; Maiti, U. N.; Lim, J.; Hwang, J. O.; Shim, J.; Oh, J. J.; Yun, T.; Kim, S. O., Liquid Crystal Size Selection of Large-Size Graphene Oxide for Size-Dependent N-Doping and Oxygen Reduction Catalysis. *Acs Nano* **2014**, *8*, 9073-9080.
24. Kim, J. E.; Han, T. H.; Lee, S. H.; Kim, J. Y.; Ahn, C. W.; Yun, J. M.; Kim, S. O., Graphene Oxide Liquid Crystals. *Angew Chem Int Edit* **2011**, *50*, 3043-3047.
25. Lee, S. H.; Park, J. S.; Lim, B. K.; Bin Mo, C.; Lee, W. J.; Lee, J. M.; Hong, S. H.; Kim, S. O., Highly entangled carbon nanotube scaffolds by self-organized aqueous droplets. *Soft Matter* **2009**, *5*, 2343-2346.

26. Onsager, L., The Effects of Shape on the Interaction of Colloidal Particles. *Ann Ny Acad Sci* **1949**, *51*, 627-659.
27. Davis, V. A.; Ericson, L. M.; Parra-Vasquez, A. N. G.; Fan, H.; Wang, Y. H.; V, P.; Longoria, J. A.; Ramesh, S.; Saini, R. K.; Kittrell, C.; Billups, W. E.; Adams, W. W.; Hauge, R. H.; Smalley, R. E.; Pasquali, M., Phase Behavior and rheology of SWNTs in superacids. *Macromolecules* **2004**, *37*, 154-160.
28. Song, W. H.; Windle, A. H., Isotropic-nematic phase transition of dispersions of multiwall carbon nanotubes. *Macromolecules* **2005**, *38*, 6181-6188.
29. Zhang, S. J.; Kumar, S., Carbon nanotubes as liquid crystals. *Small* **2008**, *4*, 1270-1283.
30. Deegan, R. D.; Bakajin, O.; Dupont, T. F.; Huber, G.; Nagel, S. R.; Witten, T. A., Capillary flow as the cause of ring stains from dried liquid drops. *Nature* **1997**, *389*, 827-829.
31. Zhang, S. J.; Li, Q. W.; Kinloch, I. A.; Windle, A. H., Ordering in a Droplet of an Aqueous Suspension of Single-Wall Carbon Nanotubes on a Solid Substrate. *Langmuir* **2010**, *26*, 2107-2112.
32. Fu, W. Q.; Liu, L.; Jiang, K. L.; Li, Q. Q.; Fan, S. S., Super-aligned carbon nanotube films as aligning layers and transparent electrodes for liquid crystal displays. *Carbon* **2010**, *48*, 1876-1879.
33. Mrozek, R. A.; Kim, B. S.; Holmberg, V. C.; Taton, T. A., Homogeneous, coaxial liquid crystal domain growth from carbon nanotube seeds. *Nano Lett* **2003**, *3*, 1665-1669.
34. Russell, J. M.; Oh, S. J.; LaRue, I.; Zhou, O.; Samulski, E. T., Alignment of nematic liquid crystals using carbon nanotube films. *Thin Solid Films* **2006**, *509*, 53-57.

35. Flory, P. J., Phase Equilibria in Solutions of Rod-Like Particles. *Proc R Soc Lon Ser-A* **1956**, *234*, 73-89.
36. Cho, H. G. Dispersion of carbon nanotubes in solvent and polymer matrix. Ph.D. Thesis, Seoul National University, **2010**.
37. Kim, S. W.; Kim, T.; Kim, Y. S.; Choi, H. S.; Lim, H. J.; Yang, S. J.; Park, C. R., Surface modifications for the effective dispersion of carbon nanotubes in solvents and polymers. *Carbon* **2012**, *50*, 3-33.
38. Oh, J. Y.; Choi, H. S.; Kim, M. S.; Kim, Y. S.; Park, C. R., Effects of morphological characteristics of Pt nanoparticles supported on poly(acrylic acid)-wrapped multiwalled carbon nanotubes on electrochemical performance of direct methanol fuel cells. *J Mater Res* **2012**, *27*, 2035-2045.
39. Lee, S. H.; Lee, D. H.; Lee, W. J.; Kim, S. O., Tailored Assembly of Carbon Nanotubes and Graphene. *Adv Funct Mater* **2011**, *21*, 1338-1354.
40. Liu, W. B.; Pei, S. F.; Du, J. H.; Liu, B. L.; Gao, L. B.; Su, Y.; Liu, C.; Cheng, H. M., Additive-Free Dispersion of Single-Walled Carbon Nanotubes and Its Application for Transparent Conductive Films. *Adv Funct Mater* **2011**, *21*, 2330-2337.
41. Liu, X. Y.; Hurt, R. H.; Kane, A. B., Biodurability of single-walled carbon nanotubes depends on surface functionalization. *Carbon* **2010**, *48*, 1961-1969.
42. Hill, F. A.; Havel, T. F.; Hart, A. J.; Livermore, C., Enhancing the Tensile Properties of Continuous Millimeter-Scale Carbon Nanotube Fibers by Densification. *ACS Appl Mater Inter* **2013**, *5*, 7198-7207.
43. Boncel, S.; Sundaram, R. M.; Windle, A. H.; Koziol, K. K. K., Enhancement of the Mechanical Properties of Directly Spun CNT Fibers by Chemical Treatment. *Acs Nano* **2011**, *5*, 9339-9344.

44. Kozlov, M. E.; Capps, R. C.; Sampson, W. M.; Ebron, V. H.; Ferraris, J. P.; Baughman, R. H., Spinning solid and hollow polymer-free carbon nanotube fibers. *Adv Mater* **2005**, *17*, 614-617.
45. Zhang, X. B.; Jiang, K. L.; Teng, C.; Liu, P.; Zhang, L.; Kong, J.; Zhang, T. H.; Li, Q. Q.; Fan, S. S., Spinning and processing continuous yarns from 4-inch wafer scale super-aligned carbon nanotube arrays. *Adv Mater* **2006**, *18*, 1505-1510.
46. Koziol, K.; Vilatela, J.; Moisala, A.; Motta, M.; Cunniff, P.; Sennett, M.; Windle, A., High-performance carbon nanotube fiber. *Science* **2007**, *318*, 1892-1895.
47. Dettlaff-Weglikowska, U.; Skakalova, V.; Graupner, R.; Jhang, S. H.; Kim, B. H.; Lee, H. J.; Ley, L.; Park, Y. W.; Berber, S.; Tomanek, D.; Roth, S., Effect of SOCl₂ treatment on electrical and mechanical properties of single-wall carbon nanotube networks. *J Am Chem Soc* **2005**, *127*, 5125-5131.
48. Pham, G. T.; Park, Y. B.; Wang, S. R.; Liang, Z. Y.; Wang, B.; Zhang, C.; Funchess, P.; Kramer, L., Mechanical and electrical properties of polycarbonate nanotube buckypaper composite sheets. *Nanotechnology* **2008**, *19*, 325705.
49. Suppiger, D.; Busato, S.; Ermanni, P., Characterization of single-walled carbon nanotube mats and their performance as electromechanical actuators. *Carbon* **2008**, *46*, 1085-1090.
50. Zhang, X. F.; Sreekumar, T. V.; Liu, T.; Kumar, S., Properties and structure of nitric acid oxidized single wall carbon nanotube films. *J Phys Chem B* **2004**, *108*, 16435-16440.
51. Wang, S. R.; Liang, Z. Y.; Wang, B.; Zhang, C., High-strength and multifunctional macroscopic fabric of single-walled carbon nanotubes. *Adv Mater* **2007**, *19*, 1257-1261.

52. Ventura, D. N.; Stone, R. A.; Chen, K. S.; Hariri, H. H.; Riddle, K. A.; Fellers, T. J.; Yun, C. S.; Strouse, G. F.; Kroto, H. W.; Acquah, S. F. A., Assembly of cross-linked multi-walled carbon nanotube mats. *Carbon* **2010**, *48*, 987-994.
53. Berhan, L.; Yi, Y. B.; Sastry, A. M.; Munoz, E.; Selvidge, M.; Baughman, R., Mechanical properties of nanotube sheets: Alterations in joint morphology and achievable moduli in manufacturable materials. *J Appl Phys* **2004**, *95*, 4335-4345.
54. Spitalsky, Z.; Tsoukleri, G.; Tasis, D.; Krontiras, C.; Georga, S. N.; Galiotis, C., High volume fraction carbon nanotube-epoxy composites. *Nanotechnology* **2009**, *20*, 405702.
55. Zhang, X. W., Hydroentangling: A Novel Approach to High-Speed Fabrication of Carbon Nanotube Membranes. *Adv Mater* **2008**, *20*, 4140-4144.
56. Inoue, Y.; Suzuki, Y.; Minami, Y.; Muramatsu, J.; Shimamura, Y.; Suzuki, K.; Ghemes, A.; Okada, M.; Sakakibara, S.; Mimura, F.; Naito, K., Anisotropic carbon nanotube papers fabricated from multiwalled carbon nanotube webs. *Carbon* **2011**, *49*, 2437-2443.
57. Ruoff, R. S.; Tersoff, J.; Lorents, D. C.; Subramoney, S.; Chan, B., Radial Deformation of Carbon Nanotubes by Van-Der-Waals Forces. *Nature* **1993**, *364*, 514-516.
58. Pathak, S.; Cambaz, Z. G.; Kalidindi, S. R.; Swadener, J. G.; Gogotsi, Y., Viscoelasticity and high buckling stress of dense carbon nanotube brushes. *Carbon* **2009**, *47*, 1969-1976.
59. Oliver, W. C.; Pharr, G. M., An Improved Technique for Determining Hardness and Elastic-Modulus Using Load and Displacement Sensing Indentation Experiments. *J Mater Res* **1992**, *7*, 1564-1583.

60. Presser, V.; Heon, M.; Gogotsi, Y., Carbide-Derived Carbons - From Porous Networks to Nanotubes and Graphene. *Adv Funct Mater* **2011**, *21*, 810-833.
61. Gao, Y.; Kodama, T.; Won, Y.; Dogbe, S.; Pan, L.; Goodson, K. E., Impact of nanotube density and alignment on the elastic modulus near the top and base surfaces of aligned multi-walled carbon nanotube films. *Carbon* **2012**, *50*, 3789-3798.
62. Cha, S. I.; Kim, K. T.; Lee, K. H.; Mo, C. B.; Jeong, Y. J.; Hong, S. H., Mechanical and electrical properties of cross-linked carbon nanotubes. *Carbon* **2008**, *46*, 482-488.

Chapter 4 Preparation and Mechanical Performance of Bone-mimicking Size-Tuned GO@CNT Hybrid Film

4.1 Introduction

The body frame for portable electronics and vehicles needs lightweight materials with high mechanical performance. Thus, CNTs have attracted great attention as promising building blocks due to the extraordinary mechanical and electrical properties.^{1,2} The key issue for utilizing their individual properties both at microscopic and macroscopic levels is in assembling CNTs into nanostructures with favorable energy/stress transfer pathways.³ One way to fulfill this requirement would be to align nanostructured CNTs along with tightly-connected individual CNTs through chemical cross-linking.^{4, 5} Several approaches have been made in the past few years to achieve the structure including CNT fibers and films through direct spinning⁶⁻⁸ and spinning from CNT forests,⁹⁻¹¹ respectively. Even though these methods have achieved enhanced mechanical properties, they lack the chemical linking between individual CNTs in their dry processes and hinder the construction of nanostructured CNTs-assembly along with the extension of novel CNTs-assembly to multifarious applications.

GO with lots of functional groups has been regarded as an efficient building block due to the abundant functional groups that facilitate additional improvements in interfacial strength by creating sheet-sheet intermolecular bridges.¹²⁻¹⁷ For instance, the mechanical

properties of cross-linked GO films are held together by divalent ion,¹⁸ borate,¹⁹ and glutaraldehyde (GA)²⁰ while hybrid composite films based on GO and poly(vinyl alcohol) (PVA),²¹ poly(dopamine) (PDA)²² were superior to those of common GO films formed by van der Waals interaction. Recent advances in CNTs-GO hybrid composites - which include CNTs-GO fibers fabricated by a bio-inspired cross-linking reaction,²³ CNTs-GO-polymer composite,²⁴ and GO-coated dry-spun CNTs fibers²⁵ - allowed for further improvements in the mechanical properties. However, the rationale behind effective load-bearing architectures of the reported composite materials is still unclear. The outstanding mechanical properties were determined by testing tiny fiber samples at sub-micron diameter and insufficient 1~2 mm gage length.^{26, 27} Overall, the development of novel hybrid materials between CNTs and GOs featuring mass productivity with superior mechanical properties and further understanding about effective load-bearing architecture from hybrid microstructure are needed.

In many natural materials, bone combines strength with toughness due to its complex architecture, which consists of hydroxyapatite nanocrystals incorporated with collagen molecules. Previous studies have revealed the key mechanistic principle of bone and the strengthening role of mineral hydroxyapatite.²⁸⁻³¹ The distinctive nanostructure based on electrostatic interactions and hydrogen bonding between plate-shaped hydroxyapatite nanocrystals and fiber-shaped collagen molecules provides unique load-bearing characteristics, making bone both strong and tough. In this respect, mimicking the natural bone structure inspires a new approach toward novel materials utilizing unusual combinations of strength and toughness. However, a practical method for large-scale preparation of bioinspired bulk composite is still scarce.

Inspired by natural bone, we introduce a nearly monolayered small GOs into SWNT based bulky film to form an effective load-bearing hybrid architecture. In general, only GO-based film or fiber prefer to use larger-size GO sheets to induce a strong inter-sheet π - π interaction for increasing the packing density of material, which is a key parameter in determining the mechanical properties.³² In our study, however, we reduced the GO sheet size to weaken the inter-sheet π - π interaction, enabling the incorporation of thinner GO sheets into the SWNTs assembly. The thinner and smaller GO sheets allow a more homogeneous cross-linking reaction between SWNTs and GO sheets and form a bone-mimetic load-bearing architecture. This leads to enhanced mechanical strength, modulus, toughness, and even electrical conductivity compared to those of previous SWNTs-GOs hybridized composites. Further elaboration on the mechanism study by *in-situ* Raman spectroscopy during tensile testing shows that the thinner and smaller size-GO sheet acts as an efficient “stress-transfer medium” comparable to hydroxyapatite nanocrystals in providing strength and toughness to the bone.

4.2 Results and discussion

The SWNT-GO film fabrication is illustrated in Figure 4.1. Prior to fabrication, SWNTs (Figure 4.2) were oxidized by a mixed acid and GO was prepared by a modified Hummers method as described in the experimental section. First, the SWNTs and size-controlled GO sheets were uniformly dispersed in dimethylformamide (DMF) at a 3:1 ratio by weight of SWNT to GO. Then, the SWNTs and GO sheets were interconnected with p-phenylenediamine (PPD) by stirring for 24 h. The cross-linked SWNT-GO suspension was filtered and washed in DMF before drying in the vacuum oven at room temperature to fabricate the black SWNT-GO film.

The GO lateral size is well known to determine the microstructures and properties of resulting GO materials. Relatively large GO sheets have fewer structural defects and more intersheet junctions so there are ordered, stacked microstructures. These have great potential for structure materials, electronic devices, and gas barriers.³²⁻³⁵ On the other hand, small GO sheets have abundant active functional edging sites, which are desirable for utilization in chemical reactions.^{36, 37} To investigate the influence of GO size on the efficiency of cross-linking and load-bearing, the GO size was controlled by varying the tip sonication time from 0 to 30 min. These GO sheets were denoted as GOXX, where XX refers to the sonication time. We conducted dynamic light scattering (DLS) to measure the lateral size distributions of GO sheets in solution (Figure 4.1b). As expected, the size distribution of GO sheets shifted to smaller values depending on the sonication time. The average lateral sizes of GO0, GO10, GO20, and GO30 were 10255.5, 405.9, 260.6, and 210.5 nm, respectively. The size variation indicated that the lateral size of GO sheets were reduced significantly within a very short sonication time, as shown in Table 4.1. We used the transmission electron microscopy (TEM) to analyze the lateral size of

the obtained GO sheets, as shown in Figure 4.3. This confirmed that the GO30 sheet size was similar to the values determined by DLS measurements. According to Onsager's theory, large GO sheets can form a liquid crystalline phase due to their high aspect ratio.^{35, 38-40} Indeed, prominent birefringence was observed in the GO0 sample, as shown in Figure 4.1b, which indicate a stable nematic phase formation. On the other hand, no birefringence was observed in GO10, GO20, and GO30 samples under crossed polarizers, so demonstrate a significantly reduced aspect ratio and intersheet π - π interaction of obtained GO sheets by sonication. This suggests that reducing the lateral size and intersheet π - π interaction of GO sheets from a facile sonication method can be accomplished. In general, this is highly advantageous for the homogeneous incorporation of GO sheets in densely packed SWNT film.

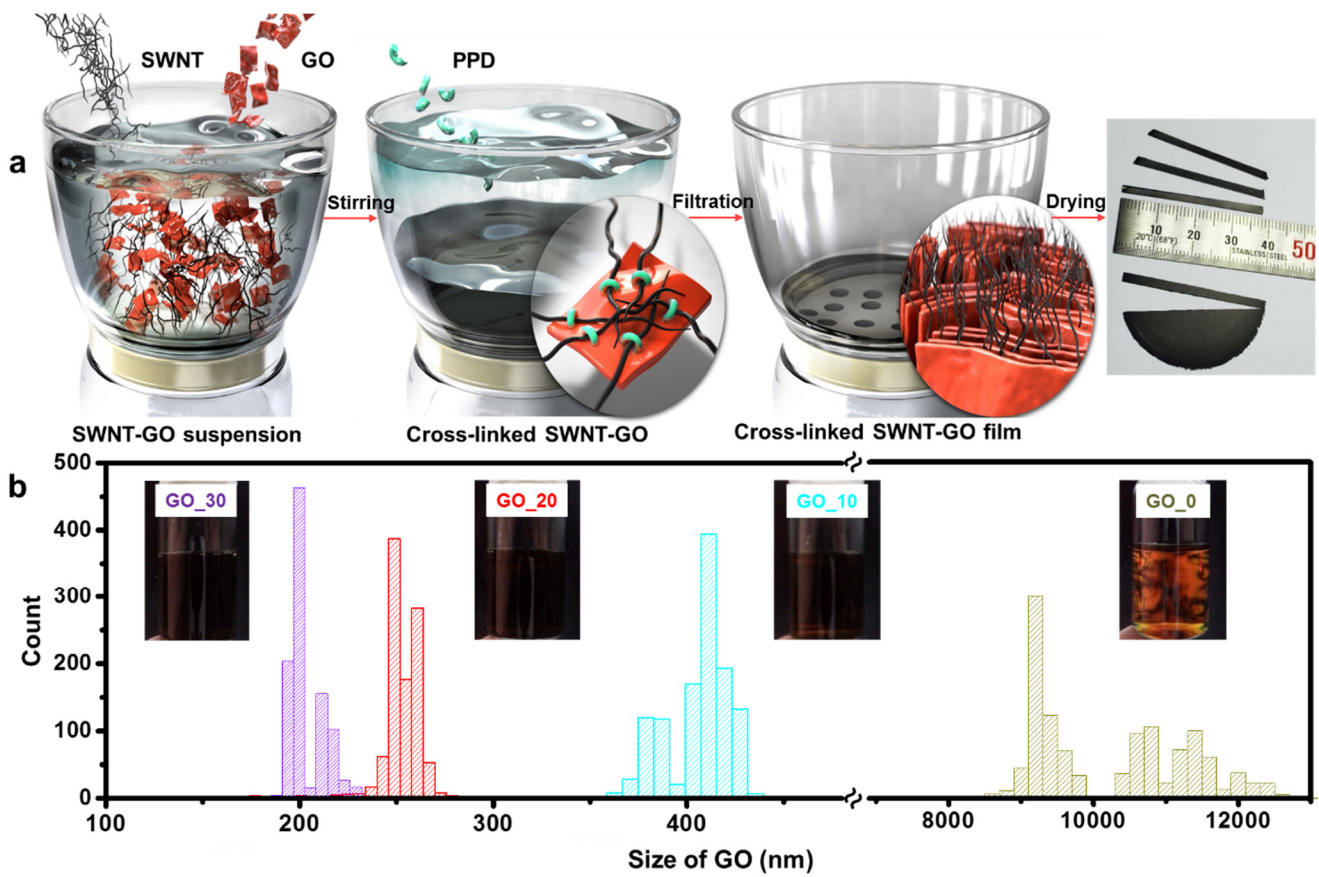


Fig. 4.1. a) Preparation process of SWNT-GO hybrid film. b) The size distribution of GO sheets depending on the tip sonication time (0 ~ 30 min). The insets are the polarized 1.0 mg/mL GO suspension optical micrographs.

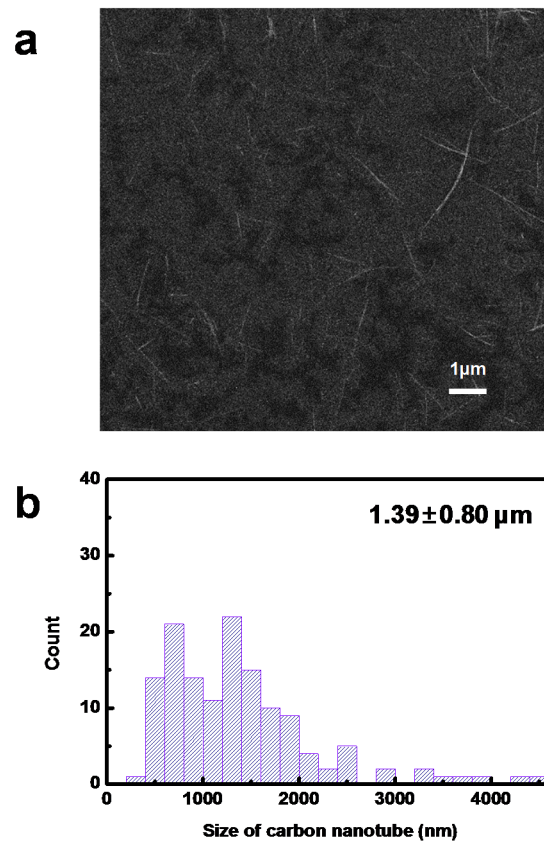


Fig. 4.2. a) SEM image of individualized SWNTs on a Si wafer and b) their length distribution.

Table 4.1. Size of fragmented GO sheets characterized by DLS measurement

Sonicated time		Size of GO	
Tip sonication (min)	Bath sonication (h)	AVG (nm)	STDEV
0	6	10255.5	1060.5
1	6	1130.0	31.4
10	6	405.9	16.4
20	6	260.6	2.5
30	6	210.5	8.6

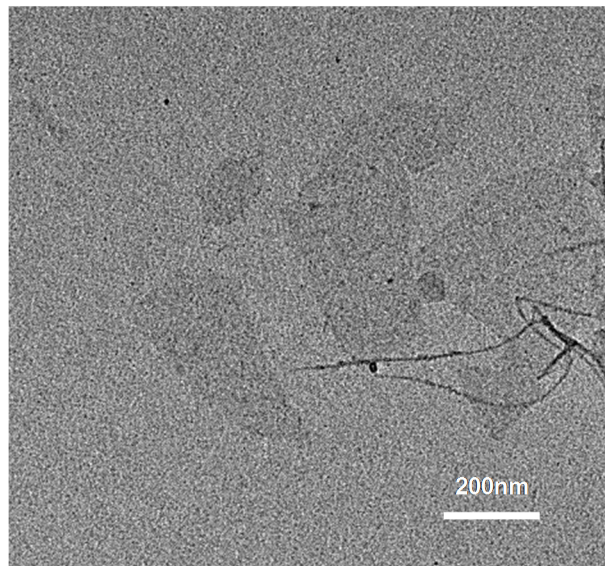


Fig. 4.3. TEM image of GO30 sheets and SWNTs after sonication.

The reduced GO sample size and weak intersheet π - π interaction have influenced the cross-linking reaction rate. When the PPD cross-linking agent dissolved in SWNT-GO suspensions, the reactions between SWNTs and GO sheets led to the precipitation of SWNT-GO, as shown in Figure 4.4a. In contrast to SWNT-GO10, GO20, and GO30, the SWNTs and GO sheets were still well dispersed in the suspension without precipitation even after 3 h of stirring, which indicate a late cross-linking reaction. These results were quantitatively confirmed by UV-vis spectroscopy monitoring the SWNT-GO suspension absorbance as a function of cross-linking time (Figure 4.4b). As the cross-linking reaction time increased, the SWNT-GO30 suspension precipitated much faster than others, implying that the smaller GO sheet size initiated a faster cross-linking reaction. A X-ray photoelectron spectroscopy (XPS) was performed to verify the amide bond formation between SWNT and GO by adding the PPD cross-linking agent (Figure 4.4c). All the SWNT-GO samples with PPD molecules exhibited new peaks at around 400 eV binding energy, which are attributed to the N_{1s} species of C-N bonds. Furthermore, no peaks were observed for N_{1s} in SWNT-GO30 film without PPD molecules (Figure 4.5). TEM equipped with energy dispersive X-ray spectroscopy (EDX) elemental analysis was conducted to identify the spatial distribution of relevant atoms (C, O, and N). As indicated in Figure 4.6, N atoms from PPD molecules were uniformly distributed on the SWNT-GO30 surface, suggesting a successful amine functionalization. X-ray diffraction (XRD) patterns (Figure 4.4d) of GO films displayed characteristic GO peaks from an interlayer distance of 0.97 ~ 1.0 nm (2θ : around 9.0°).^{35, 41} However, in the case of SWNT-GO20 and -GO30 composite films (Figure 4.4e), the characteristics GO film peaks almost vanished, pointing to a very weak stacking along the c-axis. Consequently, well-dispersed, size-reduced GO sheets are homogeneously incorporated into SWNT films in the nearly mono-layered state without restacking themselves.

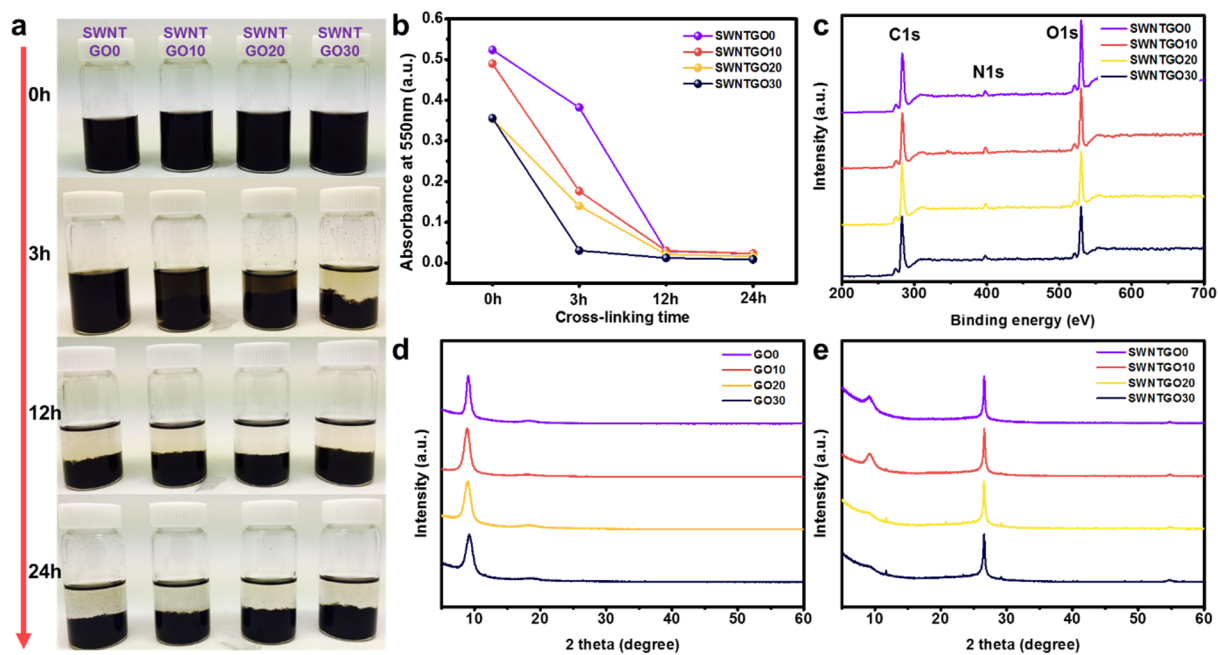


Fig. 4.4. a) SWNT-GO suspension precipitation depending on the cross-linking reaction between SWNTs and GO sheets by PPD molecules b) Absorbance at 550 nm of SWNT-GO suspensions acquired by UV-vis spectroscopy to quantitatively monitor the cross-linking reaction. c) XPS wide spectra of SWNT-GO films. XRD patterns of d) only GO sheets and e) SWNT-GO hybrid films.

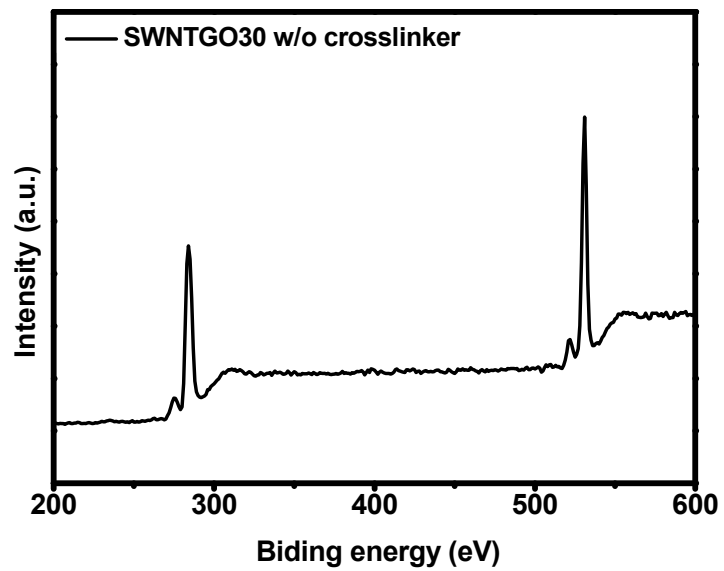


Fig. 4.5. XPS wide spectrum of SWNT-GO30 film without cross-linking agent.

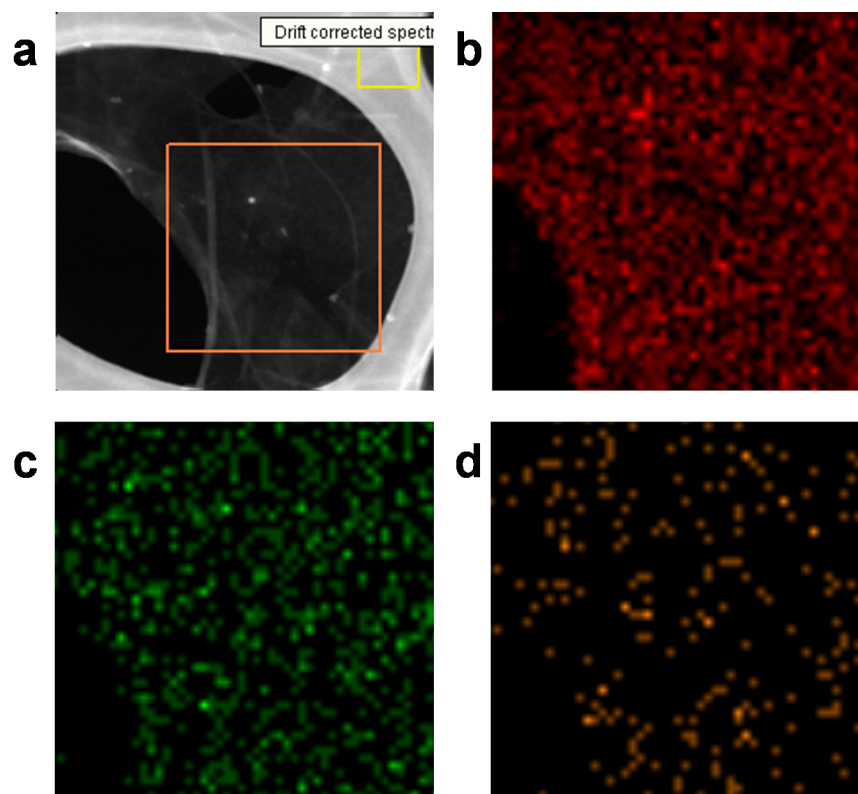


Fig. 4.6. a) TEM image of the SWNT-GO30 sample after cross-linking and elemental maps of b) carbon, c) oxygen, and d) nitrogen.

We studied the GO size effect on the mechanical properties of SWNT-GO films using a uniaxial tensile measurement. Figure 4.7a shows the representative stress-strain curves of SWNT-GO films along various GO sizes. The determined tensile strength, modulus, and toughness of SWNT-GO0 film were about 123.8 ± 25.0 MPa, 9.1 ± 0.8 GPa, and 2.0 ± 1.0 MJ/m³, respectively. By using smaller GO sheets in fabrication, the tensile strength, modulus, and toughness of SWNT-GO films gradually increased. Thus, the parameters reached up to 208.8 ± 34.3 MPa, 14.9 ± 2.3 GPa, and 3.3 ± 1.0 MJ/m³, respectively, when GO30 sheets were used. The obtained values of SWNT-GO30 film outperformed those of other films fabricated by pure SWNT, cross-linked SWNT, and pure SWNT/GO30 without PPD (Figure 4.8), which manifests the synergistic effect of the cross-linking reaction between SWNTs and GO30 sheets. The detailed mechanical and electrical characteristics of SWNT-GO films are summarized in Table 4.2.

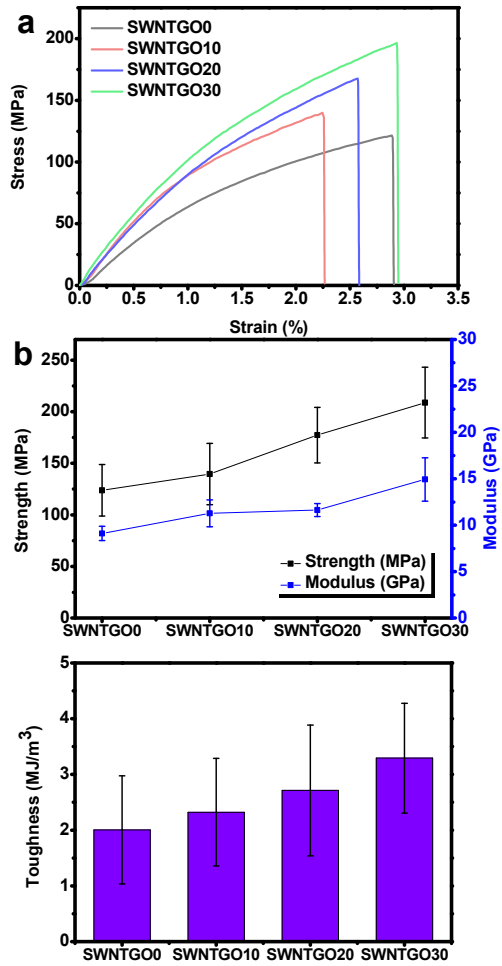


Fig. 4.7. a) Stress-strain curves of SWNT-GO0 (gray), -GO10 (pink), -GO20 (blue), and T-GO30 (green) films. b) Tensile strength (black squares) and elastic modulus (blue squares). c) Toughness values of SWNT-GO films

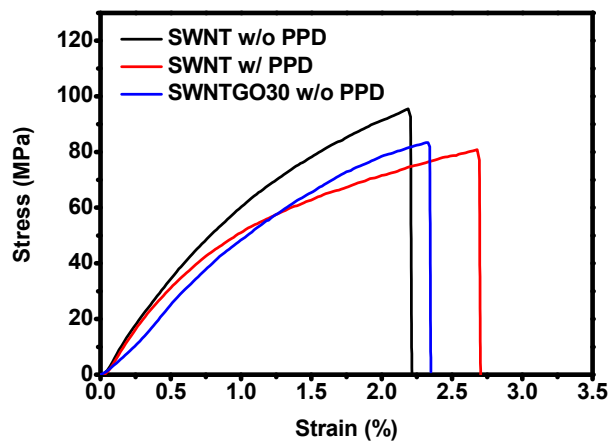


Fig. 4.8. Representative stress-strain curves of SWNT, SWNT with PPD, and SWNT-GO film without PPD.

Table 4.2. Summary of SWNT-GO film mechanical and electrical performance

Sample	Strength (MPa)	Modulus (GPa)	Elongation (%)	Toughness (MJ/m³)	Electrical conductivity (S/cm)
SWNTGO0	123.8 ± 25.0	9.1 ± 0.8	2.8 ± 1.1	2.0 ± 1.0	191.0±1.7
SWNTGO10	139.6 ± 29.7	11.3 ± 1.4	2.6 ± 0.6	2.3 ± 1.0	236.4±2.9
SWNTGO20	177.0 ± 20.5	11.6 ± 0.2	2.8 ± 0.5	2.9 ± 0.9	323.5±9.6
SWNTGO30	208.8 ± 34.3	14.9 ± 2.3	2.6 ± 0.4	3.3 ± 1.0	350.9±4.2

Previously reported cross-linked GO films¹⁸⁻²⁰ and their composite materials⁴²⁻⁴⁴ possess outstanding mechanical performances that generally exhibit low electrical conductivities due to the insulating characteristics of used GO sheets. Even if the used GO sheets in these materials were reduced by adding a reducing agent or thermal treatment, the electrical conductivity of these materials was not easily recovered because such materials were built with non-conductive cross-linking agents or polymer matrix, and the reduced GO sheets in such materials were inhomogeneously distributed to hamper the electric-conductive pathway formation. It is noteworthy that the electrical conductivity of SWNT-GO30 film surpasses those of other benchmark GO-based composite films. Furthermore, it is comparable to CNT film even without further GO reduction (see Figures 4.9a and 4.9b). We believe that the size-tuning strategy enables the GO sheets to be well-dispersed in a nearly mono-layered form. Thus, the insulating nature of the GO sheets might be negligible on the fabricated composite film.

We previously reported on self-assembled CNTs buckypaper³ by simple filtration of highly concentrated dispersion. Because of its aligned and dense microstructure, the material exhibited high tensile and compressive strength without any additives. Taking into account the 1-dimensional morphology and less-flexible rigid body of the CNTs, however, the desirable cross-linking reaction hardly occurred, so a cross-linking agent in the SWNT film would need additions that can serve more efficient cross-linking reactions (SWNT with PPD in Figures 4.8 and 4.9b). When considering mechanical properties of the reported materials (Figure 4.9b), the strength of the prepared SWNT-GO30 films exceeds that of GO films modified by multifarious linking ions,^{18, 19} composite with polymers,^{21, 22, 42-46} and natural materials.⁴⁷ Taking into consideration that strength and toughness are mutually exclusive, a competent SWNT-GO30 toughness can provide an alternative approach for developing an ideal compromise between ductility

and hardness. When a load is applied, it is speculated that the incorporated GO sheets are both well-distributed and nearly monolayered to make them a damage-tolerable material *via* promoting appropriate inter-sheets sliding, which operates efficacious stress-transfer and inhibits crack initiation.

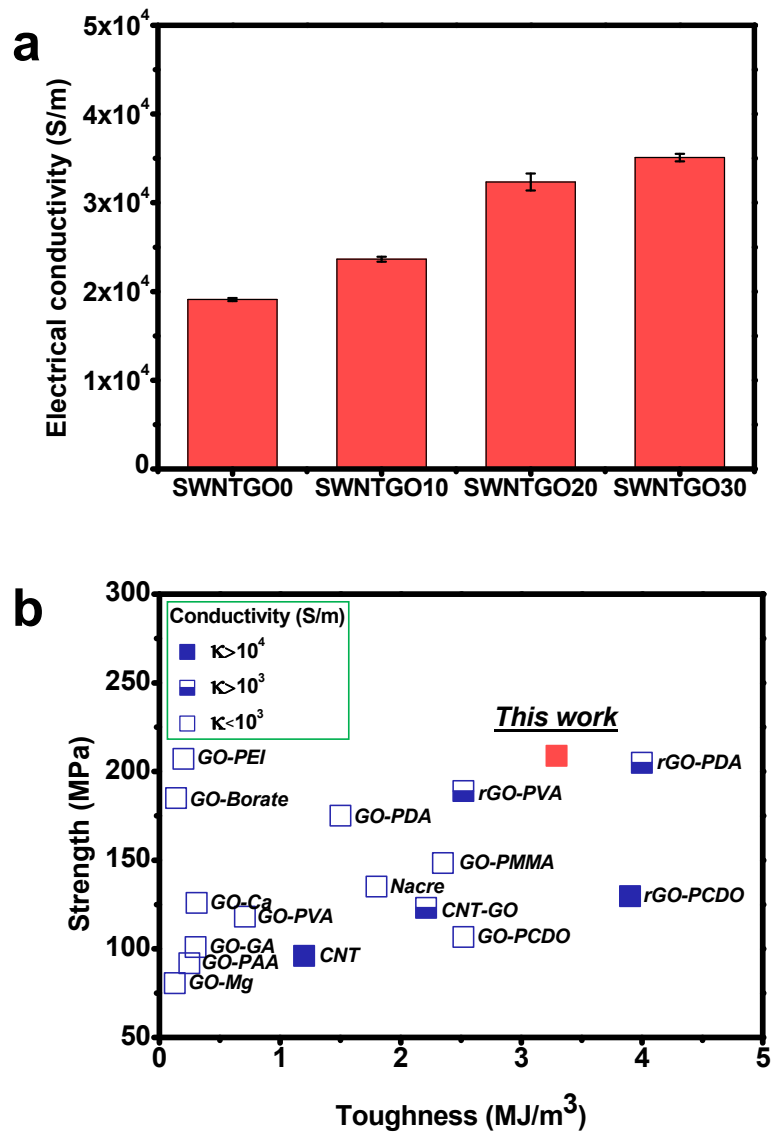


Fig. 4.9. a) Electrical conductivities of SWNT-GO films. b) Comparison of tensile strength and toughness values of prior-art materials. Fully-filled square, half-filled square, and non-filled square indicate the order of electrical conductivity.

The introduction of size-reduced GO sheets into the SWNTs resulted in different integrated surfaces and fractured ends during tensile loading. The surface morphologies of SWNT-GO films before and after tensile tests are observed using scanning electron microscopy (SEM), as shown in Figure 4.10. When utilizing the larger GO sheets (SWNT-GO0 film) for a stress-transfer medium, relatively irregular and rough morphology was found (Figure 4.10a). As the used GO sheet sizes decreased, the resultant hybrid films displayed more uniform, smoother, and denser surface morphology. Further investigations on the surface roughness through atomic force microscopy (AFM) with 10 μm x 10 μm scan area and line scan are consistent with SEM results (Figure 4.10i-l). The lower root-mean-square (RMS) value of the surface roughness has accounted for the long-range uniformity, dense packed nanostructure, and interconnectivity in nanoscale. As the used GO sheet sizes decreased, the roughness values continue to reduce, ensuring a more uniform and denser packed nanostructure. These nanostructures played a role in their ability to promote SWNTs sliding efficiently during tensile loading. Based on the observation that the number of SWNTs stuck out of the fractured composite after tensile test increased in accordance with decreasing surface roughness values (Figure 4.10e-h), we can conjecture that more nanotubes in SWNTs-GO30 participated in dissipating energy that was generated during deformation and reducing the driving force for cracking. These features constrain the deformation of the hybrid film and are the basis for increasing bone strength with collagen and hydroxyapatite nanocrystal.

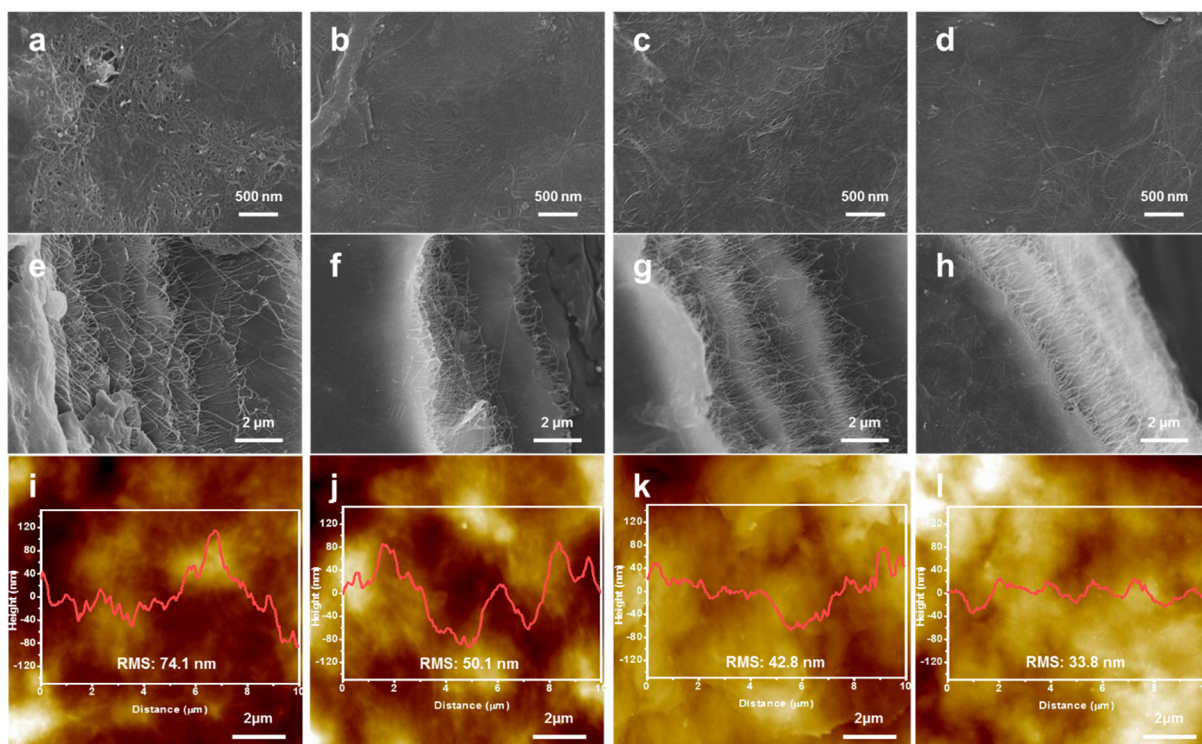


Fig. 4.10. SEM micrographs and large area AFM images with line scan results showing the surface morphologies and fractured ends after tensile testing of a, e, i) SWNT-GO0; b, f, j) SWNT-GO10; c, g, k) SWNT-GO20; and d, h, i) SWNT-GO30 films.

To further investigate the size effect of incorporated GO sheets on the stress transfer efficiency, we conducted an *in-situ* Raman spectroscopy measurement during tensile loading of SWNT-GO films, as shown in Figures 4.11a and b. It is suggested that the G' band shift in Raman spectrum can be considered a criterion to quantitatively characterize the load-sharing of sp² nanocarbons.⁴⁸⁻⁵⁰ In other words, the down shift of the G' peak position originating from the elongated carbon-carbon bonds under tensile strain indicate that the generated stress energy dissipates efficiently. Figures 4.11b shows a typical G' band Raman spectra change of SWNT-GO30 film during tensile loading (Figure 4.12 for G' band Raman spectra of SWNT-GO0, GO10, and GO20 films). The evident down shift and peak broadening of the G' band determined by the increased strain confirm that the evolved macroscale strain by axial tension was well-distributed to the hybrid film constituents: SWNTs and GO sheets. As shown in Figure 4.11c, the degree of stress transfer varied according to the used GO sheet size for hybrid films. The downshifts in SWNT-GO20 and -GO30 continued to occur even after exceeding 0.4% of tensile strain while the bigger GO sheets-based hybrid films (SWNT-GO0 and -GO10) displayed the change plateau after 0.4% of tensile strain. These trends highlighted a crucial role of used GO sheet size in hybrid films on determining stress transfer efficiency, and are indicative of resulting mechanical performances (Table 4.2). The TEM micrograph of the SWNT-GO30 (Figure 4.11d) exhibits uniform coverage of SWNTs with size-controlled GO sheets, leading to a favorable architecture for efficient stress transfer. We conjectured that the stress transfer efficiency can affect the relative orientation change of SWNTs in the hybrid film during tensile loading and thus measured the polarized Raman spectra to qualify the alignment along the tensile axis (Figure 4.11e and 4.13). The large difference in the Raman intensity depending on the polarization (parallel and perpendicular to tensile axis) provided a solid evidence for a complete alignment of the

SWNTs in hybrid film during tensile loading. The generated stress was well-distributed to the respective SWNTs in hybrid film and the stress-loaded SWNTs were more flexible in properly responding to the mechanical stimulus for achieving the desired mechanical performances. As expected, the largest intensity difference (Figure 4.11f) was obtained for the SWNT-GO30 in which the smallest GO sheets were used for the hybrid film. This demonstrates the efficient stress transfer of the microstructure. We further support the enhanced alignment of SWNTs upon stress loading by polarized optical microscopy (POM) images. For SWNT-GO20 and -GO30 films (smaller GO sheets used; Figure 4.11g and 4.14), there is strong birefringence on the exposed surface of fractured hybrid films, indicating well-aligned SWNTs. Others that used larger-scale GO sheets did not exhibit a birefringence. From these observations, we can conclude that the size-tuned GO sheets not only facilitated substantial stress transfer to the overall hybrid film, but also enabled the hybrid films to be responsive to mechanical stimulus, resulting in transmuting randomly-oriented SWNTs into highly-aligned SWNTs.

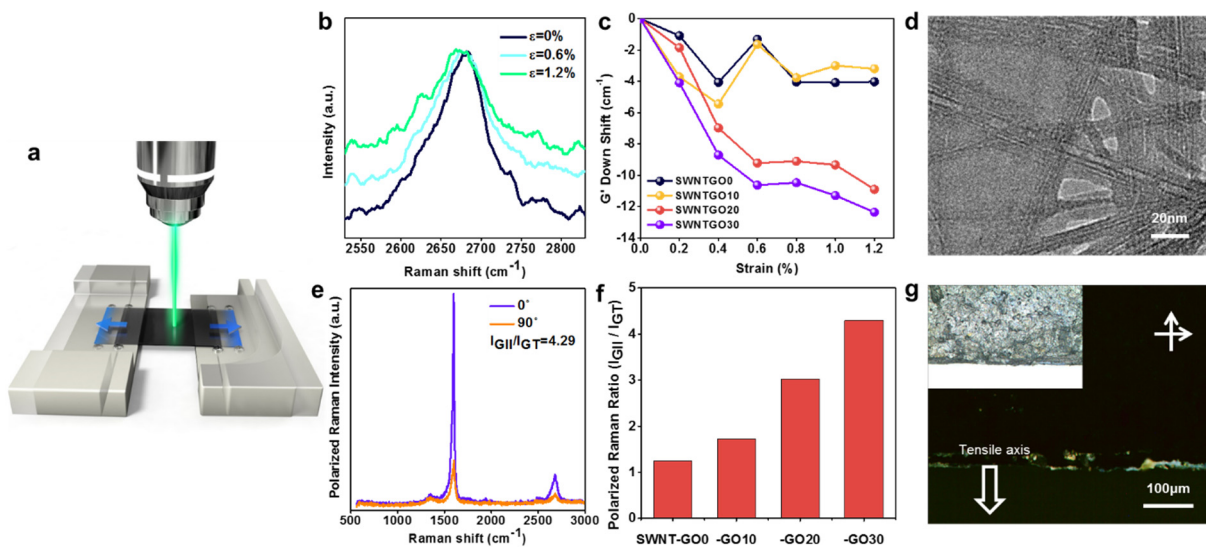


Fig. 4.11. a) Schematic illustration of *in-situ* Raman spectroscopy at tensile stage. b) G' band Raman spectra of SWNT-GO30 film under tensile strain. c) G' peak shift in the Raman spectra of the SWNT-GO films during tensile loading. d) TEM image showing the inter-connection between SWNTs and GO sheets. e) Polarized Raman spectra along the tensile axis showing relative orientation change of SWNT-GO30 after failure. f) Relative G peak intensity ratio in polarized Raman spectra of SWNT-GO films after failure. g) Fractured surface of SWNT-GO30 film between two crossed linear polarizer with an inset of normal OM image.

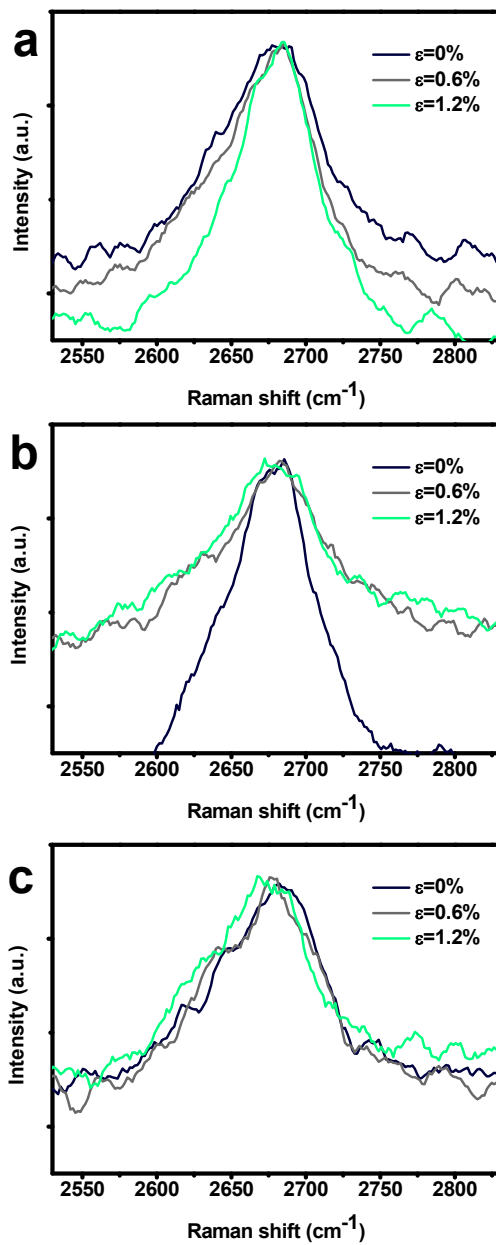


Fig. 4.12. G' band Raman spectra of a) SWNT-GO0, b) SWNT-GO10, and c) SWNT-GO20 films under tensile strain.

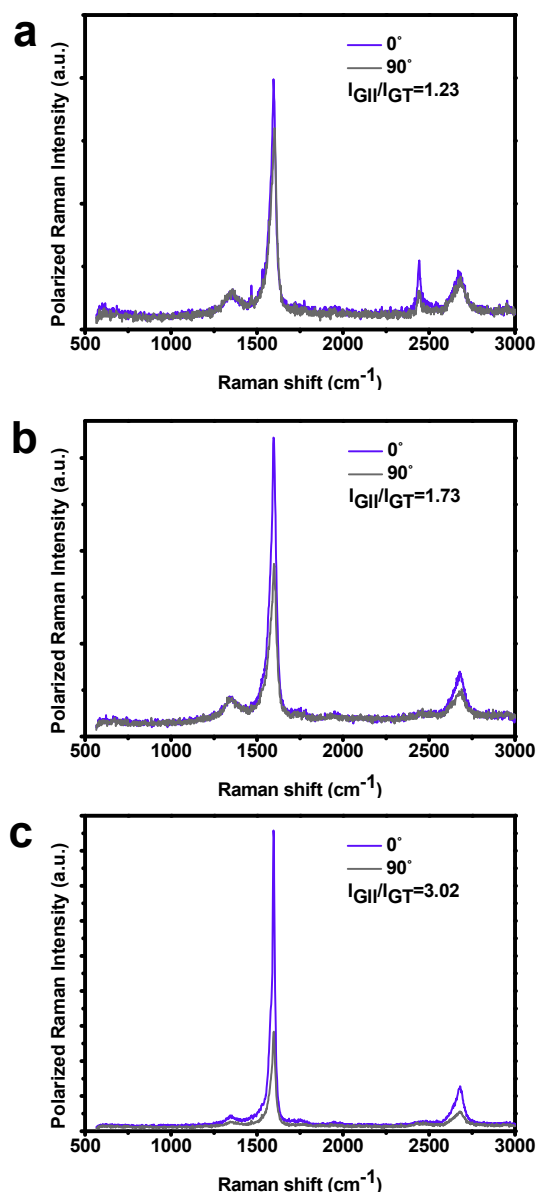


Fig. 4.13. Polarized Raman spectra along the tensile and perpendicular axis showing the relative orientation change of a) SWNT-GO0, b) SWNT-GO10, and c) SWNT-GO20 films after failure.

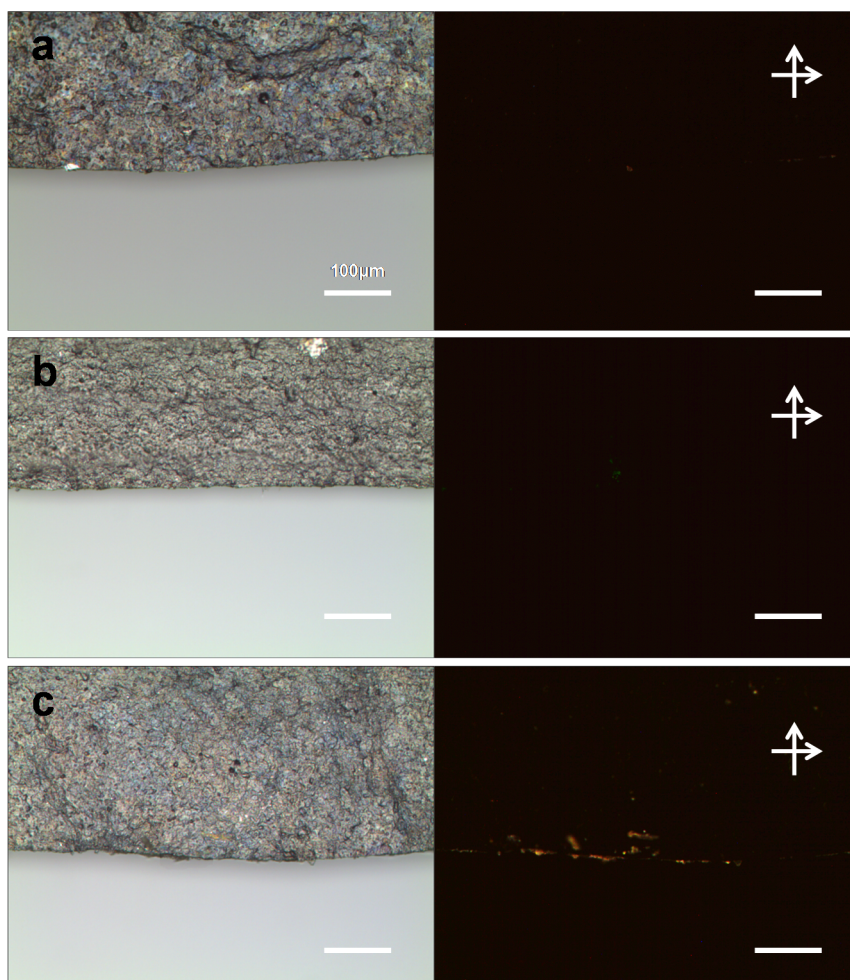


Fig. 4.14. Fractured surface of a) SWNT-GO0, b) SWNT-GO10, and c) SWNT-GO20 film after failure and their POM images under two crossed linear polarizer.

Considering the fibril structure of SWNTs and platelet-like GO sheets, if the size-tuned GO sheets are preferentially oriented with their c axis parallel to the SWNT fibrils, the hybrid composite mimics the natural bone microstructure with fibril collagens and platelet hydroxyapatite nanocrystals. We simplified the microstructure of the hybrid composite films according to the used GO sheet size as shown in Figure 4.15. Large-scale GO sheets (Fig. 4.15a) induced isolated GO aggregation islands in the composite due to a strong intersheet π - π interaction. Such microstructures caused far less chemical cross-linking reactions with SWNTs. However, the small-scale GO sheets (Fig. 4.15b) can be homogeneously incorporated into SWNTs in a nearly mono-layered state, as confirmed by XRD and TEM results, with high-density cross-linking reactions that mimic the bone microstructure. As the load is applied, such bone-like microstructures can resist fractures by retarding the crack propagation due to its efficient stress transfer and acquiring a much higher specific strength and toughness. Additionally, a susceptible movement toward mechanical stimulus of this proposed system might enhance the mechanical properties.

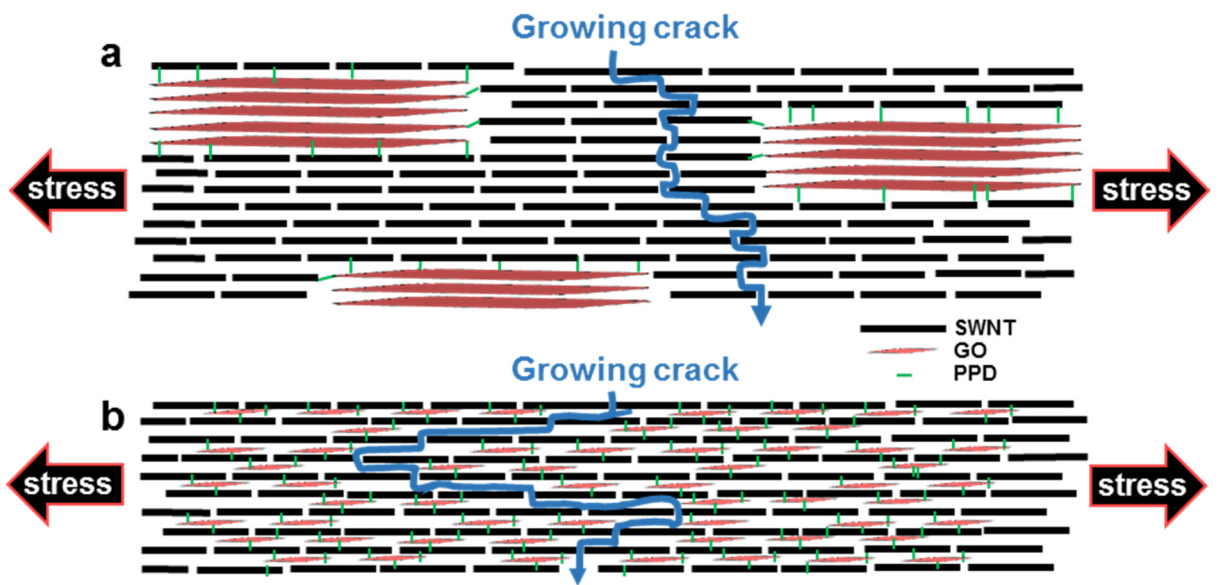


Fig. 4.15. Schematic diagram showing different architecture and fracture behavior of cross-linked a) SWNT-large GO and b) SWNT-small GO films.

4.3 Experimental

Preparation of SWNT-GO film.

SWNTs (1~2 nm in outer diameter, 10~15 μm in length, Purity > 95 wt.%, Timesnano, Chengdu Organic Chemicals Co. Ltd., China) were oxidized by a mixture of sulfuric acid and nitric acid (v/v = 3:1) at 60 °C for 24 h. GOs were prepared by a modified Hummers' method⁵¹ from large-flake graphite (Sigma Aldrich). The GO sheet size was controlled by varying the tip sonication time. Typically, 30 mg of SWNT were dispersed in 39 ml of DMF then mixed with 1 ml of size-controlled GO (10 mg/mL in concentration) and PPD under 6 h of moderate bath sonication. 1-ethyl-3-(3-dimethylaminopropyl) carbodiimide (EDC) and N-hydroxysuccinimide (NHS) (Sigma Aldrich) were added to activate the carboxyl groups of SWNT and GO and also facilitate the formation of amide bonds. The suspension was stirred for 24h before filtration and drying under vacuum at room temperature for one day.

Characterization

The size distribution of size-controlled GO samples was studied based on DLS using an ELSZ 1000ZS Size Analyzer, Otsuka. To ensure data reproducibility, DLS measurements were repeated 1000 times for each GO sample. The UV-vis spectra of SWNT-GO suspensions were acquired using a spectrometer (UV-vis-NIR Cary 5000 spectrometer, Varian). The XPS study of the SWNT-GO films was carried out to confirm the amide bond formation using a spectrometer (AXIS-His, KRATOS). The XRD profiles were obtained to study the interlayer distances and microstructure of solidified GO and SWNT-GO films using a D8 Advance (Bruker) diffractometer equipped with a

CuK α -radiation source ($\lambda = 1.54184 \text{ \AA}$). Tensile tests were performed using a universal testing machine (Instron-5543, Instron). The gage length and loading rate were 10 mm and 1 mm/min. Prior to the tensile test, the films were cut into the sizes (length: 32 mm, width: 6mm) shown in Figure 1a. The electrical properties were measured using a Keithley 2634B unit. The SEM (JSM6700F instrument, JEOL) was used to obtain the cross sectional morphology, fractured end of the SWNT-GO films, and the length distribution of individualized SWNTs on a Si wafer. The length distribution of individualized SWNTs was analyzed using Image-Pro Plus software. The AFM images and line scan results of each SWNT-GO film were obtained using the Surface Imaging Systems NANOSTationII instrument. The *in-situ* Raman spectroscopy was applied to the strained SWNT-GO films to measure the load-bearing capability using a Raman plus confocal laser Raman microscope (Nanophoton) with a 532 nm Nd-YAG laser source integrated with a tensile stage (TST350, Linkam). The TEM images were obtained using a microscope equipped with EDX (Tecnai F20, Philips). The optical images of the fractured ends were obtained using an Olympus BX-51 microscope in the reflection mode between two crossed linear polarizers.

4.4 Conclusion

We successfully developed a novel load-bearing hybrid architecture with SWNTs and size-tuned GO sheets reflecting the natural bone structure. The thinner and smaller GO sheets facilitate a homogeneous incorporation of GO sheets into SWNT buckypaper. In comparison with previous CNT and GO composite materials, the resultant films exhibited higher tensile strength, toughness, and exceptional electrical conductivity without any reduction. *In-situ* Raman spectroscopy with POM results revealed that the tailored GO sheets played a significant role as an efficient stress transfer medium. Taking into account the versatility of the proposed hybrid structure, alternative synthetic condition, and strengthening mechanism, we believe that the present approaches will open a reliable platform toward unique self-assembled architectures that mimic the nature and consecutive design of a carbon nanomaterial hybrid that has distinct functional features.

4.5 References

1. De Volder, M. F.; Tawfick, S. H.; Baughman, R. H.; Hart, A. J. Carbon nanotubes: present and future commercial applications. *Science* **2013**, *339*, 535-539.
2. Yu, M. F.; Files, B. S.; Arepalli, S.; Ruoff, R. S. Tensile loading of ropes of single wall carbon nanotubes and their mechanical properties. *Phys. Rev. Lett.* **2000**, *84*, 5552-5555.
3. Oh, J. Y.; Yang, S. J.; Park, J. Y.; Kim, T.; Lee, K.; Kim, Y. S.; Han, H. N.; Park, C. R. Easy preparation of self-assembled high-density buckypaper with enhanced mechanical properties. *Nano Lett.* **2015**, *15*, 190-197.
4. Boncel, S.; Sundaram, R. M.; Windle, A. H.; Koziol, K. K. K. Enhancement of the Mechanical Properties of Directly Spun CNT Fibers by Chemical Treatment. *ACS Nano* **2011**, *5*, 9339-9344.
5. Peng, B.; Locascio, M.; Zapol, P.; Li, S.; Mielke, S. L.; Schatz, G. C.; Espinosa, H. D. Measurements of near-ultimate strength for multiwalled carbon nanotubes and irradiation-induced crosslinking improvements. *Nat. Nanotechnol.* **2008**, *3*, 626-631.
6. Koziol, K.; Vilatela, J.; Moisala, A.; Motta, M.; Cunniff, P.; Sennett, M.; Windle, A. High-Performance Carbon Nanotube Fiber. *Science* **2007**, *318*, 1892-1895.
7. Motta, M.; Li; Kinloch, I.; Windle, A. Mechanical Properties of Continuously Spun Fibers of Carbon Nanotubes. *Nano Lett.* **2005**, *5*, 1529-1533.
8. Jung, Y.; Kim, T.; Park, C. R. Effect of polymer infiltration on structure and properties of carbon nanotube yarns. *Carbon* **2015**, *88*, 60-69.
9. Zhang, M.; Atkinson, K. R.; Baughman, R. H. Multifunctional Carbon Nanotube Yarns by Downsizing an Ancient Technology. *Science* **2004**, *306*, 1358-1361.
10. Zhang, M.; Fang, S.; Zakhidov, A. A.; Lee, S. B.; Aliev, A. E.; Williams, C. D.; Atkinson, K. R.; Baughman, R. H. Strong, Transparent, Multifunctional, Carbon

Nanotube Sheets. *Science* **2005**, *309*, 1215-1219.

11. Zhang, X.; Jiang, K.; Feng, C.; Liu, P.; Zhang, L.; Kong, J.; Zhang, T.; Li, Q.; Fan, S. Spinning and Processing Continuous Yarns from 4-Inch Wafer Scale Super-Aligned Carbon Nanotube Arrays. *Adv. Mater.* **2006**, *18*, 1505-1510.

12. Yan, Z.; Peng, Z.; Casillas, G.; Lin, J.; Xiang, C.; Zhou, H.; Yang, Y.; Ruan, G.; Raji, A. R.; Samuel, E. L., *et al.* Rebar graphene. *ACS Nano* **2014**, *8*, 5061-5068.

13. Stankovich, S.; Dikin, D. A.; Dommett, G. H.; Kohlhaas, K. M.; Zimney, E. J.; Stach, E. A.; Piner, R. D.; Nguyen, S. T.; Ruoff, R. S. Graphene-based composite materials. *Nature* **2006**, *442*, 282-286.

14. Dikin, D. A.; Stankovich, S.; Zimney, E. J.; Piner, R. D.; Dommett, G. H.; Evmenenko, G.; Nguyen, S. T.; Ruoff, R. S. Preparation and characterization of graphene oxide paper. *Nature* **2007**, *448*, 457-460.

15. Li, D.; Kaner, R. B. Materials science. Graphene-based materials. *Science* **2008**, *320*, 1170-1171.

16. Zhu, J.; Zhang, H.; Kotov, N. A. Thermodynamic and structural insights into nanocomposites engineering by comparing two materials assembly techniques for graphene. *ACS Nano* **2013**, *7*, 4818-4829.

17. Maiti, U. N.; Lee, W. J.; Lee, J. M.; Oh, Y.; Kim, J. Y.; Kim, J. E.; Shim, J.; Han, T. H.; Kim, S. O. 25th Anniversary Article: Chemically Modified/Doped Carbon Nanotubes & Graphene for Optimized Nanostructures & Nanodevices. *Adv. Mater.* **2013**, *26*, 40-67.

18. Park, S.; Lee, K. S.; Bozoklu, G.; Cai, W.; Nguyen, S. T.; Ruoff, R. S. Graphene oxide papers modified by divalent ions-enhancing mechanical properties via chemical cross-linking. *ACS Nano* **2008**, *2*, 572-578.

19. An, Z.; Compton, O. C.; Putz, K. W.; Brinson, L. C.; Nguyen, S. T. Bio-inspired

- borate cross-linking in ultra-stiff graphene oxide thin films. *Adv. Mater.* **2011**, *23*, 3842-3846.
20. Gao, Y.; Liu, L. Q.; Zu, S. Z.; Peng, K.; Zhou, D.; Han, B. H.; Zhang, Z. The effect of interlayer adhesion on the mechanical behaviors of macroscopic graphene oxide papers. *ACS Nano* **2011**, *5*, 2134-2141.
21. Li, Y. Q.; Yu, T.; Yang, T. Y.; Zheng, L. X.; Liao, K. Bio-inspired nacre-like composite films based on graphene with superior mechanical, electrical, and biocompatible properties. *Adv. Mater.* **2012**, *24*, 3426-3431.
22. Cui, W.; Li, M.; Liu, J.; Wang, B.; Zhang, C.; Jiang, L.; Cheng, Q. A strong integrated strength and toughness artificial nacre based on dopamine cross-linked graphene oxide. *ACS Nano* **2014**, *8*, 9511-9517.
23. Ryu, S.; Lee, Y.; Hwang, J.-W.; Hong, S.; Kim, C.; Park, T. G.; Lee, H.; Hong, S. H. High-Strength Carbon Nanotube Fibers Fabricated by Infiltration and Curing of Mussel-Inspired Catecholamine Polymer. *Adv. Mater.* **2011**, *23*, 1971-1975.
24. Shin, M. K.; Lee, B.; Kim, S. H.; Lee, J. A.; Spinks, G. M.; Gambhir, S.; Wallace, G. G.; Kozlov, M. E.; Baughman, R. H.; Kim, S. J. Synergistic toughening of composite fibres by self-alignment of reduced graphene oxide and carbon nanotubes. *Nat. Commun.* **2012**, *3*, 650.
25. Sun, H.; You, X.; Deng, J.; Chen, X.; Yang, Z.; Ren, J.; Peng, H. Novel graphene/carbon nanotube composite fibers for efficient wire-shaped miniature energy devices. *Adv. Mater.* **2014**, *26*, 2868-2873.
26. Koziol, K.; Vilatela, J.; Moisala, A.; Motta, M.; Cunniff, P.; Sennett, M.; Windle, A. High-performance carbon nanotube fiber. *Science* **2007**, *318*, 1892-1895.
27. Vilatela, J. J.; Elliott, J. A.; Windle, A. H. A model for the strength of yarn-like carbon nanotube fibers. *ACS Nano* **2011**, *5*, 1921-1927.

28. Wegst, U. G.; Bai, H.; Saiz, E.; Tomsia, A. P.; Ritchie, R. O. Bioinspired structural materials. *Nat. Mater.* **2015**, *14*, 23-36.
29. Nair, A. K.; Gautieri, A.; Chang, S. W.; Buehler, M. J. Molecular mechanics of mineralized collagen fibrils in bone. *Nat. Commun.* **2013**, *4*, 1724.
30. Ortiz, C.; Boyce, M. C. Materials science. Bioinspired structural materials. *Science* **2008**, *319*, 1053-1054.
31. Ritchie, R. O. The conflicts between strength and toughness. *Nat. Mater.* **2011**, *10*, 817-822.
32. Uddin, M. N.; Huang, Z. D.; Mai, Y. W.; Kim, J. K. Tensile and tearing fracture properties of graphene oxide papers intercalated with carbon nanotubes. *Carbon* **2014**, *77*, 481-491.
33. Chen, J.; Li, Y. R.; Huang, L.; Jia, N.; Li, C.; Shi, G. Q. Size Fractionation of Graphene Oxide Sheets via Filtration through Track-Etched Membranes. *Adv. Mater.* **2015**, *27*, 3654-3660.
34. Zheng, Q. B.; Ip, W. H.; Lin, X. Y.; Yousefi, N.; Yeung, K. K.; Li, Z. G.; Kim, J. K. Transparent Conductive Films Consisting of Ultra large Graphene Sheets Produced by Langmuir-Blodgett Assembly. *Acs Nano* **2011**, *5*, 6039-6051.
35. Kim, T.; Kang, J. H.; Yang, S. J.; Sung, S. J.; Kim, Y. S.; Park, C. R. Facile preparation of reduced graphene oxide-based gas barrier films for organic photovoltaic devices. *Energy & Environ. Sci.* **2014**, *7*, 3403-3411.
36. Liu, Z.; Robinson, J. T.; Sun, X. M.; Dai, H. J. PEGylated nanographene oxide for delivery of water-insoluble cancer drugs. *J. Am. Chem. Soc.* **2008**, *130*, 10876-10877.
37. Sun, X. M.; Liu, Z.; Welsher, K.; Robinson, J. T.; Goodwin, A.; Zaric, S.; Dai, H. J. Nano-Graphene Oxide for Cellular Imaging and Drug Delivery. *Nano Res.* **2008**, *1*, 203-212.

38. Kim, Y. S.; Kang, J. H.; Kim, T.; Jung, Y.; Lee, K.; Oh, J. Y.; Park, J.; Park, C. R. Easy Preparation of Readily Self-Assembled High-Performance Graphene Oxide Fibers. *Chem. Mater.* **2014**, *26*, 5549-5555.
39. Kim, J. E.; Han, T. H.; Lee, S. H.; Kim, J. Y.; Ahn, C. W.; Yun, J. M.; Kim, S. O. Graphene Oxide Liquid Crystals. *Angew. Chem., Int. Ed.* **2011**, *50*, 3043-3047.
40. Lee, K. E.; Kim, J. E.; Maiti, U. N.; Lim, J.; Hwang, J. O.; Shim, J.; Oh, J. J.; Yun, T.; Kim, S. O. Liquid Crystal Size Selection of Large-Size Graphene Oxide for Size-Dependent N-Doping and Oxygen Reduction Catalysis. *Acs Nano* **2014**, *8*, 9073-9080.
41. Yang, S. J.; Kang, J. H.; Jung, H.; Kim, T.; Park, C. R. Preparation of a freestanding, macroporous reduced graphene oxide film as an efficient and recyclable sorbent for oils and organic solvents. *J. Mater. Chem. A* **2013**, *1*, 9427-9432.
42. Park, S.; Dikin, D. A.; Nguyen, S. T.; Ruoff, R. S. Graphene Oxide Sheets Chemically Cross-Linked by Polyallylamine. *J. Phys. Chem. C* **2009**, *113*, 15801-15804.
43. Putz, K. W.; Compton, O. C.; Palmeri, M. J.; Nguyen, S. T.; Brinson, L. C. High-Nanofiller-Content Graphene Oxide-Polymer Nanocomposites via Vacuum-Assisted Self-Assembly. *Adv. Funct. Mater.* **2010**, *20*, 3322-3329.
44. Tian, Y.; Cao, Y.; Wang, Y.; Yang, W.; Feng, J. Realizing ultrahigh modulus and high strength of macroscopic graphene oxide papers through crosslinking of mussel-inspired polymers. *Adv. Mater.* **2013**, *25*, 2980-2983.
45. Yu, D. S.; Goh, K.; Wang, H.; Wei, L.; Jiang, W. C.; Zhang, Q.; Dai, L. M.; Chen, Y. Scalable synthesis of hierarchically structured carbon nanotube-graphene fibres for capacitive energy storage. *Nat. Nanotechnol.* **2014**, *9*, 555-562.
46. Cheng, Q. F.; Wu, M. X.; Li, M. Z.; Jiang, L.; Tang, Z. Y. Ultratough Artificial Nacre Based on Conjugated Cross-linked Graphene Oxide. *Angew. Chem., Int. Ed.* **2013**,

52, 3750-3755.

47. Wang, R. Z.; Suo, Z.; Evans, A. G.; Yao, N.; Aksay, I. A. Deformation mechanisms in nacre. *J. Mater. Res.* **2001**, *16*, 2485-2493.

48. Dresselhaus, M. S.; Dresselhaus, G.; Saito, R.; Jorio, A. Raman spectroscopy of carbon nanotubes. *Phys. Rep.* **2005**, *409*, 47-99.

49. Ma, W.; Liu, L.; Zhang, Z.; Yang, R.; Liu, G.; Zhang, T.; An, X.; Yi, X.; Ren, Y.; Niu, Z., *et al.* High-strength composite fibers: realizing true potential of carbon nanotubes in polymer matrix through continuous reticulate architecture and molecular level couplings. *Nano Lett.* **2009**, *9*, 2855-2861.

50. Kudin, K. N.; Ozbas, B.; Schniepp, H. C.; Prud'homme, R. K.; Aksay, I. A.; Car, R. Raman spectra of graphite oxide and functionalized graphene sheets. *Nano Lett.* **2008**, *8*, 36-41.

51. Marcano, D. C.; Kosynkin, D. V.; Berlin, J. M.; Sinitskii, A.; Sun, Z. Z.; Slesarev, A.; Alemany, L. B.; Lu, W.; Tour, J. M. Improved Synthesis of Graphene Oxide. *ACS Nano* **2010**, *4*, 4806-4814.

Chapter 5 Preparation and Mechanical/ Electrochemical Performance of TA@CNT Hybrid Film for Flexible Energy Storage System

5.1 Introduction

The increasing interest in flexible electronic devices such as collapsible display is connected to increasing studies on flexible energy storage materials.^{1,2} In many flexible supercapacitor electrodes, CNT based supercapacitor electrodes have attracted considerable attention due to their high electrical conductivities and porous structures for the fast transfer of ions and electrons.^{1,3,4} However, previously reported CNT based electrodes are not strong enough for the bending and stretching force.⁵ Therefore, CNT electrodes are easily degraded to external forces and lose their electrochemical performances. The alignment method in Chapter 3, which is introduced to increase the film strength, is not used as an approach since the close-packed nanostructure is not desirable for electron and ion diffusion. In this regard, a preparation method for CNT films that combines flexibility, strength, and high specific surface area is urgently required.

In this work, we report on the flexible, strong, and pseudocapacitive CNT film by

providing a functional metal-phenolic network between CNTs. In many chelation phenolic materials, tannic acid (TA), which is a natural polyphenol, is a very attractive material due to a facile coordination with metal ions. The pH dependent chelation and adhesion capability of TA on Au nanoparticles was recently demonstrated.⁶⁻⁹ We showed that TA could also wrap pristine SWNTs and disperse them in aqueous solutions. TA functionalized SWNT films displayed high flexibility, strength, modulus, and pseudocapacitive properties compared to pristine SWNT films.

5.2 Results and discussion

The preparation process of TA@SWNT film is illustrated in Figure 5.1. The dispersion issue has been challenging for pristine SWNTs in the wet process. Several approaches to disperse SWNTs in an aqueous solution were attempted, but acid treatments functionalized the oxygen functional groups on SWNTs and oxidized SWNTs showed decreased electrical conductivity. While the use of surfactant was nondestructive in the dispersion approach, the elimination of unnecessary surfactant after film preparation was difficult. Compared to previous functionalization methods, TA functionalization by metal-phenolic coordination complex demonstrates the nondestructive dispersion approach which is free of elimination issue. As shown in Figure 1, TA and Fe ions were dispersed after SWNT dispersion in water. When pH increased to 8, the well dispersed TA@SWNT suspension was obtained. The difference in degree of dispersion before and after Fe ion addition was shown in Figure 5.2. After the Fe ions coordinate with the TA catechol groups, the degree of SWNT dispersion is enhanced.

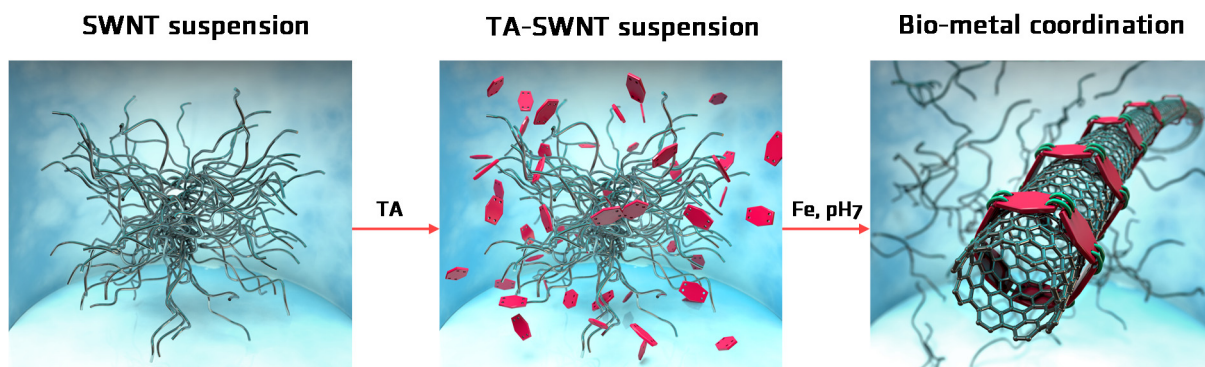


Fig. 5.1. Scheme of the TA@SWNT film preparation by Fe-catechol coordination.

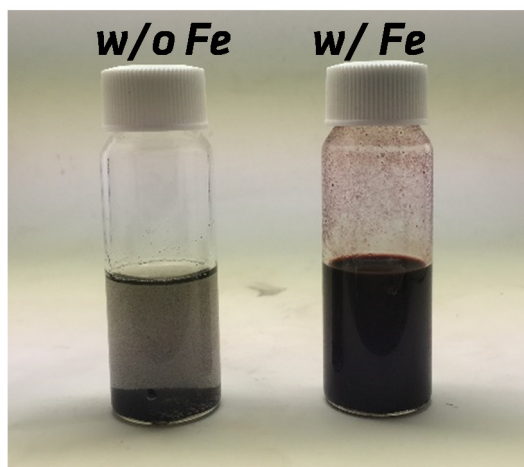


Fig. 5.2. Photograph of TA@SWNT suspensions before and after Fe ion addition.

TEM equipped with EDX was used to confirm the adsorption of TA on SWNTs by Fe-phenolic coordination. As shown in Figure 5.3a, pristine SWNTs exist in large bundles due to strong intermolecular van der Waals interactions. However, after TA adsorption on SWNTs, it was shown that individualized SWNT was obtained with surface coated morphology. The EDX line mapping analysis of the TA functionalized, individual SWNT shown in Figure 5.4 indicates that the oxygen and iron elements were uniformly coated to the surface of SWNT after Fe ion addition. The oxygen and iron content in the SWNTs existed homogeneously in the composite at around 14 and 0.4 wt.%, respectively. After the filtration of TA functionalized SWNT suspension, the TA@SWNT film was obtained. Consequently, the surface morphology and EDX area mapping analysis of TA@SWNT film was analyzed. As shown in Figure 5.5b, the TA@SWNTs had porous structures with random orientations like with pSWNT films (Figure 5.5a). The EDX area mapping analysis in Figure 5.5c demonstrated that oxygen and iron elements were homogeneously embedded to TA@SWNT films, which was in accord with the TEM/EDX line scan results. The uniform distributions indicated that the TA molecules were well coated to SWNTs by Fe-catechol coordination complex.

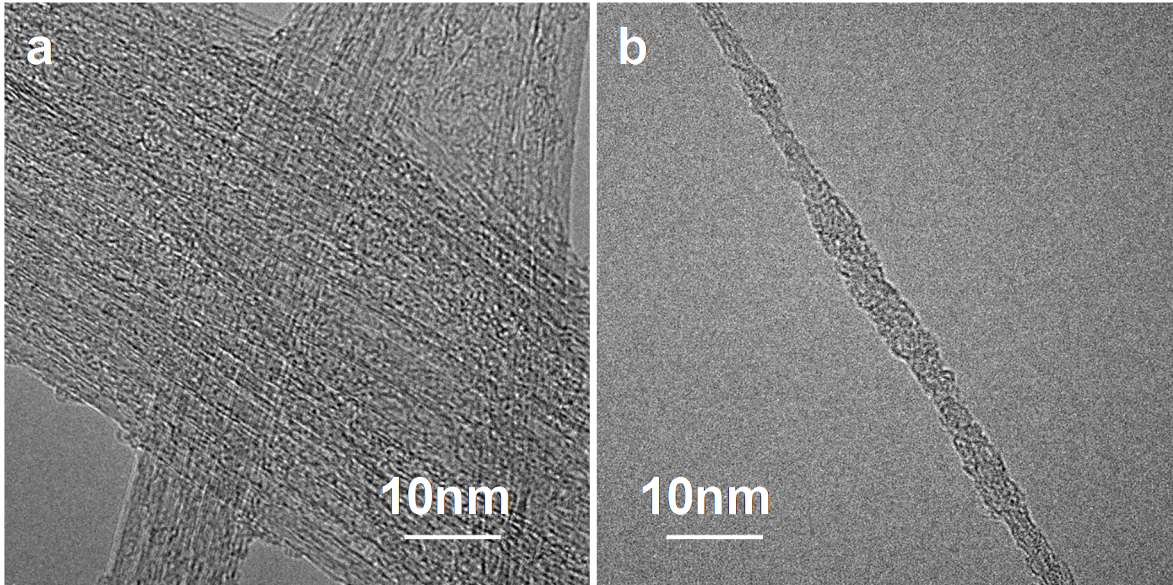


Fig. 5.3. TEM images of (a) pristine and (b) TA functionalized SWNT.

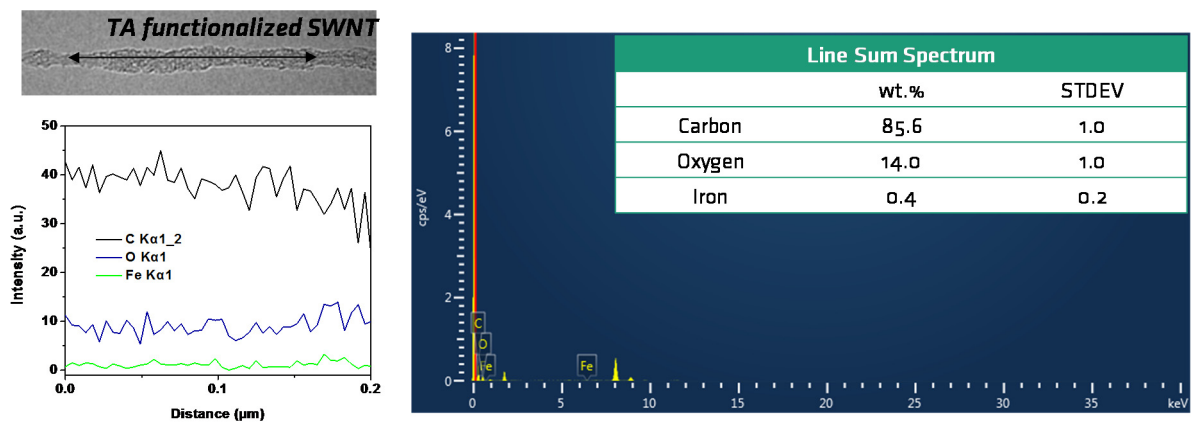


Fig. 5.4. TEM image and EDX line mapping analysis results of the TA functionalized, individual SWNT for carbon, oxygen, and iron elements with an inset table indicating content quantity.

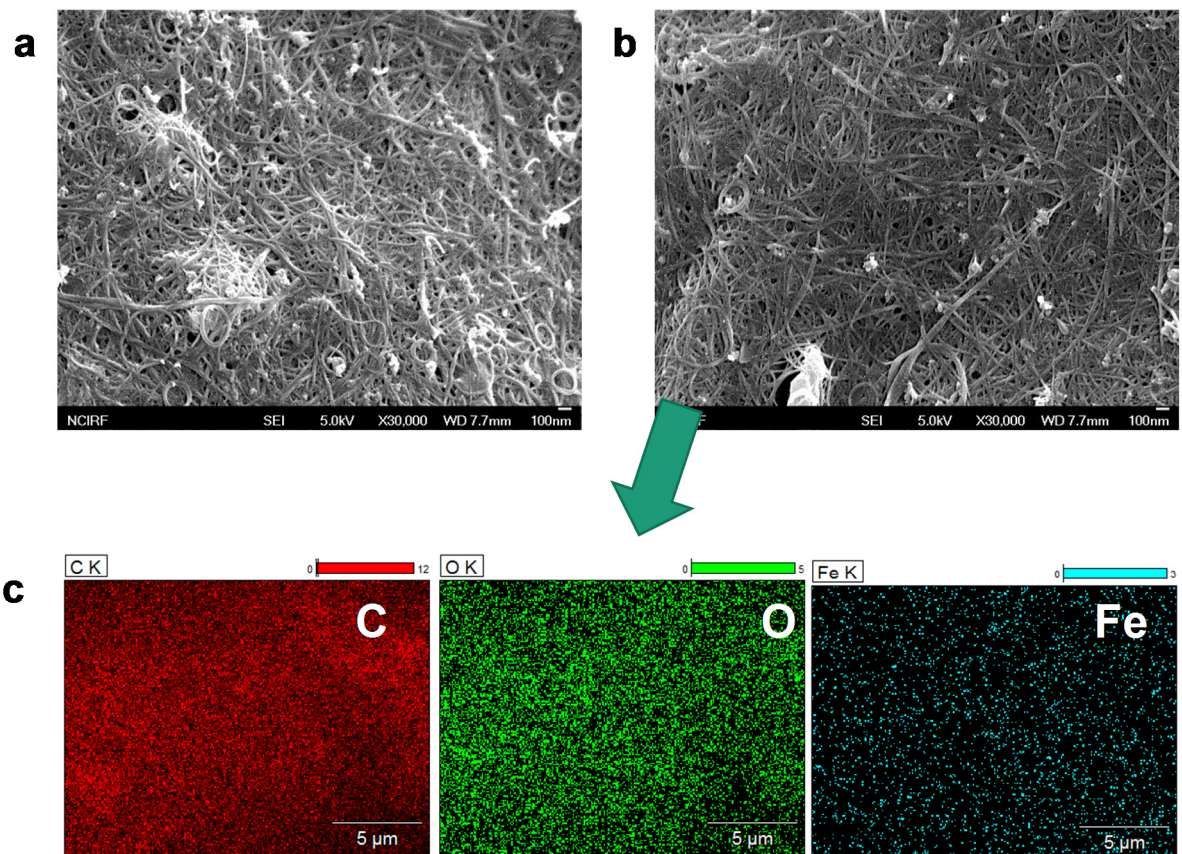


Fig. 5.5. SEM images of (a) pristine SWNT film and (b) TA@SWNT_10:1 film. EDX mapping analysis results of the TA@SWNT film for the carbon (red), oxygen (green), and iron (aquamarine) elements.

XPS was performed to obtain information about the surface chemical characteristics of the TA functionalized SWNT films with the varied TA mixing quantities. Figure 5.6. shows the XPS spectra with magnified views of the carbon (C1s) peaks and weight fractions of various C in the films. The peaks from the C1s spectra of pristine SWNT and TA@SWNT films were assigned to the C=C (284.5 eV), C-C (285 eV), C-O (286.1 eV), C=O (287.1 eV), O-C=O (288.2 eV), and pi-pi (290.3 eV) modes. As the quantity of wrapped TA increased, that of oxygen functional groups (C-O, C=O, and O-C=O) increased, as shown in Figure 5.6c.

TGA was carried out to calculate the weight ratio of the TA in the TA@SWNT film with varied TA quantities. Furthermore, the weight ratio was calculated just before the degradation of SWNTs near 425°C. As shown in Figure 5.7, the weight fraction of TA in the composite was increased to 36.2 and 55.7 % according to increased TA quantities. The electrical conductivity of the products was also shown in Figure 5.8. Due to the nonconductive TA molecules, the TA@SWNT films showed relatively decreased conductivity compared to pristine SWNT films.

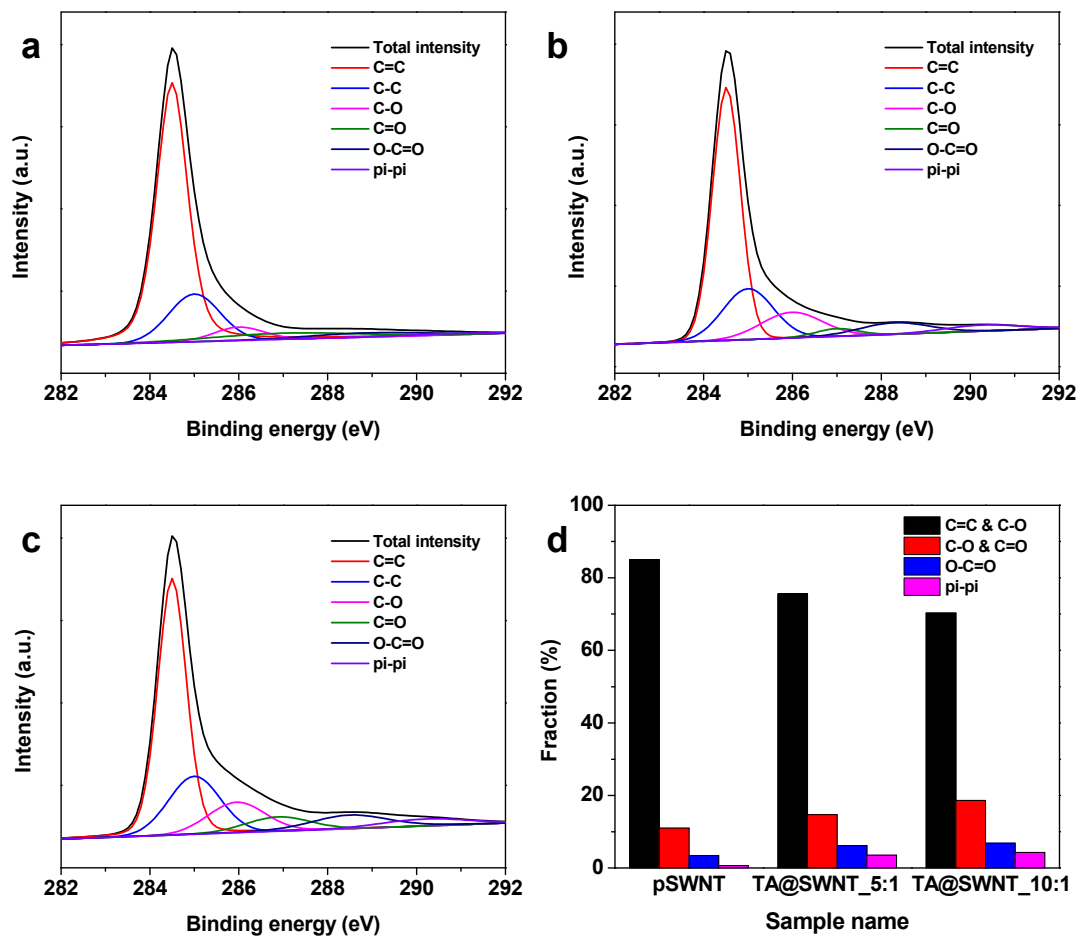


Fig. 5.6. C1s XPS spectra of (a) pristine SWNT film, (b) TA@SWNT_5:1 film, and (c) TA@SWNT_10:1 film. The quantitative analysis of various forms of carbon in the films calculated from C1s peak deconvolution.

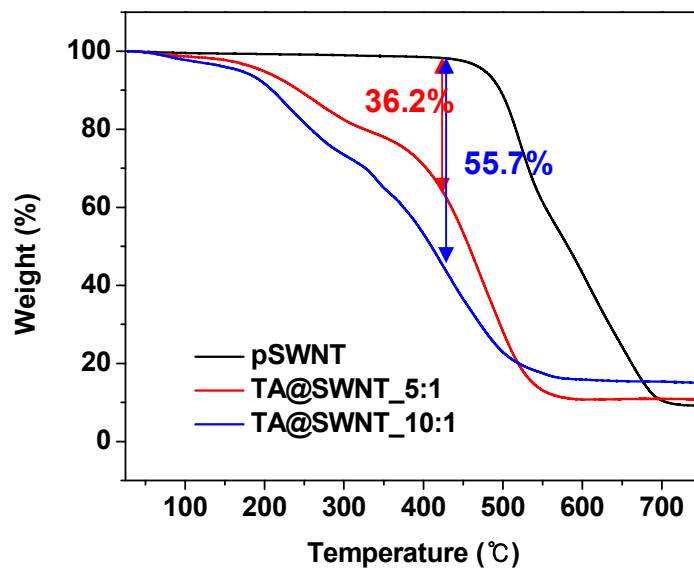


Fig. 5.7. TGA curves of pristine SWNT, TA@SWNT_5:1, and TA@SWNT_10:1 films.

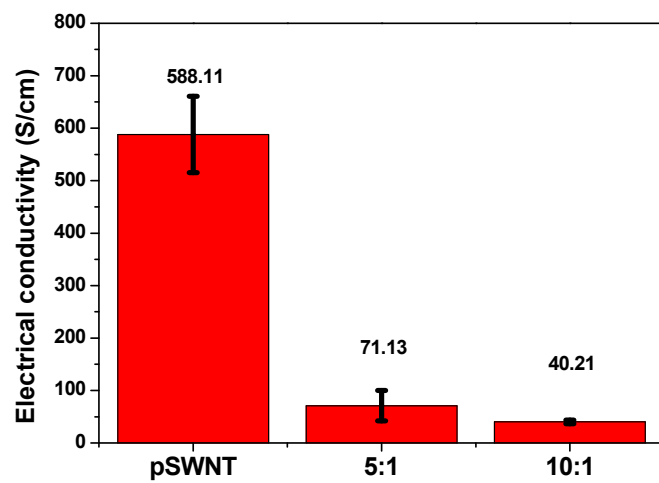


Fig. 5.8. The electrical conductivities of pristine SWNT, TA@SWNT_5:1, and TA@SWNT_10:1 films.

The effect of Fe-catechol coordination complex on the mechanical properties of TA@SWNT films was studied using a uniaxial tensile measurement. Figure 5.9 shows the representative stress-strain curves of TA@SWNT films. The average tensile strength of pristine SWNT film was 4.8 MPa, which was similar to previously reported films. TA@SWNT films prepared without Fe ions showed very low strength while the addition of Fe ions increased the tensile strength and modulus of TA@SWNT films. As the pH increased to 7, the tensile strength of TA@SWNT films increased due to the Fe-catechol transition of mono-complex to tris-complex and effective stress dissipation. As shown in Figure 5.5, although the TA@SWNT film had a porous structure with randomly oriented SWNTs, the strong metal-bio coordinated SWNTs show 4~20 times higher mechanical performance than films composed of pure SWNTs. Raman spectroscopy was performed to demonstrate the Fe³⁺-catechol coordination in SWNTs after the addition of Fe. As shown in Figure 5.10, a clear Raman band was shown at 650~750 cm⁻¹, originating specifically from the Fe³⁺ ion chelation by the catechol oxygen atoms.¹⁰ In low pH conditions, the peaks associated with the coordination were not observed. With the enhanced tensile strength, the mechanical stability and flexibility of the SWNT film upon bending was significantly enhanced, as shown in Figure 5.11, which was expected to be applied to flexible energy storage systems as freestanding electrodes.

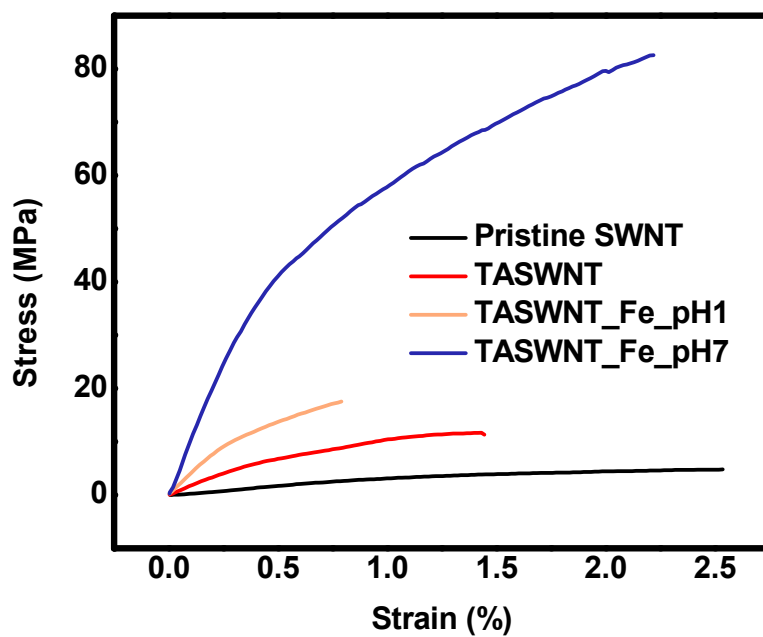


Fig. 5.9. Stress-strain curves of pristine SWNT (black), TA@SWNT prepared without Fe ions (red), TA@SWNT_Fe_pH1 (incarnadine), and TA@SWNT_Fe_pH7 (blue) films.

Table. 5.1. Tensile strength of pristine SWNT, TA@SWNT prepared without Fe ions, TA@SWNT_Fe_pH1, and TA@SWNT_Fe_pH7 films

Material	Fe	pH	Strength (MPa)	
			AVG	STD
SWNT	X	7~8	4.8	0.1
TA @ SWNT	X	7~8	12.0	1.2
TA @ SWNT	0	1	17.5	5.0
TA @ SWNT	0	7~8	82.9	6.11

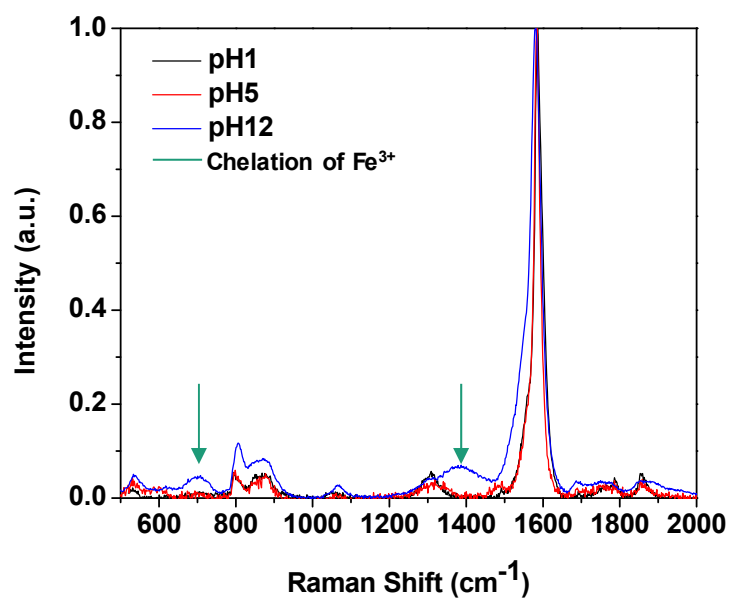


Fig. 5.10. Raman spectra of TA@SWNT prepared with varying pH.



Fig. 5.11. Photograph bended TA@SWNT film showing flexibility.

To analyze the electrochemical performance of the TA@SWNT films as a flexible, freestanding electrode material for flexible supercapacitors, cyclic voltammetry and galvanostatic charge/discharge performance tests at various rates were conducted using three electrode systems. As shown in Figure 5.12, the typical redox peaks around 0.4 V (vs SCE) correspond to the faradaic reaction of quinone groups in TA. The small peaks of pristine SWNT films near 0.4 V were known as oxygen containing carbon impurities.¹¹ The different current density of the films at a scan rate of 10 mV/s in the CV curves indicated increased charge storage capacitance of TA@SWNT films. Figure 5.13 illustrates the galvanostatic charge-discharge curves of the films. At an applied current density of 1A/g, the discharge curves of TA@SWNT_10:1 film obviously deviated from the typical linear shape of EDLC based supercapacitors. However, pristine SWNT and TA@SWNT_5:1 had almost linear shaped curves. For TA@SWNT_10:1 film, it was found that the specific capacitance between -0.2 and 0.5 V was much larger than that between 0.5 and 1 V, which with CV curves suggested that pseudocapacitance becomes dominating at low potential regions. As shown in Figure 5.14, the volumetric capacitance of TA@SWNT_10:1 films was superior compared to other films. The volumetric capacitance of TA@SWNT_10:1 film was 1.8 times higher than pristine SWNT film at an applied current density of 1A/g due to the additional pseudocapacitance properties of TA.

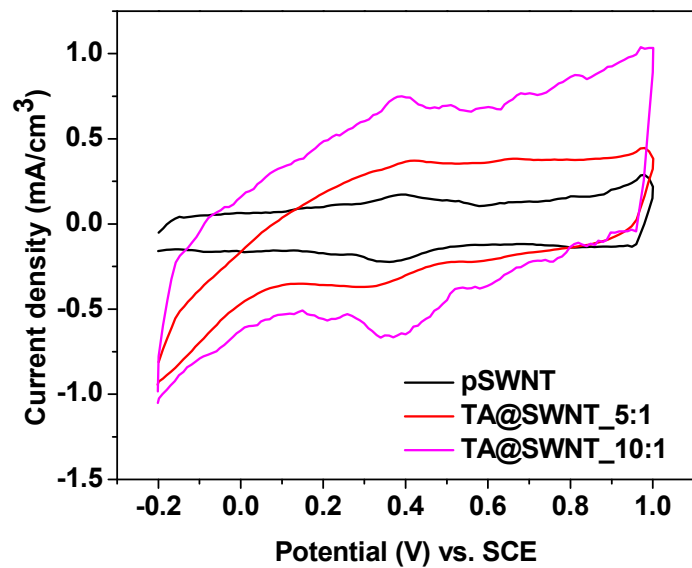


Fig. 5.12. Cyclic voltammetry curves of pristine SWNT, TA@SWNT_5:1, and TA@SWNT_10:1 films at a sweep rate of 10 mV/s in 1M H₂SO₄ solution.

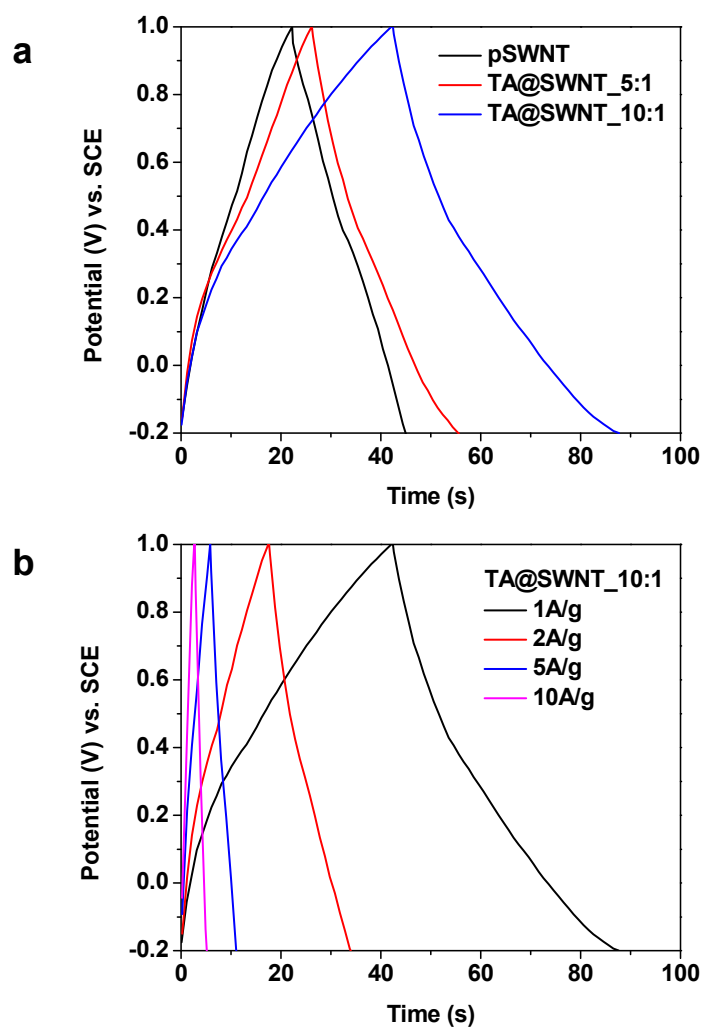


Fig. 5.13. Galvanostatic charge-discharge plot for (a) pristine SWNT, TA@SWNT_5:1, and TA@SWNT_10:1 films with a current of 1A/g (b) TA@SWNT_10:1 films with various currents in 1M H₂SO₄ solution.

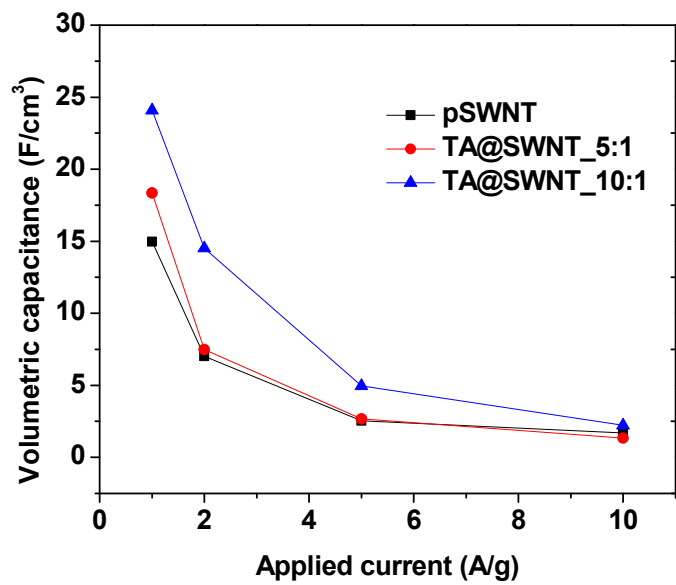


Fig. 5.14. Overall capacitance of the films as a function of discharge current density.

Due to the nonconductive TA in the composite, the electrical conductivity was not high and deteriorated the kinetics during the charge-discharge process. To increase the electrical conductivity of TA@SWNT films, the films were heated to 200 and 400°C at 2.5°C/min in nitrogen atmosphere. The phenolic groups on carbon decomposed at over 600°C in nitrogen atmosphere while the carboxylic acid groups carbonized near 200°C.^{12,13} The electrical conductivity of TA@SWNT film increased with the heating temperature, as shown in Figure 5.15. After the carbonization process, the change in quantity of surface functional groups on the film was analyzed as shown in Figure 5.16. Due to the high decomposition temperature of phenol and quinone groups, the peak intensities of C-O and C=O showed similar values, which the phenolic groups for metal coordination and pseudocapacitance preserved.

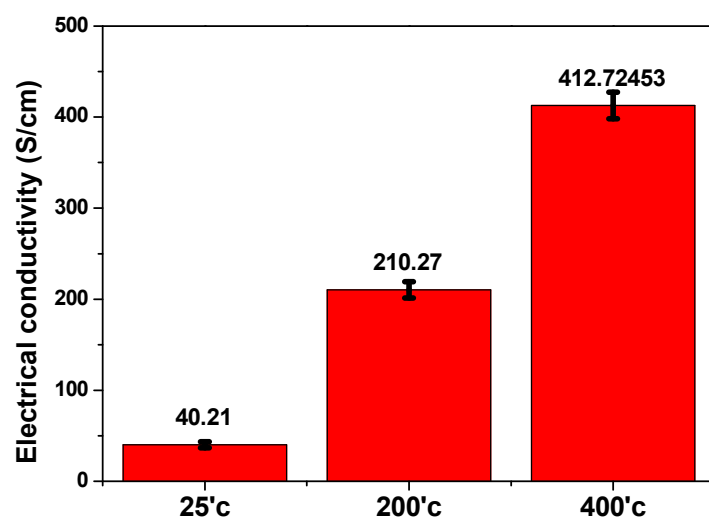


Fig. 5.15. The electrical conductivities of the heated TA@SWNT_10:1 films.

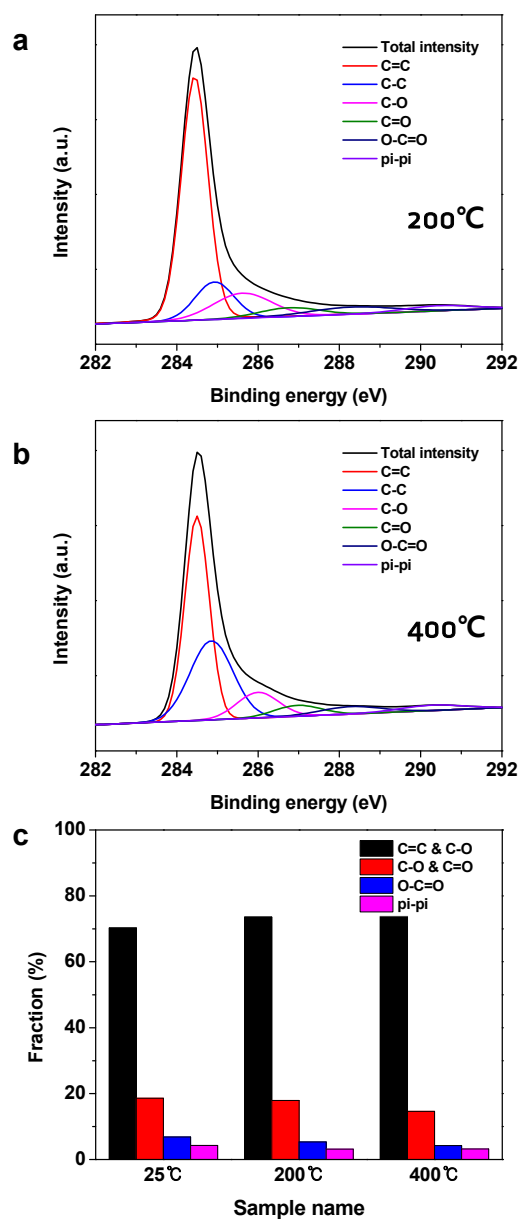


Fig. 5.16. C1s XPS spectra of TA@SWNT_{10:1} film after carbonization (a) at 200 and (b) 400°C. The quantitative analysis of various carbon forms in the films are calculated from the C1s peak deconvolution.

The galvanostatic charge-discharge curves of TA@SWNT films after carbonization were obtained at a current density of 1A/g. As shown in Figure 5.17a, the differences in the discharge curve shape was observed to determine that the heated sample had much higher capacitance. The slope of the 400°C sample changed greatly around 0.4 V due to the faradaic reaction after heat treatment. The volumetric capacitance of the TA@SWNT (400°C) sample showed 52.0 F/cm³, which was superior to other films. When we applied a lower current density than 1A/g, much higher values were obtained. These differences in volumetric capacitance with the carbonization temperature were due to differences in charge transfer. The Nyquist impedance spectra of the TA@SWNT films with varied carbonization temperature were illustrated in Figure 5.18. The AC impedance data for the samples were compared over the frequency range 100 kHz-10mHz under open circuit voltage after preliminary equilibration. The impedance analysis results clearly demonstrated that the charge transfer resistance (R_{ct}) of the films reduced with the increased heating temperature due to the faster charge transport.

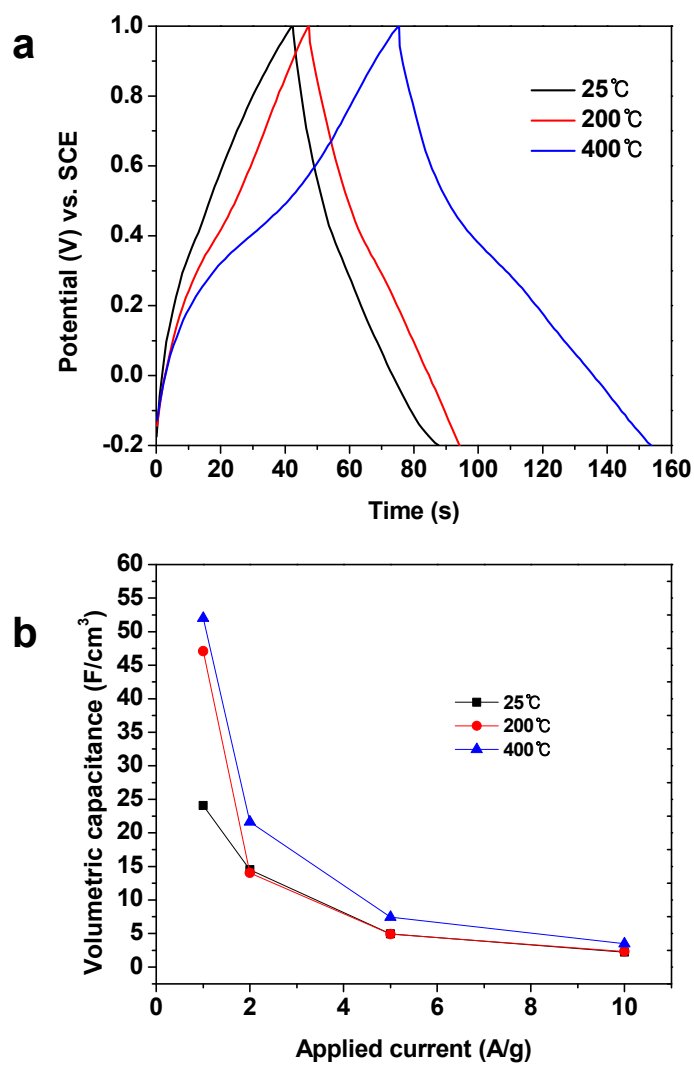


Fig. 5.17. (a) Galvanostatic charge-discharge plot for TA@SWNT_10:1 films with varied carbonization temperatures. (b) Overall film capacitance as a function of discharge current density with 1M H₂SO₄ solution.

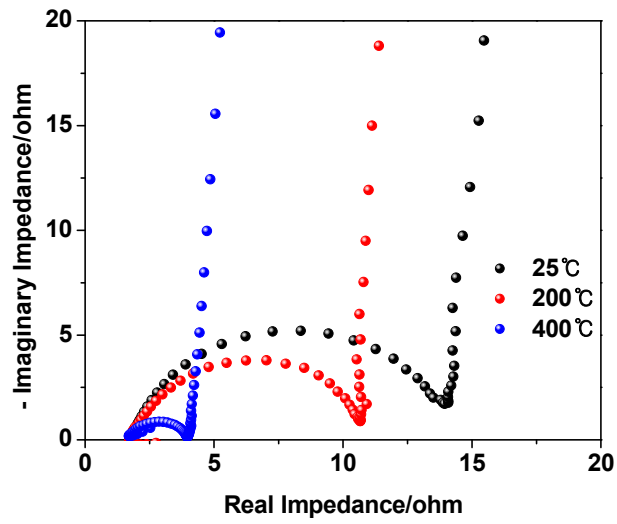


Fig. 5.18. Nyquist impedance spectra of the TA@SWNT films.

The Ragone plot in Figure 5.19, which summarized the electrochemical performances, was obtained from charge-discharge measurements of the TA@SWNT film at a variety of power densities based on the total mass. The energy density and power density with respect to TA@SWNT films were calculated using $E=0.5CV^2/M$ and $P=0.25V^2/RM$, where C was the capacitance from Figure 5.17, R was the internal resistance, and M was the total mass of the film. The flexible TA@SWNT film showed typical supercapacitor class in the Ragone plot and showed higher energy densities than carbon nanomaterials based on EDLC. The flexible, freestanding TA@SWNT film displayed extremely good cycling stability with only 3% variation in capacitance over 1000 cycles (Figure 5.20). During the electrochemical performance test at a 180° bent state as shown in the Figure 5.20 inset, the capacitance retention was excellent without any loss and enabled for application in flexible energy storage devices.

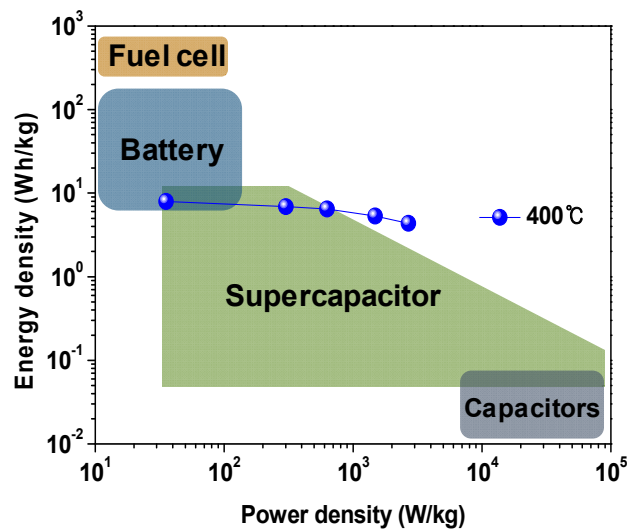


Fig. 5.19. Ragone plot for the TA@SWNT film at various charge-discharge rates in the working potential range of -0.2-1V. The data were calculated based on the total mass of the active electrode materials.

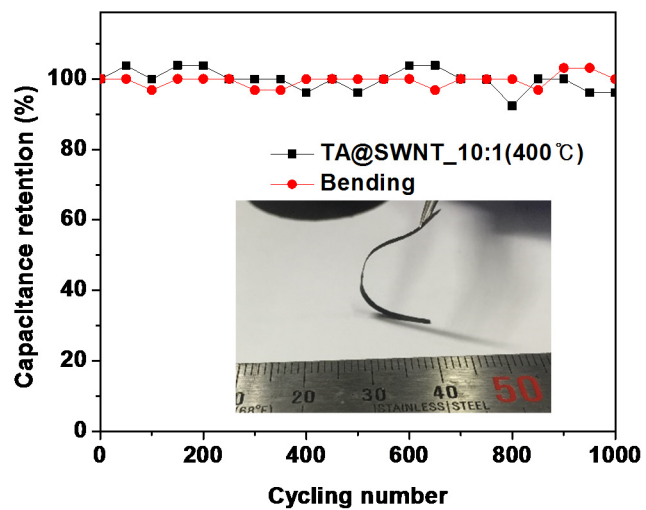


Fig. 5.20. Cycling stability of TA@SWNT film upon bending. The inset image shows the bent, flexible, and freestanding film.

5.3 Experimental

Materials.

The SWNTs (CVD, Purity > 95wt .%, 1–2 nm outer diameter, 10–15 μm length) used in this work were purchased from Timesnano, Chengdu Organic Chemicals Co. Ltd., China. The TA and iron (III) chloride hexahydrate ($\text{FeCl}_3 \cdot 6\text{H}_2\text{O}$) were purchased from Sigma-Aldrich. All materials were used as received.

Preparation of Fe^{3+} -Catechol coated SWNTs

The SWNTs, TA and $\text{FeCl}_3 \cdot 6\text{H}_2\text{O}$ were soaked in 20ml of DI water in a 40 ml vial. The final ratio of SWNT, TA and $\text{FeCl}_3 \cdot 6\text{H}_2\text{O}$ were as 1: 10: 2.5 and 1: 5: 2.5 by weight. The solution was vigorously mixed by magnetic stirring for 30 min at room temperature. The pH of this solution was subsequently adjusted to pH 8 by adding NaOH powder then the prepared solution was filtered and washed by DI water to prepare TA functionalized SWNT film. The resultant film was then dried in a vacuum oven for 48 h.

Characterization.

The transmission electron microscopy (TEM) images and energy-dispersive X-ray spectroscopy (EDX) line scan results were obtained by using a microscope equipped with EDX (JEM-2100F, JEOL). Scanning electron microscopy (SEM) (JSM6700F, JEOL) was used to analyze the surface morphology of the film. Furthermore, the TA weight fraction in SWNT composite was confirmed by thermogravimetry analysis (TGA)

in air atmosphere (10°C/min). The XPS study of the TA@SWNT films was carried out to confirm the formation of oxygen functional groups including phenol and carboxylic acid using a spectrometer (AXIS-His, KRATOS). The electrical conductivities of the prepared films were measured using a Keithley 2634B unit and tensile tests were carried out using a universal testing machine (Instron-5543, Instron). For tensile tests, the TA@SWNT films were cut to size (length: 32 mm, width: 2 mm). The gage length and loading rate were 10 mm and 1 mm/min, respectively. For Raman spectroscopic studies, a Raman plus confocal laser Raman microscope (Nanophoton) with a 785 nm laser source were used in combination with a 20x microscope objective. The electrochemical performances of the TA@SWNT films were investigated by cyclic voltammetry (CV) and galvanostatic charge-discharge test using three electrode systems with a battery cycler (WBCS3000, WonATech). The freestanding TA@SWNT films were used as working electrode without any supporting material. Pt wire and saturated calomel electrode (CHI150) were used as counter and reference electrodes, respectively. Finally, an electrochemical impedance spectroscopy (EIS) study was conducted with a potentiostate generator (ZIVE SP2).

5.4 Conclusion

In this study, we report the hybridization of natural polyphenol, TA, as a multifunctional material with SWNTs for flexible energy storage device applications. TA allows for the dispersion of SWNTs in water as well as strong interactions between SWNTs by creating metal-bio coordination complexes. Strong TA@SWNT films showed high pseudocapacitance properties after carbonization and the electrochemical performances were maintained upon deformation (bending). Such SWNT-based composite films with high mechanical strength, flexibility, lightweight, and conductivity can be utilized to boost the wearable electronic application.

References

1. Chen, T.; Dai, L. M., Flexible supercapacitors based on carbon nanomaterials. *J. Mater. Chem. A* **2014**, *2*, 10756-10775.
2. Yang, P. H.; Mai, W. J., Flexible solid-state electrochemical supercapacitors. *Nano Energy* **2014**, *8*, 274-290.
3. Wang, G. P.; Zhang, L.; Zhang, J. J., A review of electrode materials for electrochemical supercapacitors. *Chem. Soc. Rev.* **2012**, *41*, 797-828.
4. Simon, P.; Gogotsi, Y., Materials for electrochemical capacitors. *Nat. Mater.* **2008**, *7*, 845-854.
5. Katakabe, T.; Kaneko, T.; Watanabe, W.; Fukushima, T.; Aida, T., Electric double-layer capacitors using "bucky gels" consisting of an ionic liquid and carbon nanotubes. *J. Electrochem. Soc.* **2005**, *152*, A1913-A1916.
6. Ejima, H.; Richardson, J. J.; Liang, K.; Best, J. P.; van Koeveden, M. P.; Such, G. K.; Cui, J. W.; Caruso, F., One-Step Assembly of Coordination Complexes for Versatile Film and Particle Engineering. *Science* **2013**, *341*, 154-157.
7. Ejima, H.; Richardson, J. J.; Caruso, F., Multivalent Directed Assembly of Colloidal Particles. *Angew. Chem. Int. Edit.* **2013**, *52*, 3314-3316.
8. Guo, J. L.; Ping, Y.; Ejima, H.; Alt, K.; Meissner, M.; Richardson, J. J.; Yan, Y.; Peter, K.; von Elverfeldt, D.; Hagemeyer, C. E.; Caruso, F., Engineering Multifunctional Capsules through the Assembly of Metal-Phenolic Networks. *Angew. Chem. Int. Edit.* **2014**, *53*, 5546-5551.
9. Ye, Q.; Zhou, F.; Liu, W. M., Bioinspired catecholic chemistry for surface modification. *Chem. Soc. Rev.* **2011**, *40*, 4244-4258.
10. Holten-Andersen, N.; Harrington, M. J.; Birkedal, H.; Lee, B. P.; Messersmith, P. B.; Lee, K. Y. C.; Waite, J. H., pH-induced metal-ligand cross-links inspired by mussel

yield self-healing polymer networks with near-covalent elastic moduli. *P. Natl. Acad. Sci.* **2011**, *108*, 2651-2655.

11. Lin, Z. Y.; Liu, Y.; Yao, Y. G.; Hildreth, O. J.; Li, Z.; Moon, K.; Wong, C. P., Superior Capacitance of Functionalized Graphene. *J. Phys. Chem. C* **2011**, *115*, 7120-7125.

12. Figueiredo, J. L.; Pereira, M. F. R., The role of surface chemistry in catalysis with carbons. *Catal. Today* **2010**, *150*, 2-7.

13. Singhal, R.; Kalra, V., Using common salt to impart pseudocapacitive functionalities to carbon nanofibers. *J Mater. Chem. A* **2015**, *3*, 377-385.

Abstract in Korean

이 논문은 구조용, 다기능성 재료로 활용되기 위한 맞춤형 구조를 가진 새로운 탄소나노튜브 기반 복합체 필름의 제조 및 특성 분석에 대해 연구하고자 한다. 탄소나노튜브는 뛰어난 기계적, 전기적, 열적 특성을 가져 최근 수 십년간 물리/화학적 특성에 대한 근본적인 분석과 다양한 응용기술에 대한 연구를 활발하게 하였다. 그러나 기대와는 달리 다방향성으로 조립된 탄소나노튜브 버키페이퍼, 섬유, 실 등은 탄소나노튜브 한 가닥의 우수한 성질을 발현하지 못하고 있다. 게다가 기존에 보고된 약한 결합력을 가진 탄소나노튜브 필름들은 쉽게 외력에 의해 부서지고 그들의 특성을 잃어버려왔다. 나노구조를 제어하기 위한 기존의 방법들은 적용분야에 응용되기 위한 성능, 내구성, 대량생산성 등의 조건을 만족시키지 못했다. 그러므로 탄소나노튜브를 강한 상호작용력을 가지면서도, 정렬된 나노구조를 갖도록 제어하는 것은 고강도 다기능성 탄소나노튜브 필름을 제조하는데 가장 큰 이슈이다.

1장에서는 탄소나노튜브 기반 복합체 필름의 고강도, 다기능성 특성에 영향을 미치는 관련 물리/화학적 변수들을 소개하고자 한다. 최신의 탄소나노튜브 필름 재료들과, 해결되지 못한 이슈들이 토의될 것이다. 또한 본질적, 이론적 접근을 통한 본 연구의 목적을 소개한다.

2장에서는 고강도 탄소나노튜브 필름에 대해 기존에 보고된 실험결과들의

분석을 바탕으로 새로운 이론적 접근법을 연구하고자 한다. 탄소나노튜브 기반 필름의 기계적 특성과 구조적 파라미터들간의 상호관계를 연구함으로써 강도에 영향을 미치는 주요인자에 대한 이론을 제공하고자 한다. 탄소나노튜브 필름에 대한 이론적 모델링을 수행하여 특정 구조와 상호작용력에 의한 탄소나노튜브 필름의 기계적 물성을 예측하고, 궁극적으로 이상적인 구조와 특성을 제안하고자 한다.

3장과 4장에서는 응력 전달에 유리한 나노구조를 갖도록 설계하는 방법론으로, 자기조립 되어 뾰족한 나노구조를 갖는 한 방향으로 정렬된 탄소나노튜브와, 그래핀옥사이드@탄소나노튜브 필름의 제조 및 특성분석을 연구하고자 한다. 고밀도, 고배향성을 갖는 탄소나노튜브들은 간단한 필터링 방법을 통해 버키페이퍼의 형태로 제조되었다. 탄소나노튜브 분산액의 임계농도가 탄소나노튜브의 배향과 자기조립거동에 크게 영향을 미쳤다. 또한 필터링 과정 중에 단위면적당 쌓인 탄소나노튜브의 양이 증가할 때 수평으로 배향된 탄소나노튜브 도메인이 커짐을 확인하였다. 배향된 버키페이퍼는 기존에 보고된 버키페이퍼들에 비해 훨씬 높은 밀도, 강도, 탄성율과 경도를 보였다. 또한 자연의 뼈 구조를 모사하기 위한 그래핀 옥사이드/탄소나노튜브 하이브리드 복합체 필름이 제조되었다. 그래핀 옥사이드 크기 변환 전략은 효과적인 가교결합 반응으로 이어졌으며, 응력전달에 효과적인 구조를 성장시키는데 성공하였다. 제조된 하이브리드 복합체 필름은 우수한 강도, 인성, 전기전도도 등을 보였다. 또한 필름의 인장시험과 동시에 라만 분광법을 활용하여 크기가 변환된 그래핀

옥사이드의 응력전달 매개체로서의 역할을 새로이 입증하였다.

5장에서는 탄닌 산이 기능화되어 금속-생물 배위결합으로 상호작용력이 강한 고강도 기능성 탄소나노튜브 복합체 필름의 설계 및 분석을 연구하고자 한다. 제조된 복합체 필름은 탄소나노튜브의 기공구조를 유지하면서도 동시에 고강도와 유연성을 가짐이 확인되었다. 또한 이 재료는 크게 휘어진 조건에서도 높은 에너지 저장 성능이 유지되어 유연 에너지 저장 소자에 적용될 수 있음을 보였다.

주요어: 탄소나노튜브, 배향, 자기조립, 역학적 특성, 그래핀 옥사이드, 뼈 조직, 구조 재료, 유연 에너지 저장 시스템, 슈퍼커패시터

학번: 2011-30190

List of Publications

- 1. Jun Young Oh**, Seung Jae Yang, Jun Young Park, Taehoon Kim, Kunsil Lee, Yern Seung Kim, Heung Nam Han, Chong Rae Park, “Easy Preparation of Self-Assembled High-Density Buckypaper with Enhanced Mechanical Properties.”, *Nano Lett.* **2015**, *15* (1), 190.
- 2. Jun Young Oh**, Yeon Sik Choi, Seung Jae Yang, Jaeho Kim, Hong Soo Choi, Gi Dae Choi, Chang Hun Yun, Bong Keun Lee, Chong Rae Park, “Effect of microstructure and morphological properties of carbon nanotubes on the length reduction during melt processing.” *Compos. Sci. Tech.* **2015**, *88*, 60.
- 3.** Sae Jin Sung, Taehoon Kim, Seung Jae Yang, **Jun Young Oh**, Chong Rae Park, “New insights into the oxidation of single-walled carbon nanotubes for the fabrication of transparent conductive films.”, *Carbon* **2015**, *81*, 525.
- 4.** Seunghoon Nam, Seung Jae Yang, Sangheon Lee, Jaewon Kim, Joonhyeon Kang, **Jun Young Oh**, Chong Rae Park, Taeho Moon, Kyu Tae Lee, Byungwoo Park, “Wrapping Strategy for SnO₂ with Porosity-Tuned Graphene for High Rate Lithium-Anodic Performance.”, *Carbon* **2015**, *85*, 289.
- 5.** Yern Seung Kim, Jong Hun Kang, Taehoon Kim, Yeonsu Jung, Kunsil Lee, **Jun Young Oh**, Jisoo Park, Chong Rae Park, “Easy preparation of readily self-assembled high-performance graphene oxide fibers.”, *Chemistry of Materials* **2014**, *26* (19), 5549-

5555.

6. Hong Soo Choi, **Jun Young Oh**, Chong Rae Park, “One step synthesis of sulfur–carbon nanosheet hybrids via a solid solvothermal reaction for lithium sulfur batteries.”, *RSC Advances* **2014**, 4 (8), 3684-3690.

7. Jun Young Oh, Hong Soo Choi, Min Seok Kim, Yern Seung Kim, Chong Rae Park, “Effects of morphological characteristics of Pt nanoparticles supported on poly (acrylic acid)-wrapped multiwalled carbon nanotubes on electrochemical performance of direct methanol fuel cells.”, *J. Mater. Res.* **2012**, 27 (15), 2035-2045.

8. Jun Young Oh, Yern Seung Kim, Yeonsu Jung, Seung Jae Yang, Chong Rae Park, “Preparation and Exceptional Mechanical Properties of Bone Mimicking Size-Tuned Graphene Oxide@Carbon Nanotube Hybrid Paper.”, *ACS Nano* **2016**, *Accepted*.